

AD-A119 896

PENNSYLVANIA STATE UNIV UNIVERSITY PARK APPLIED RESE--ETC F/G 7/4  
PHOTO FIELD EMISSION AND FIELD EMISSION ENERGY DISTRIBUTIONS FR--ETC (U)  
JUL 82 M H HERMAN N00024-79-C-6043  
ARL/PSU/TM-82-177 NL

UNCLASSIFIED

1 of 2

00000

4 7  
1 6

5 2  
1 7

11  
11

AD A119896

6

PHOTO FIELD EMISSION AND FIELD EMISSION ENERGY  
DISTRIBUTIONS FROM SILICON

Michael H. Herman

Technical Memorandum  
File No. TM 82-177  
July 13, 1982  
Contract No. N00024-79-C-6043

Copy No. 8

The Pennsylvania State University  
Intercollege Research Programs and Facilities  
APPLIED RESEARCH LABORATORY  
Post Office Box 30  
State College, PA 16801

DTIC FILE COPY

APPROVED FOR PUBLIC RELEASE  
DISTRIBUTION UNLIMITED

DTIC  
ELECTE  
OCT 05 1982  
S D  
E

NAVY DEPARTMENT  
NAVAL SEA SYSTEMS COMMAND

82 10 05 021

UNCLASSIFIED

SECURITY CLASSIFICATION OF THIS PAGE (When Data Entered)

REPORT DOCUMENTATION PAGE		READ INSTRUCTIONS BEFORE COMPLETING FORM
1. REPORT NUMBER 82-177	2. GOVT ACCESSION NO. AD-A119896	3. RECIPIENT'S CATALOG NUMBER
4. TITLE (and Subtitle) PHOTO FIELD EMISSION AND FIELD EMISSION ENERGY DISTRIBUTIONS FROM SILICON		5. TYPE OF REPORT & PERIOD COVERED Ph.D. Thesis, November 1982
		6. PERFORMING ORG. REPORT NUMBER 82-177
7. AUTHOR(s) Michael H. Herman		8. CONTRACT OR GRANT NUMBER(s) N00024-79-C-6043
9. PERFORMING ORGANIZATION NAME AND ADDRESS The Pennsylvania State University Applied Research Laboratory, P.O. Box 30 State College, PA 16801		10. PROGRAM ELEMENT, PROJECT, TASK AREA & WORK UNIT NUMBERS
11. CONTROLLING OFFICE NAME AND ADDRESS Naval Sea Systems Command Department of the Navy Washington, DC 20362		12. REPORT DATE July 13, 1982
		13. NUMBER OF PAGES 151 pages
14. MONITORING AGENCY NAME & ADDRESS (if different from Controlling Office)		15. SECURITY CLASS. (of this report) Unclassified, Unlimited
		15a. DECLASSIFICATION/DOWNGRADING SCHEDULE
16. DISTRIBUTION STATEMENT (of this Report)  Approved for public release, distribution unlimited, per NSSC (Naval Sea Systems Command), September 14, 1982		
17. DISTRIBUTION STATEMENT (of the abstract entered in Block 20, if different from Report)		
18. SUPPLEMENTARY NOTES		
19. KEY WORDS (Continue on reverse side if necessary and identify by block number)  thesis, silicon, semiconductors, electron, field, emission		
20. ABSTRACT (Continue on reverse side if necessary and identify by block number)  Electron field emission from semiconductors is investigated both theoretically and experimentally. The theoretical predictions of the general Stratton theory are calculated specifically for silicon, in the [100], [110], and [111] directions. A method of simplifying the calculation of the energy distribution for arbitrary semiconductor bands is obtained, utilizing the effective mass approximation.  Experimental field emission energy distributions (FEEDs) are reported for		

DD FORM 1473  
1 JAN 73

EDITION OF 1 NOV 65 IS OBSOLETE

UNCLASSIFIED

SECURITY CLASSIFICATION OF THIS PAGE (When Data Entered)

UNCLASSIFIED

SECURITY CLASSIFICATION OF THIS PAGE(When Data Entered)

both n- and p- type samples of low resistivity. The experimental distributions are characterized by a high intensity single peak, of energy 0.4 eV or more below the Fermi level, with a subsidiary peak of lower intensity, rising from just below the Fermi level. The larger peak drops in energy with increasing field. Presented data demonstrates that this peak lowering is not attributable to sample resistance. Observation of the subsidiary peak is linked to either low sample temperature or low doping, implying that the carrier concentration affects its presence.

Experimental FEEDs are compared to those expected theoretically. It is concluded that they are not similar. Comparison with photoemission work indicates that the large peak is due to a band of surface acceptor states. The subsidiary peak is tentatively ascribed to conduction band electrons.

Finally, a phenomenological model of photo-field emission (PFE) is proposed. Based upon both FEED and PFE experiments, this model assumes that emission occurs primarily from surface states. A second component of the current is due to tunnelling of photogenerated electrons. In addition to photoconductivity, a self-regulating break-down mechanism is necessary for qualitative agreement with experimental data. One such mechanism, avalanche, is investigated for the dielectric emitter model. Qualitative agreement is obtained with the characteristic non-linear Fowler-Nordheim behavior observed experimentally.

Accession For	
NTIS GRA&I	<input checked="" type="checkbox"/>
DTIC TAB	<input type="checkbox"/>
Unannounced	<input type="checkbox"/>
Justification	
By _____	
Distribution/	
Availability Codes	
Dist	Avail and/or Special
A	



UNCLASSIFIED

SECURITY CLASSIFICATION OF THIS PAGE(When Data Entered)

## ABSTRACT

Electron field emission from semiconductors is investigated both theoretically and experimentally. The theoretical predictions of the general Stratton theory are calculated specifically for silicon, in the [100], [110], and [111] directions. A method of simplifying the calculation of the energy distribution for arbitrary semiconductor bands is obtained, utilizing the effective mass approximation.

> Experimental field emission energy distributions (FEEDs) are reported for both n- and p-type samples of low resistivity. The experimental distributions are characterized by a high intensity single peak, of energy 0.4 eV or more below the Fermi level, with a subsidiary peak of lower intensity, rising from just below the Fermi level. The larger peak drops in energy with increasing field. Presented data demonstrates that this peak lowering is not attributable to sample resistance. Observation of the subsidiary peak is linked to either low sample temperature or low doping, implying that the carrier concentration affects its presence.

Experimental FEEDs are compared to those expected theoretically. It is concluded that they are not similar. Comparison with photoemission work indicates that the large peak is due to a band of surface acceptor states. The subsidiary peak is tentatively ascribed to conduction band electrons.

Finally, a phenomenological model of photo-field emission (PFE) is proposed. Based upon both FEED and PFE experiments, this model assumes that emission occurs primarily from surface states. A second component of the current is due to tunnelling of photogenerated electrons. In addition to photoconductivity, a self-regulating breakdown mechanism is necessary for qualitative agreement with experimental data. One such mechanism, avalanche, is investigated for the dielectric emitter model. Qualitative agreement is obtained with the characteristic non-linear Fowler-Nordheim behavior observed experimentally.

## TABLE OF CONTENTS

	<u>Page</u>
ABSTRACT .....	iii
LIST OF TABLES.....	vii
LIST OF FIGURES.....	viii
ACKNOWLEDGEMENTS.....	xi
<u>Chapter</u>	
I. INTRODUCTION.....	1
II. THEORY.....	5
Field Emission from Metals.....	5
Field Emission from Semiconductors.....	11
General Formalism.....	11
General Band Considerations.....	14
Specific Conduction Band Calculations.....	19
[100] Direction.....	19
[110] Direction.....	19
[111] Direction.....	21
Valence Band Calculation.....	23
Predicted Energy Distributions from Si [100].....	24
III. APPARATUS AND EXPERIMENTAL PROCEDURES.....	29
Mechanical Components.....	29
Vacuum System.....	29
Energy Analyzer.....	31
Total Current-Voltage-Light Measurements.....	35
Electronics.....	38
Computer Interfacing.....	38
Hardware.....	38
Software.....	49
Sample Preparation.....	52
Cutting Blanks from Wafers.....	52
Photolithography.....	54
Abrasive Cutting.....	56
Electrolytic Etching.....	57
Pre-Vacuum Processing.....	58
In-Vacuum Processing.....	58
IV. EXPERIMENTAL RESULTS.....	61
Lightly Doped Silicon.....	61

## TABLE OF CONTENTS (Continued)

<u>Chapter</u>	<u>Page</u>
Energy Distributions.....	61
Current-Voltage-Light Characteristics.....	67
Heavily N-Doped Silicon.....	72
Energy Distributions.....	72
Field Desorbed Surface.....	74
Thermally Annealed Surface.....	74
Current-Voltage Characteristics.....	79
Heavily P-Doped Silicon.....	79
Discussion and Comparison of Results.....	83
Previous Work on Si.....	83
Previous Work on Other Semiconductors.....	84
Generalization and Discussion.....	87
V. PHOTO-FIELD EMISSION.....	93
Introduction.....	93
A Second Model.....	98
Account of Photoconductivity.....	99
Note on the Lifetime.....	100
Sample Resistance.....	101
Photogeneration of Carriers.....	101
Dielectric Model.....	107
Full Model with Breakdown.....	109
VI. CONCLUSION.....	116
SELECTED BIBLIOGRAPHY.....	120
APPENDIX A: BASIC PROGRAM FOR EXPERIMENTATION.....	125
APPENDIX B: MACHINE LANGUAGE PROGRAM FOR DATA ACQUISITION.....	132

LIST OF TABLES

<u>Table</u>	<u>Page</u>
1. Hardware Addresses and Data Assignments.....	39
2. Photo-Field Emission Surface Potential Measurements.....	66

## LIST OF FIGURES

<u>Figure</u>	<u>Page</u>
1. Energy Diagram for Metallic Emitter with Applied Field....	6
2. Definition of Emission Vectors and Angles.....	8
3. Theoretically Predicted Free Electron Total Energy Distributions.....	10
4. Band Structure of Silicon.....	13
5. General Mapping of Constant Energy Ellipsoids onto Emission Plane.....	15
6. Mapping of Constant Energy Ellipsoids onto (100) Plane....	20
7. Mapping of Constant Energy Ellipsoids onto (110) Plane....	22
8. Effect of Temperature on (100) Distribution from Degenerately N-Type Si.....	25
9. Effect of Temperature on (100) Distribution from Degenerately P-Type Si.....	26
10. Effect of Fermi Level Position on (100) Distribution from Si at 300K.....	27
11. Schematic Layout of Ultrahigh Vacuum System.....	30
12. Van Oostrum Energy Analyzer.....	32
13. Tungsten Calibration Distribution.....	34
14. Energy Diagram for Surface Potential Measurements.....	37
15. Block Diagram of Electronics.....	42
16. Buffer Board for Apple II Interfacing.....	43
17. Address Decoding Section.....	44
18. Plotter Controller.....	45
19. Retarder and Lens Controller.....	46

## LIST OF FIGURES (continued)

<u>Figure</u>	<u>Page</u>
20. Current-to-Voltage Converter (CVC) and Butterworth Filter.....	47
21. Analog-to-Digital Converter (ADC).....	48
22. Cleavage Characteristics and Sample Orientation from <100>-Oriented Si Wafers.....	53
23. Photolithographic Mask Designs.....	55
24. Various Surface Conditions Observed for Emitters.....	62
25. Illuminated vs. Dark FEEDs from High Resistivity P-Type Si.....	64
26. Photo-Field-Emission (PFE) Fowler-Nordheim Plot.....	65
27. Effect of Surface Condition on PFE Light/Dark Current Ratio .....	68
28. PFE Offset Voltage as a Function of Total Current.....	69
29. 78K PFE Current as a Function of Illumination Wavelength at Fixed Applied Voltage.....	70
30. 300K and 78K PFE Current as a Function of Illumination Wavelength at Fixed Applied Voltage.....	71
31. Onset, Peak Position, and Total Current as a Function of Applied Voltage for Heavily N-Doped Si.....	73
32. 300K FEED of Heavily N-Doped Si for Various Fields.....	75
33. 78K FEED of Heavily N-Doped Si for Various Fields.....	76
34. 300K FEED of Heavily N-Doped, Annealed Si.....	77
35. Fowler-Nordheim Plot for Heavily N-Doped Si.....	78
36. 300K FEEDs of Heavily P-Doped Si at Various Fields.....	80
37. Onset Position and Total Current as a Function of Applied Voltage for Heavily P-Doped Si.....	81
38. Fowler-Nordheim Plot for Heavily P-Doped Si.....	82

## LIST OF FIGURES (continued)

<u>Figure</u>	<u>Page</u>
39. Proposed Model of Surface State Density from Photoemission Experiments.....	89
40. Extension of Proposed Surface-State Model to Field Emission from N-Type Si.....	90
41. Log of Total Current as a Function of Inverse of Applied Voltage for Photoconductivity Correction to F-N Theory..	95
42. Fowler-Nordheim Plot of Photoconductivity Correction to F-N Theory.....	96
43. Fowler-Nordheim Plot of Revised Theory Without Breakdown..	105
44. Fowler-Nordheim Plot of Revised Theory with Hard Breakdown Mechanism.....	111
45. Fowler-Nordheim Plot of Revised Theory with Soft Breakdown Mechanism.....	112
46. Fowler-Nordheim Plot of Revised Theory with Hard Breakdown Mechanism Without Conduction Band Contribution.....	114
47. Fowler-Nordheim Plot of Revised Theory with Soft Breakdown Mechanism Without Conduction Band Contribution.....	115

## ACKNOWLEDGEMENTS

The author wishes to thank his research adviser, Professor Tien T. Tsong, for suggesting this study, and for his encouragement and patience during its course.

Further, the author thanks the members of the Field Emission Laboratory, in particular Mr. Brooks McLane for his electronics expertise and for help in computer interfacing. Thanks are also due to Mr. Thomas Kinkus, and Dr. Michael Martinka for their invaluable aid during the course of this research. The author is indebted to many professors at this university for productive discussions and for use of equipment essential to the completion of this project. In particular, the aid of Professor Monkowski and the services of the Solid State Device Laboratory of the Department of Electrical Engineering must be cited.

The author reserves special thanks for Mrs. Susan Herman for her support and her patience.

Lastly, the author acknowledges the financial support of the Applied Research Laboratory, the Pennsylvania Research Group, and the Department of Physics in supporting this research.

## CHAPTER I

### INTRODUCTION

Field emission (FE) from metals has been studied since the 1920's [26]. In 1928, theorists Fowler and Nordheim successfully predicted the FE current-voltage relationship [20]. Experimental verification of this theory and utilization in work function studies of adsorption followed [26]. Field emission energy distribution work (FEED) confirmed the "total energy" theory of Young, in 1959 [57,60]. These theoretical foundations were based upon the free electron theory of metals.

Serious experimental challenges, most notably the anomalous FEED from tungsten's (100) plane [53], were met with a more comprehensive theory. This general theory, due to Stratton [51,52], takes account of bulk band structure and its effects on the tunnelling probability of non-free electron bulk electronic states. This theory was considered to adequately explain the experimental results [23].

Due to the overall success of the Fowler-Nordheim (F-N) and Stratton theories for metals, work was extended to field emission from semiconductors. Strong deviations from F-N behavior were demonstrated in the early research on CdS [4]. These were attributed to photoconductivity, which could be adapted easily into the FN theory. Later,

however, Busch and Fischer showed that work function measurements from silicon showed an inverse relationship to that expected--n-type emitters demonstrated a higher barrier than those of p-type [11]. Further, the double peak with sharp energy gap, predicted by the Stratton theory, was not observed. Instead, two peaks of varying separation were generally seen [34,36]. Also, wide energy distributions were observed even from very heavily n-doped samples, contrasting greatly to those seen for metallic emitters [28,30]. In addition, it was demonstrated that photoconductivity could not account for the entirety of deviations in emission from high resistivity samples [56].

This thesis presents a study of field emission from semiconductors, silicon in particular. It is based on an attempt to synthesize the data of previous researchers with new experiments of FEED and photon stimulated field emission (or Photo Field Emission, PFE, in the literature). New analysis of this evidence is compared to both the theoretical predictions of the Stratton theory, and proposed surface state models. In particular, the implications of photoemission studies on Si are compared to the experimental results on FEED from semiconductors.

Using the results of this comparison, a new model of PFE is developed. Although the model utilizes crude approximations of the quantities involved, the predictions of the model show some qualitative agreement to the actual experimental data. This model is meant to be an incipient attempt to link together the experimental parameters of the PFE problem.

In undertaking the thesis, novel methods of sample prepara-

tion and data acquisition were developed. Photolithographic techniques were applied to precisely define sample dimensions. A suitable pre-cleaning treatment was found to reduce surface desorption problems usually associated with strong oxide layers on the Si. Also, an adapted van Oostrum type electron energy analyser was interfaced to an Apple II microcomputer. The computer control allows the user a number of features, such as rapid data acquisition, graphing, and numerical differentiation, which previously were performed manually. These techniques are described in detail.

The application of the Stratton theory to the silicon band structure is developed in an original way, using a simplified general approximation to the constant energy shadows. This calculation reduces the Stratton integrals to a form amenable to rapid numerical calculation. Direct application is made for emission from the silicon (100), (110), and (111) planes.

The thesis begins with a synopsis of Young's free electron FEED theory. This second chapter also contains a section comprising an original extension of Stratton's general formalism to cover the particular case of silicon. This provides a theoretical basis for comparison of the experimental FEEDs which will follow.

The third chapter introduces the experimental apparatus and electronics developed for FEED studies. Some brief discussion of the software, also originated for this work, follows. Further, improvements and innovations in the sample preparation are discussed. The equipment used in PFE studies is also described in this chapter.

Experimental results are explained in the fourth chapter. The

first section of this chapter summarizes results obtained from FEED, PFE, and F-N techniques, and gives surface micrographs for samples of various dopings and temperatures. Subsequent sections of this chapter compare these results to those of previous researchers. The last section discusses a generalization of these observations by comparison to the photoemission work of Wagner and Spicer.

The fifth chapter discusses PFE. Briefly deriving the photoconductivity additions to the F-N equation, it is demonstrated that these simple theoretical additions cannot completely satisfy the experimental data. Using the conclusions of the fourth chapter, a new model is developed, which yields more satisfying qualitative behavior.

The sixth chapter comprises a general conclusion to the thesis. Here, a brief summary is presented of the previous discussions. Following the conclusion are appendices containing the computer programs utilized in this study.

## CHAPTER II

## THEORY

Field Emission from Metals

The general theory of field emission from free electron metals was developed in 1928 by Fowler and Nordheim [20]. Their solution of the current-field relationship, the Fowler-Nordheim (F-N) equation, provided one of the first applications of wave mechanics to a tunnelling problem [26].

Young rederived the F-N equation along with the total energy distribution (TED) in a classic paper [57]. The formalism is repeated here, as silicon energy distributions will later be compared to the approximately free electron distributions from tungsten.

From Figure 1, we see that

$$V(z) = -W_a \quad z < 0 \quad (1)$$

$$= -ke^2/4z - eFz \quad z > 0 \quad (2)$$

where the first term of (2) is due to the image potential energy, and the second, the applied field. Here we distinguish between energy normal to the surface  $W$ , and total energy,  $E$  by

$$\begin{aligned} W &= E - p_x^2/2m - p_y^2/2m \\ &= p_z^2/2m + V(z) \end{aligned} \quad (3)$$

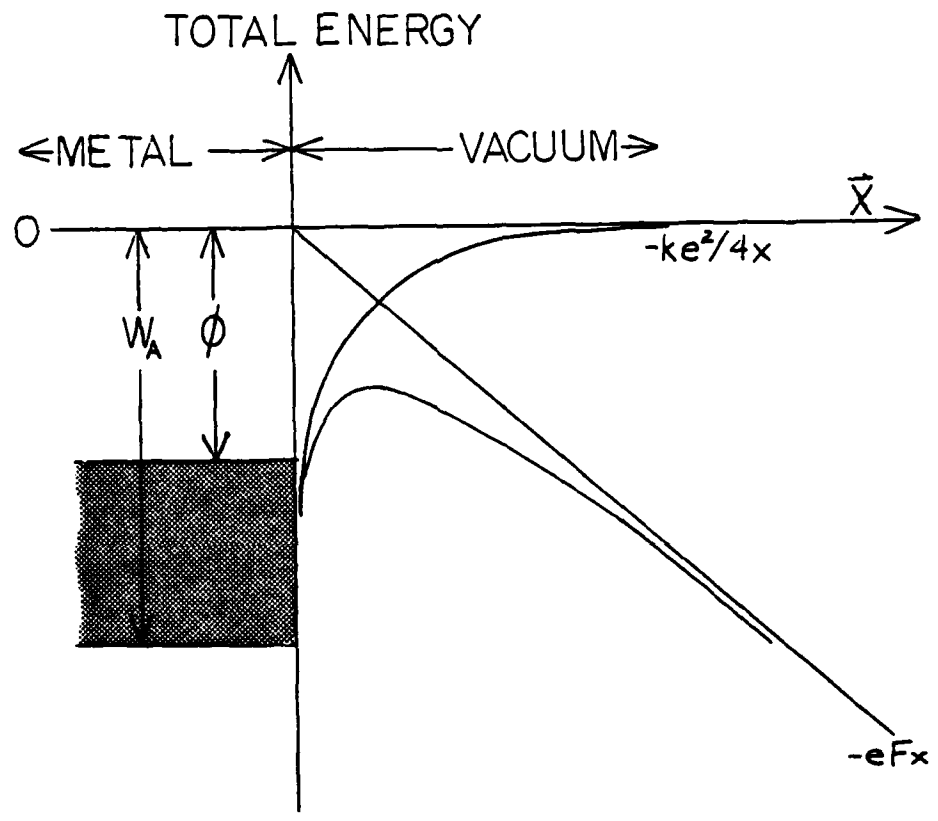


Figure 1. Energy Diagram for Metallic Emitter with Applied Field.

where  $p_i$  is the momentum in the  $i^{\text{th}}$  direction, and  $m$  the free electron mass.

By defining the following terms, Young placed the problem on manageable ground:

$N(W,E)dWdE$  = number of  $e^-$  incident at the surface in the interval  $(E, E+dE), (W, W+dW)$  per unit time per unit area.

$D(W)$  = probability of barrier penetration.

$P(W,E)dWdE = N(W,E)D(W)dWdE$  = number of  $e^-$  in interval which penetrate barrier.

$P(E)dE = (\int P(W,E)dW)dE$  = Total Energy Distribution.

$j = e \int P(E)dE$  = current/area = F-N equation.

Now we determine these quantities.

From Figure 2, we see that the component of  $\vec{v}$  in the  $\hat{z}$  direction is  $|\vec{v}|\cos\theta$ . The relative area encompassed goes as  $\sin\theta$ , so

$$N(\omega, E)d\omega dE = n(E)dE [ |\vec{v}|\cos\theta \sin\theta d\theta d\phi / 4\pi ] \quad (4)$$

where  $\omega$  is the solid angle,  $4\pi$  (steradians) the normalization,  $n(E)$  the density of electrons. Then

$$W = m(|\vec{v}|\cos\theta)^2 / 2 \quad (5)$$

and

$$-dW/m|\vec{v}| = |\vec{v}|\sin\theta\cos\theta d\theta = -dW/[2m(E-V)]^{1/2} \quad (6)$$

After substitution into (4) and integration over  $\phi$ ,

$$N(\omega, E)d\omega dE = -dWdEn(E)/2[2m(E-V)]^{1/2} \quad (7)$$

using

$$n(E)dE = \frac{4\pi(2m)^{3/2}(E-V)^{1/2}dE}{h^3(\exp[(E-u)/kT] + 1)} \quad (8)$$

gives

$$N(W, E)dWdE = \frac{-4\pi m dWdE}{h^3(\exp[(E-u)/kT] + 1)} \quad (9)$$

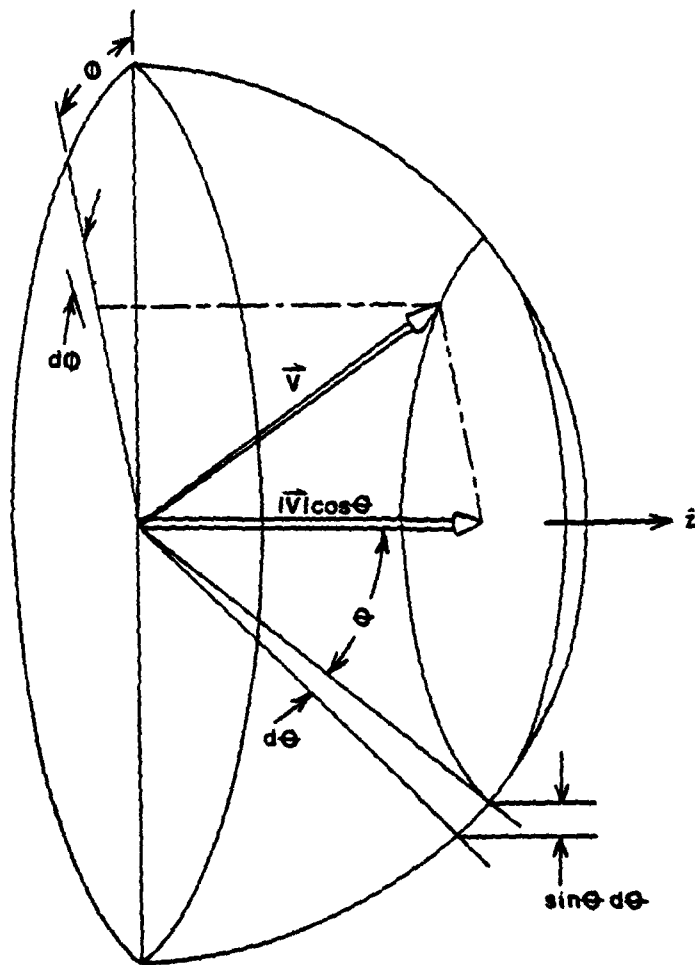


Figure 2. Definition of Emission Vectors and Angles.

Using a tunnelling probability  $D(W)$  of the form

$$D(W) = \exp[-c + (W - \mu)/d] \quad (10)$$

where  $c = 4(2m\phi^3)^{1/2}/3\hbar eF \times$

$$v((ke^3F)^{1/2}/\phi) \quad (11)$$

$d = \hbar eF/(2(2m\phi)^{1/2} \times$

$$t((ke^3F)^{1/2}/\phi) \quad (12)$$

Both  $t(y)$  and  $v(y)$  are tabulated functions of value near 1, and are discussed following equation (20) in the next section.

Upon integration:

$$P(E)dE = \int_{W=E}^{-W_A} N(W,E)D(W)dWdE \quad (13)$$

$$= \frac{4\pi md}{h^3} \times \frac{\exp(-c-\mu/d) \exp(E/d)dE}{1 + \exp([E-\mu]/kT)} \quad (14)$$

Then the total current density  $j$  is:

$$j = e \int_{-\infty}^{\infty} P(E)dE \quad (15)$$

$$= [e^3F^2/8\pi \hbar \phi t((a)^{1/2}/\phi)] \times \exp\left[\left[-4(2m)^{1/2} \phi^{3/2}/(3\hbar eF)\right] \times [v((a)^{1/2}/\phi)]\right] \times (\pi kT/d)/(\sin(\pi kT/d)) \quad (16)$$

where  $a = (ke^3F)$ .

Energy distributions, typical of the free electron model derived above, have been observed by many researchers. Various distributions appear in Figure 3, as predicted by Young's equations above. These show that the distribution widens with increasing temperature. Although this fact has been borne out by experimentation, there have

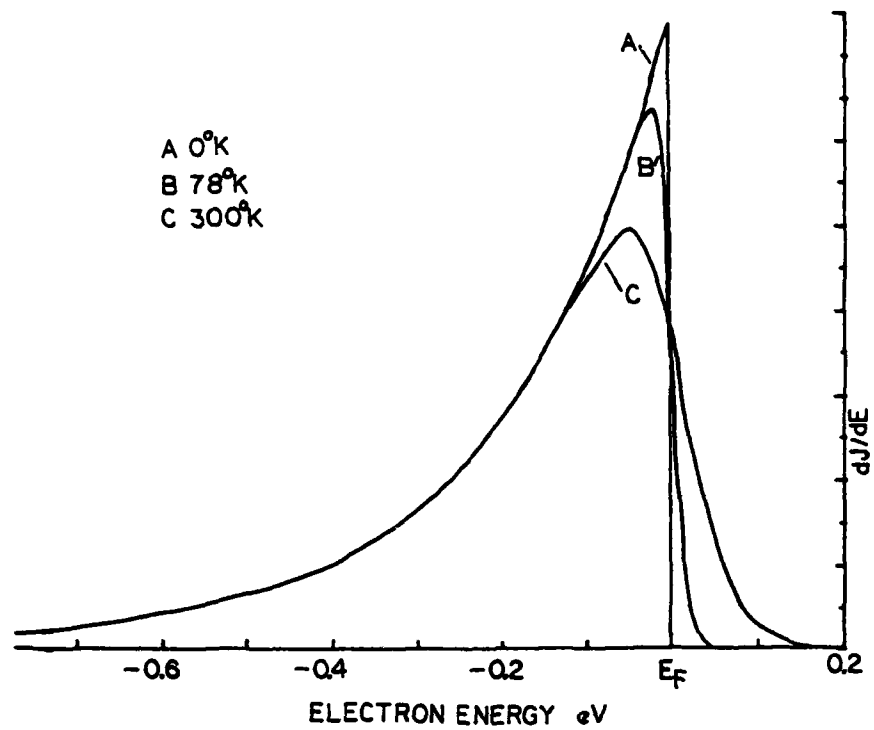


Figure 3. Theoretically Predicted Free Electron Total Energy Distributions.

also been found crystallographic directions of tungsten and molybdenum which do not exhibit the free electron distribution predicted [53]. To explain the phenomenon of "anomalous" energy distributions from metals, Stratton's theory of field emission from non-free electron solids was invoked [53]. This theory takes account of the actual band structure of the sample in describing the transverse energy, and will be described in the next section.

### Field Emission from Semiconductors

#### General Formalism

The free electron calculation of Young was generalized to non-free electron solids by Stratton [51,52]. This generalization has apparently been quite successful in explaining the anomalies obtained in TED's from tungsten in particular emission directions [23,53]. The Stratton formalism has since been the general theory for field emission from bulk states. Although measured TEDs from semiconductors do not agree with this theory [5,30], it provides a theoretical basis for the TED expected from bulk states. For this reason, the present section comprises an investigation of the predictions of this theory.

Stratton has pointed out that equation (13) may be written [52]:

$$P(E) = [2ef(E)/h^3] \iint D(W) dp_y dp_x \quad (17)$$

or equivalently:

$$P(E) = [2ef(E)/\pi(2\pi)^3] \iint D(W) dk_y dk_x \quad (18)$$

where the integration ranges over the shadow, on the emission plane, of the constant energy surface [23]. This form is useful for semiconductor calculations involving subbands or multivalley bands. The  $P(E)$  calculations for each component subband may be added algebraically [47]. To proceed further, one must know the explicit band structure of the sample in question. That of Si, for example, is shown in Figure 4.

To use the Stratton formalism, one must first derive expressions for the transverse energy  $E_t$ . This transverse energy is unavailable for tunnelling, and must be subtracted from the total energy  $E$  in the integral over  $D(W)$ . The procedure is straightforward in the  $\langle 100 \rangle$  directions, for the constant energy ellipsoids of the conduction band are either along or normal to these axes. For other directions, the procedure for finding  $E_t$  is non-trivial.

Further, the form of  $D(W)$  given in equation (10) is not general. The form used by Young was an approximation of the general WKB result, with image corrections, valid near  $E_F$ . The general result for metals is [23]:

$$D(W) = \exp[-(4/3eF)(2m/\hbar^2)^{1/2} \\ \times [\phi - (W - E_F)]^{3/2} \\ \times v[(ke_F^3)^{1/2} / (\phi - (W - E_F))] ] \quad (19)$$

or  $D(W) = \exp[-0.685 (\phi - (W - E_F))^{3/2}/F$



$$x \sqrt{3.79 F^{1/2} / (\phi - (W - E_F))} \quad (20)$$

with  $F$  in  $V/\text{\AA}$ ,  $\phi$ ,  $W$ ,  $E_F$ , in eV. In the above equations,  $v(y)$  and  $t(y)$  can be approximated by:

$$v(y) \cong A_0 + A_1 y + A_2 y^2 + A_3 y^3 \quad (0 < y < 1)$$

with  $A_0 = 1.0056$ ,  $A_1 = -0.1521$ ,  $A_2 = -1.0625$ ,  $A_3 = 0.2083$

and  $t(y) \cong 1 + 0.1y$

The correct form for semiconductors of dielectric constant  $K$  differs slightly, due to reduction of the image potential by the factor  $[(K-1)/(K+1)]^{1/2}$ , as discussed by R. Gomer [25].

#### General Band Considerations

Although the actual integrations must be performed to determine  $P(E)$  for any particular emission direction, the transverse energy at the conduction band edge may be expressed exactly. For arbitrary emission direction  $\vec{D} = h\hat{i} + k\hat{j} + l\hat{k}$ , there exist three sets of 2-fold degenerate lobes--one pair per axis. The centers of these lobes are at an energy of 3.7eV along each axis, from the origin [11]. Thus the transverse energy along the emission direction is  $3.7\text{eV}\sin^2\theta$ , with  $\theta$  the angle between  $\vec{D}$  and the axis. But  $\sin^2\theta = (k^2 + l^2)/(h^2 + k^2 + l^2)$  for the  $i$  axis, and the same for the other axes by cyclic permutation of the indices. Thus

$$E_{ti}(hkl) = 3.7\text{eV} (k^2 + l^2)/(h^2 + k^2 + l^2) \quad (21)$$

$$E_{tj}(hkl) = 3.7\text{eV} (h^2 + l^2)/(h^2 + k^2 + l^2) \quad (22)$$

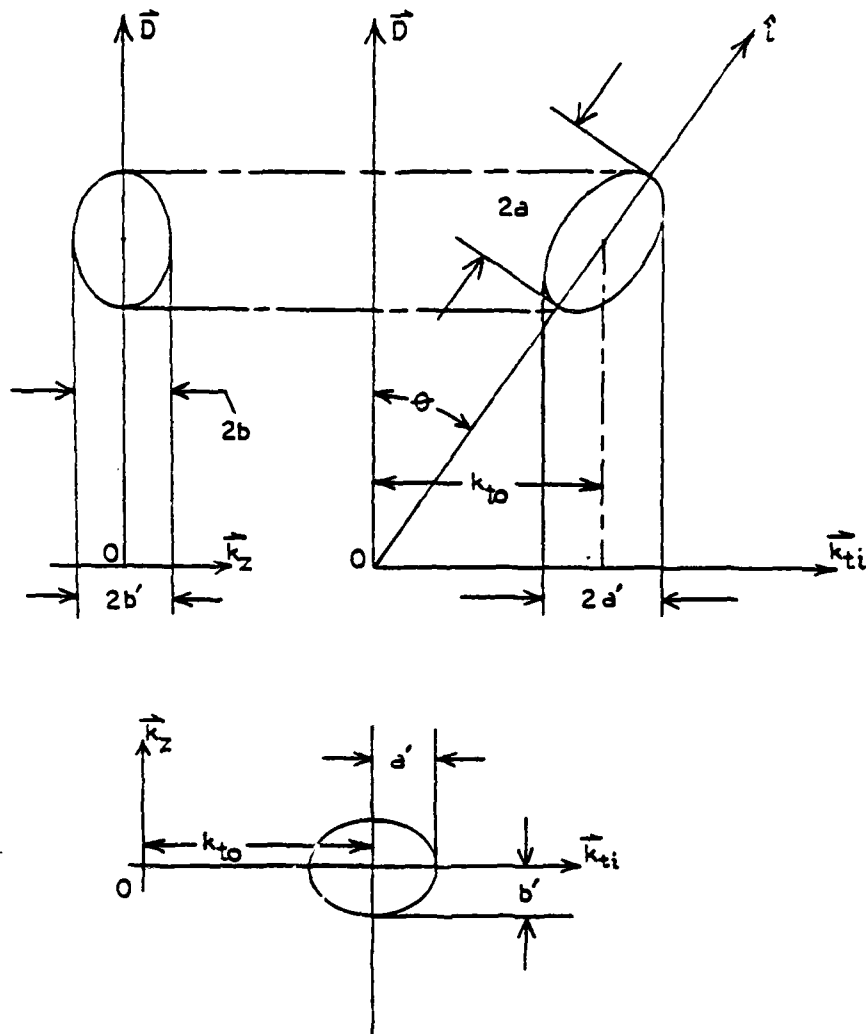


Figure 5. General Mapping of Constant Energy Ellipsoids onto Emission Plane. Here,  $a$  and  $a'$  denote the semimajor axes,  $b$  and  $b'$  denote the semiminor axes. Unprimed variables correspond to the constant energy ellipsoid, primed ones to the shadow on the emission plane.

$$E_{tk}(hkl) = 3.7\text{eV} (h^2 + k^2) / (h^2 + k^2 + l^2) \quad (23)$$

The general solution of  $P(E)$  for the silicon conduction band may be made with the following assumptions. First, because of the symmetry of the constant energy ellipsoids about their long axis, the angle between the long axis and the emission vector  $\vec{D}$  completely specifies the shape of the transverse energy shadow. The dimensions of this shadow, of course, must come from  $E$  and the effective masses.

Secondly, it is assumed that each 3-d constant energy ellipsoid is mapped into a 2-d ellipse on the surface plane. This assumption allows us to use the construction in Figure 5, whereby we must compute the maximum transverse distance in the 2-d  $k$ -space of the emission plane to determine  $a'$  for the 2-d ellipse. This  $a'$  in turn will give the "effective" effective mass for the 2-d ellipse on the long axis. The value for  $b'$  of the 2-d ellipse will always be given by the same value,  $b$ . This is intuitively true because the width of the shadow of the 3-d ellipsoid is constant, although the length of the shadow will depend upon the angle  $\theta$ .

We begin by describing the projection of the ellipsoid in the  $\vec{D}$ - $\hat{i}$  plane by

$$K(k_x, k_y) = k_x^2/a^2 + k_y^2/b^2 = 1 \quad (24)$$

with  $a^2 = 2m_l E / \hbar^2$ ;  $b^2 = \hbar^2 / \pi^2$

putting the equation of the ellipse into standard form. Here,  $m_l$  and  $m_t$  are the longitudinal and transverse effective masses, of value  $0.91m$  and  $0.19m$  respectively [8]. We wish to maximize the distance  $d(k_x, k_y)$  between a point  $k_x, k_y$  and the emission vector  $\vec{D} = \hat{h}i + \hat{k}j + \hat{l}k$ , given by

$$d(k_x, k_y) = k_x \sin\theta - k_y \cos\theta \quad (26)$$

Using the Euler-Lagrange multiplier method, we take

$$\delta d(k_x, k_y) = \lambda \delta K(k_x, k_y) \quad (27)$$

$$\Delta k_x \sin \theta - \Delta k_y \cos \theta = \lambda (2k_x \Delta k_x / a^2 + 2k_y \Delta k_y / b^2) \quad (28)$$

or

$$(2k_x \lambda / a^2 - \sin \theta) \Delta k_x + (2k_y \lambda / b^2 + \cos \theta) \Delta k_y = 0 \quad (29)$$

for any  $\Delta k_x$ ,  $\Delta k_y$ . Therefore, each expression in parentheses in (29) must be zero, so

$$k_x^* = a^2 \sin \theta / 2\lambda \quad ; \quad k_y^* = -b^2 \cos \theta / 2\lambda \quad (30)$$

Substituting (30) into (24) yields

$$k_x^{*2} / a^2 + k_y^{*2} / b^2 = 1$$

$$\text{so} \quad \lambda = \pm (a^2 \sin^2 \theta + b^2 \cos^2 \theta)^{1/2} / 2 \quad (31)$$

We choose the + sign, since maximal distance is obtained when  $k_x > 0$ ,  $k_y < 0$ . Substituting into (30) again, gives

$$\begin{aligned} k_x^* &= a^2 \sin \theta / (a^2 \sin^2 \theta + b^2 \cos^2 \theta)^{1/2} \\ k_y^* &= -b^2 \cos \theta / (a^2 \sin^2 \theta + b^2 \cos^2 \theta)^{1/2} \end{aligned} \quad (32)$$

Again substituting (32) into (26) yields

$$d(k_x^*, k_y^*) = (a^2 \sin^2 \theta + b^2 \cos^2 \theta)^{1/2} = a' \quad (33)$$

The new 2-d ellipse must be:

$$k_t'^2 / a'^2 + k_z'^2 / b'^2 = 1 \quad (34)$$

with

$$a'^2 = 2m^* E / \hbar^2 = a^2 \sin^2 \theta + b^2 \cos^2 \theta \quad (35)$$

$$b'^2 = 2m_t E / \hbar^2$$

Installing a and b from equation (24) yields for  $m^*$ :

$$m^*(\theta) = m_l \sin^2 \theta + m_t \cos^2 \theta \quad (36)$$

The general expression for conduction band transverse energy must take into account the shifted origin of the 2-d ellipse. As described in

equations (21) to (23) this implies that

$$\hbar^2 k_{to}^2 / (2m^*(\theta)) = 3.7\text{eV} \sin^2\theta$$

$$\text{with } k_{to} = [(3.7\text{eV})2m^*(\theta) \sin^2\theta / \hbar^2]^{1/2} \quad (37)$$

and a transverse energy  $E_t$  described by

$$E_t(\theta) = \hbar^2(k_t + k_{to})^2 / 2m^*(\theta) + \hbar^2 k_z^2 / (2m_t) \quad (38)$$

Finally, we may generalize the  $P(E)$  from the conduction band to:

$$P(E) = 2 \times [ 2ef(E)/\pi(2\pi)^3 ] \times$$

$$\sum_{i=1}^3 \left( \int_{-a}^a \left[ \int_{-b_i(k_z)}^{b_i(k_z)} D(E - E_{ti}) dk_{ti} \right] dk_z \right) \quad (39)$$

$$a = [2m_t E / \hbar^2]^{1/2} \quad (40)$$

$$\sin^2\theta_i = [h^2(1 - \delta_{i1}) + k^2(1 - \delta_{i2}) + l^2(1 - \delta_{i3})] \times 1/(h^2 + k^2 + l^2) \quad (41a)$$

$$\cos^2\theta_i = (\delta_{i1}h^2 + \delta_{i2}k^2 + \delta_{i3}l^2)/(h^2 + k^2 + l^2) \quad (41b)$$

$$\delta_{ij} = 1 \text{ if } i=j; 0 \text{ if } i \neq j$$

$$m_i^* = m_1 \sin^2\theta + m_t \cos^2\theta \quad (42)$$

$$k_{oi} = [2 (3.7\text{eV}) m_i^* \sin^2\theta / \hbar^2]^{1/2} \quad (43)$$

$$b_i = [(2m_i^*/\hbar^2) \times (E - \hbar^2 k_z^2 / 2m_t)]^{1/2} \quad (44)$$

$$E_{ti} = [\hbar^2(k_{ti} + k_{oi})^2 / (2m_i^*) + \hbar^2 k_z^2 / (2m_t)] \quad (45)$$

It should be noted here that the shadow of each constant energy ellipsoid is taken into account separately, even if the shadows overlap on the emission plane. Calculations for the three major crystallographic planes are described in particular in the following sections.

## Specific Conduction Band Calculations

[100] Direction

The general form given above, equations (39) to (45), can be broken into two parts for the [100] direction. These two cases arise because of the degeneracy in energy of the ellipsoids symmetrically centered on the  $\hat{j}$  and  $\hat{k}$  axes, as shown in Figure 6, and the ellipsoids doubly degenerate in momentum with centers on the  $\hat{i}$  axis. It can be shown that (39) simplifies to

$$P(E) = [2ef(E)/(\hbar (2\pi)^3)] \times$$

$$\begin{aligned} & (4 \int_{-a}^a \left( \int_b^b D(E - E_t) dk_t \right) dk_z + \\ & 2 \times (2\pi) \int_0^c D(E - \hbar^2 k_t^2 / (2m_t)) k_t dk_t ) \end{aligned} \quad (46)$$

with

$$a = c = [2m_t E / \hbar^2]^{1/2}$$

$$b = [2m_1 E / \hbar^2 - m_1 k_z^2 / m_t]^{1/2} \quad (47)$$

$$E_t = \hbar^2 (k_t + k_0)^2 / (2m_1) + \hbar^2 k_z^2 / 2m_t \quad (48a)$$

$$k_0 = [2 (3.7\text{eV}) m_1 / \hbar^2]^{1/2} \quad (48b)$$

[110] Direction

The [110] direction conduction band of silicon exhibits 2-fold momentum degeneracy of ellipses centered on the  $\hat{i}$  and  $\hat{j}$  axes. As shown in Figure 7, ellipsoids centered on the positive side of these

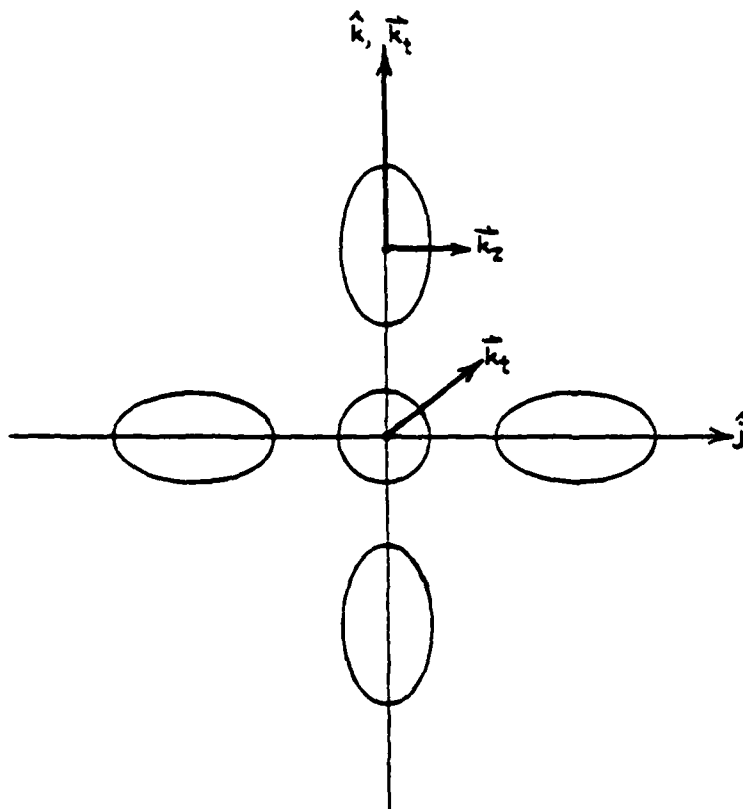


Figure 6. Mapping of Constant Energy Ellipsoids onto (100) Plane.

axes lie above those centered on the negative side. These overlapped ellipsoids still contribute to the transverse energy integrals over  $k_t$ ,  $k_z$ , though their shadows are degenerate with those of the ellipsoids above. For this reason, the form of  $P(E)$  for the conduction band is:

$$P(E) = [2ef(E)/\pi(2\pi)^3] \times$$

$$\begin{aligned} & (4 \int_{-a}^a \left[ \int_{-b_1}^{b_1} D(E - E_{t1}) dk_{t1} \right] dk_z + \\ & 2 \int_{-a}^a \left[ \int_{-b_2}^{b_2} D(E - E_{t2}) dk_{t2} \right] dk_z ) \end{aligned} \quad (49)$$

$$a = [2m_t E/\hbar^2]^{1/2}$$

$$b_i = ([2m_i^*/\hbar^2] \times [E - \hbar^2 k_i^2/2m_t])^{1/2} \quad (50)$$

$$m_1^* = (m_1 + m_t)/2 ; m_2^* = m_1 \quad (51)$$

$$k_{01} = [m_1^* 3.7\text{eV}/\hbar^2]^{1/2}$$

$$k_{02} = [2m_1 3.7\text{eV}/\hbar^2]^{1/2} \quad (52)$$

$$E_{ti} = [\hbar^2(k_{ti} + k_{0i})^2/2m_i^* + \hbar^2 k_z^2/2m_t] \quad (53)$$

### [111] Direction

The [111] direction is completely non-degenerate in  $k_t$ -space. That is, the shadows of each of the six ellipsoids do not overlap for reasonably low energies. However, the ellipsoids are degenerate in energy, and so the general formula, equation (39), reduces to:

$$P(E) = [2ef(E)/\pi(2\pi)^3] \times$$

$$6 \times \left( \int_{-a}^a \left( \int_{-b}^b D(E - E_t) dk_t \right) dk_z \right) \quad (54)$$

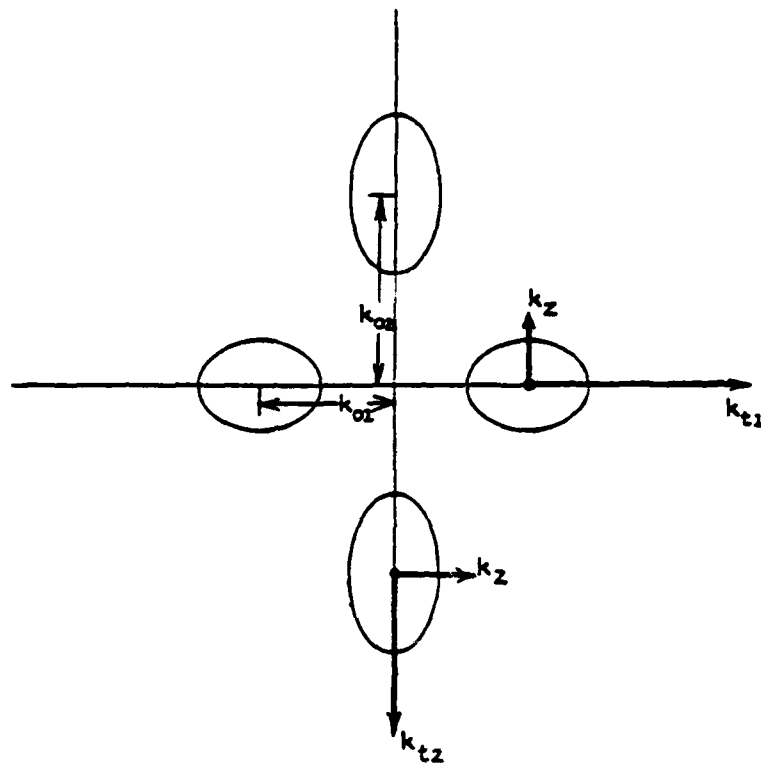


Figure 7. Mapping of Constant Energy Ellipsoids onto  $(110)$  Plane.

$$\begin{aligned} \text{with } a &= [2m_t E/\hbar^2]^{1/2} \\ b &= [(2m^*/\hbar^2)(E - \hbar^2 k_z^2/2m_t)]^{1/2} \end{aligned} \quad (55)$$

$$\begin{aligned} m^* &= (2m_1 + m_t)/3 \\ k_o &= [4(3.7\text{eV}) m^*/3\hbar^2]^{1/2} \end{aligned} \quad (56)$$

$$E_t = [\hbar^2(k_t + k_o)^2/2m^* + \hbar^2 k_z^2/2m_t] \quad (57)$$

### Valence Band Calculation

The valence band calculation for  $P(E)$  proceeds from a determination of the transverse energy. The calculation is simpler from the standpoint that the valence bands are maximal in energy at  $\vec{k}=0$  (i.e. hole energy is minimal at  $\vec{k}=0$ ). Thus, the large transverse momenta, associated with the conduction bands of indirect gap semiconductors such as silicon, are absent here.

We start with the general form of the constant energy surfaces for the valence band. This equation is [8]:

$$E = E_v - (\hbar^2/2m) \times [Ak^2 + [B^2k^4 + C^2(k_x^2k_y^2 + k_x^2k_z^2 + k_y^2k_z^2)]^{1/2}] \quad (58)$$

$$\text{with } A = 4.0 ; B = 1.1 ; C = 4.1 \quad (59a)$$

This yields three effective masses for the valence

band:

$$\begin{aligned} m_1 &= m/(A-B) = m/2.9 ; m_2 = m/(A+B) = m/5.1 \\ \text{and } m_3 &= m/A = m/4 \end{aligned} \quad (59b)$$

Taking the hole energy to be positive downward [47], relabelled  $E'$ , we get:

$$P(E') = \sum_{l=1}^3 [2ef(E')/\hbar(2\pi)^3] \times (2\pi) \times$$

$$\int_0^{k_{mi}} D(E' + E_t + X + E_g) k_t dk_t \quad (60)$$

$$\text{with } k_{mi} = [2m_i E' / \hbar^2]^{1/2} \quad (61a)$$

$$\text{and } E_t = \hbar^2 k_t^2 / 2m_i \quad (61b)$$

or, rewriting in terms of  $E' = -E - E_g$ , gives, for  $E < -E_g$ ,

$$P_{vb}(E) = [2ef(E)/\hbar (2\pi)^3] \times 2\pi \times$$

$$\sum_{i=1}^3 \left[ \int_0^a D(-E + \hbar^2 k_t^2 / 2m_i + X) k_t dk_t \right] \quad (62)$$

$$\text{with } a = [2m_i(-E - E_g) / \hbar^2]^{1/2} \quad (63)$$

#### Predicted Energy Distributions from Si [100]

The equations developed in the previous sections allow calculation of the expected FEEDs from Si. In particular, predictions for the [100] direction appear in Figures 8 through 10. The effect of raising the electron temperature is demonstrated by the broadening of the conduction band peak, demonstrated in Figure 8. Alternatively, the effect of temperature broadening on the valence band emission appears in Figure 9. By raising the Fermi level above the conduction band edge, the conduction band distribution approaches that predicted for a free electron metal, as shown in Figure 10.

In general, for a conduction band only a few tenths of an eV below the Fermi level, the 300K distribution consists of a sharp spike,

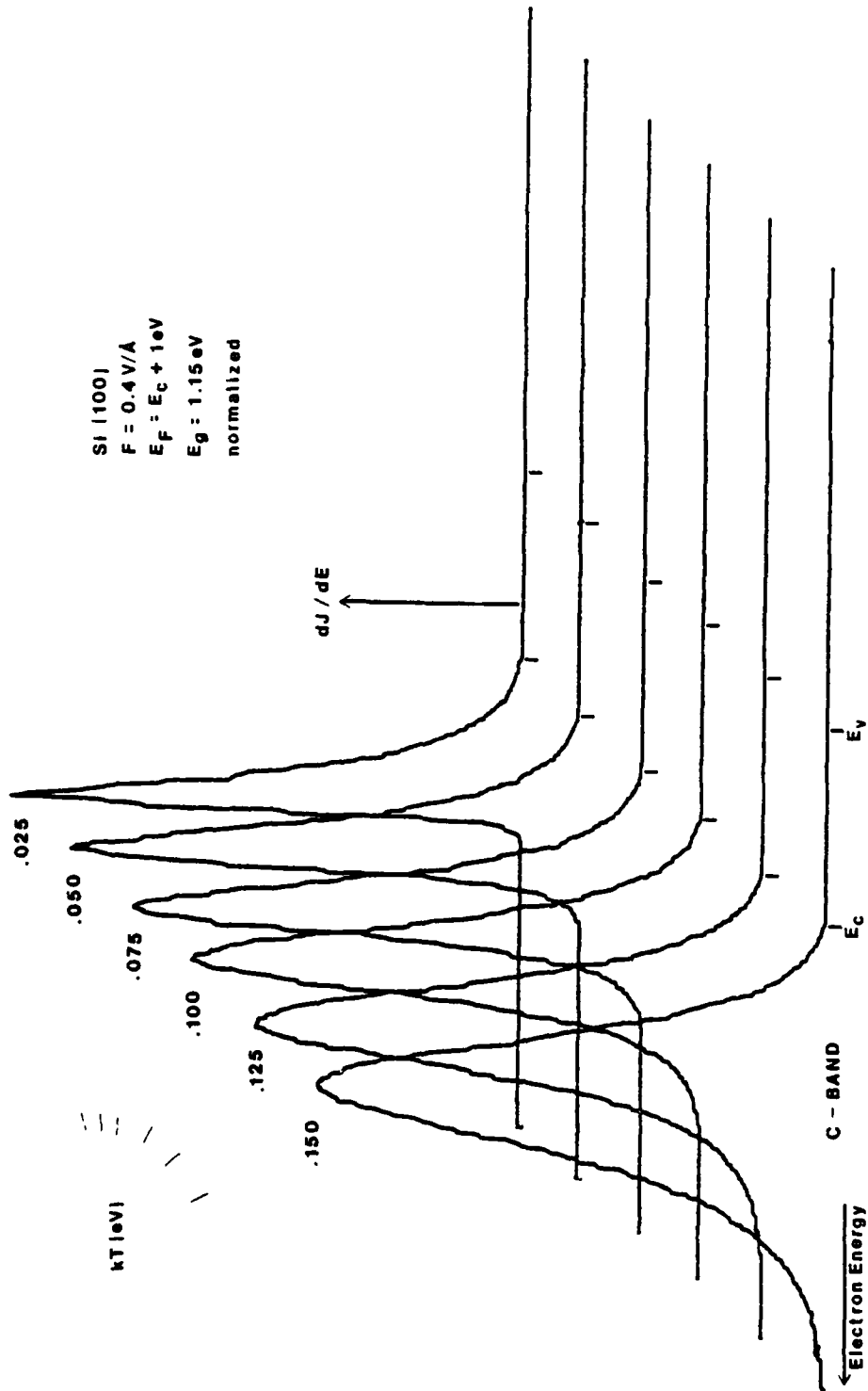


Figure 8. Effect of Temperature on (100) Distribution from Degenerately N-Type Si.

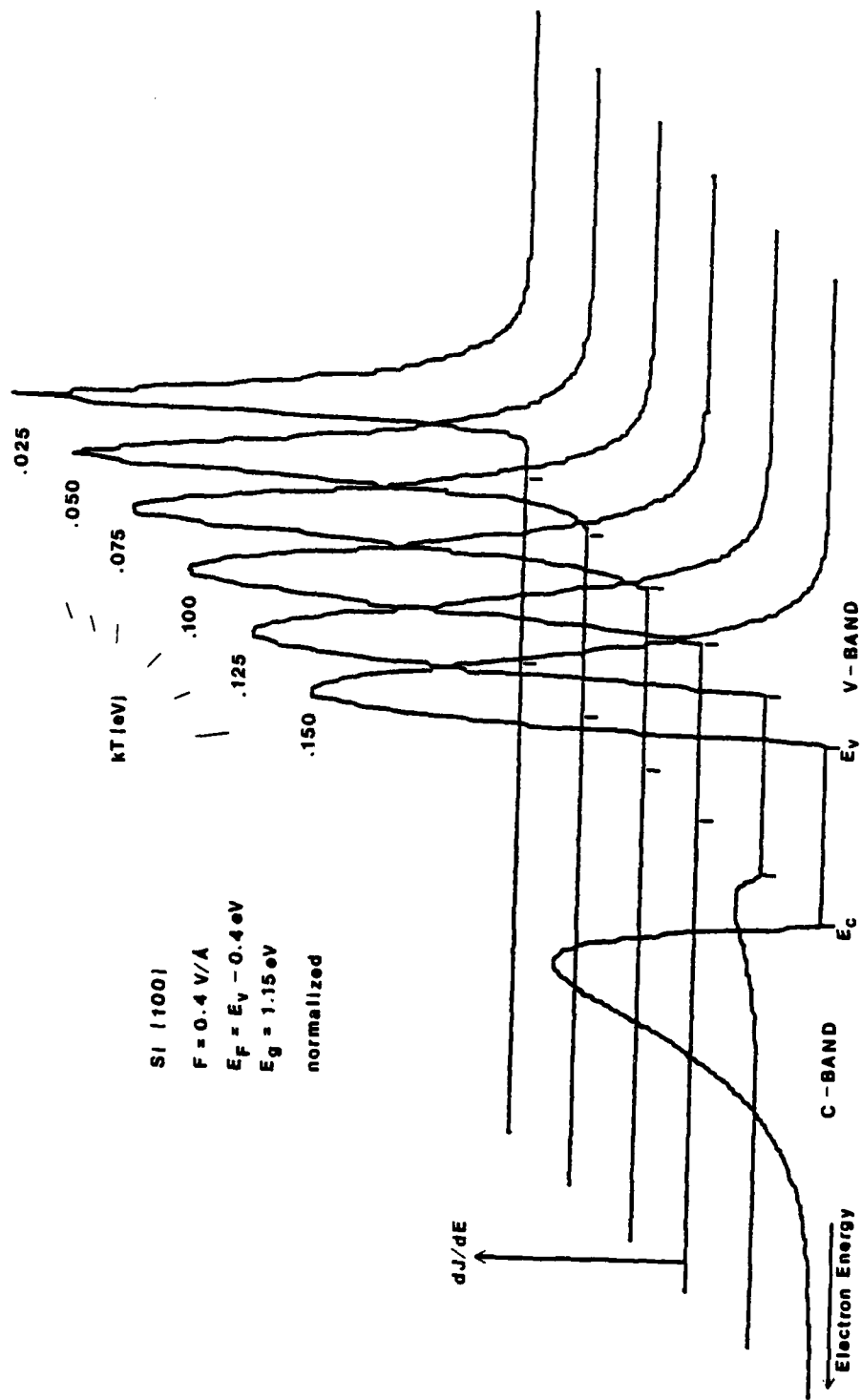


Figure 9. Effect of Temperature on (100) Distribution from Degenerately P-Type Si.

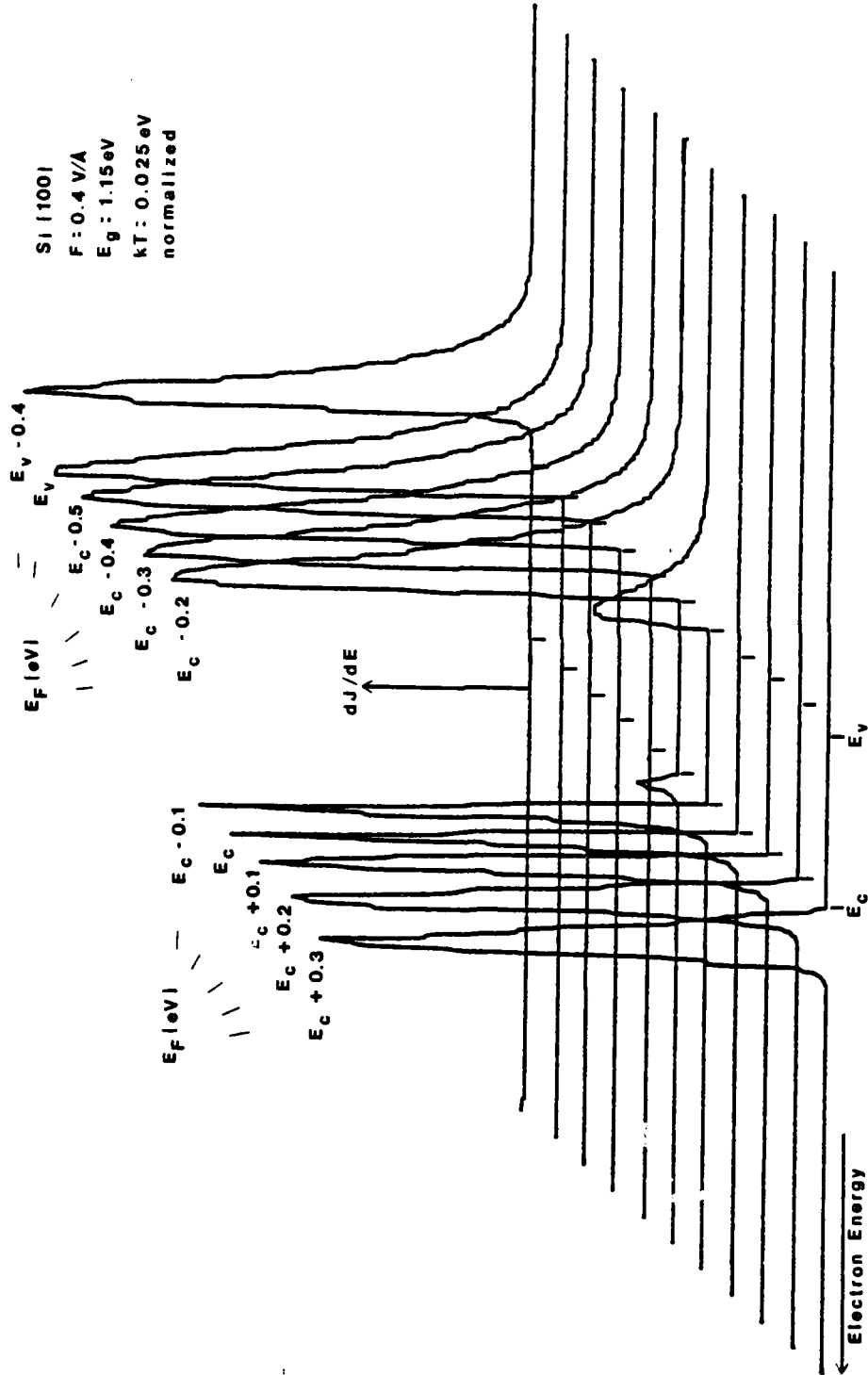


Figure 10. Effect of Fermi Level Position on (100) Distribution from Si at 300K.

evidenced in Figure 10. For the normalized distributions plotted, the valence band will be of low intensity. Of course, for emission directions other than the  $\langle 100 \rangle$  set, conduction band intensity will be greatly reduced. This stems from the non-zero transverse energy terms within the Stratton integrals.

Conversely, the valence band distribution does not change shape if the Fermi level remains above it in energy. In such a case, the valence band contribution only changes amplitude. However, if the Fermi level is positioned within the valence band, the distribution from this band narrows, as demonstrated in Figure 10, where both cases appear.

## CHAPTER III

## APPARATUS AND EXPERIMENTAL PROCEDURES

Mechanical Components

## Vacuum System

An ultra-high vacuum (UHV) system is employed in the FE study. The UHV system is comprised of a stainless steel (ss.) chamber, with components connected to its Cu-sealed flanges. These components are viewports, various ceramic feedthroughs, valves, a "cold finger" sample holder, and a nude Bayard-Alpert ionization gauge. In addition, a sealed palladium tube, silver brazed to a miniConflat flange, is attached to the system. When heated with an alcohol lamp, the palladium tube diffuses hydrogen into the chamber.

The chamber is evacuated by various standard pumps. From atmospheric pressure, the system is initially roughed to  $10^{-3}$  torr by an Edwards Model ED-100 rough pump, via a Varian bakeable mini-valve, mounted below the chamber. The rough pump is then switched to back an Edwards Model EO-2 oil vapor diffusion pump (d.p.). The d.p. utilizes Dow Corning DC-705 pump fluid. A liquid nitrogen cold trap, stationed above the d.p., reduces backstreaming of oil vapor, and is connected to the chamber with a Granville-Phillips 1.5-inch main valve.

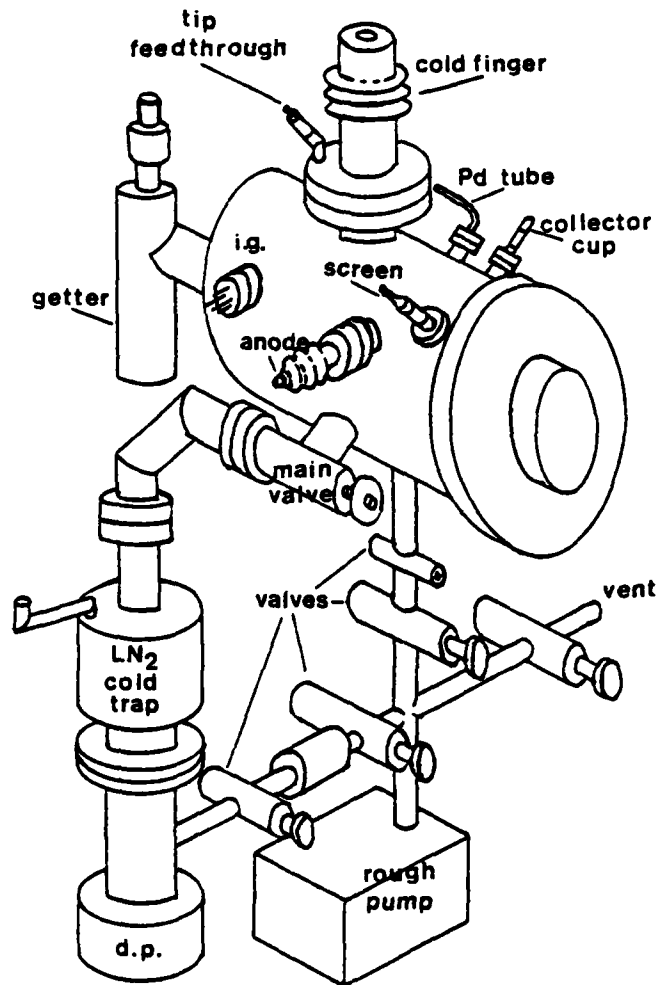


Figure 11. Schematic Layout of Ultrahigh Vacuum System.  
 Here, i.g. refers to the Bayard-Alpert ionization gauge,  
 and d.p. refers to the oil vapor diffusion pump.

Also, attached to the rear of the chamber is a titanium filament sublimation pump, or "getter," which may be cryogenically cooled. A schematic of the chamber and pumping system appears in Figure 11.

After the chamber pressure drops below  $5 \times 10^{-7}$  torr, the system is baked to  $280^{\circ}\text{C}$  for 12 hours under a fiberglass oven. During this bakeout, the getter is "flashed" by passing 45 Amps through the filament for 3 minutes. This effectively degasses the filament and getter walls. Periodically during baking, the getter is similarly flashed. Finally, the heat is switched off and the system is cooled slowly under the oven to reduce thermal strain on the ceramic feedthroughs. The pumps bring the ultimate pressure below  $4 \times 10^{-11}$  torr after one bakeout, as measured with the integral nude Bayard-Alpert ionization gauge.

#### Energy Analyzer

A high-resolution van-Oostrum type electron energy analyzer, chosen for ease of construction and operation, and reproducibility of results, was built by the author. Specifications, published by Swanson and Crouser [53], were modified slightly for mounting and viewing ease in the present UHV chamber. An Au-coated Cu cup comprises the final collector; the rest of the analyzer is constructed of type 304 ss., except the viewing screen composed of phosphor coated Ni foil. Present sizes of the apertures are as follows:

- (a) Screen probe hole: 0.069 inch

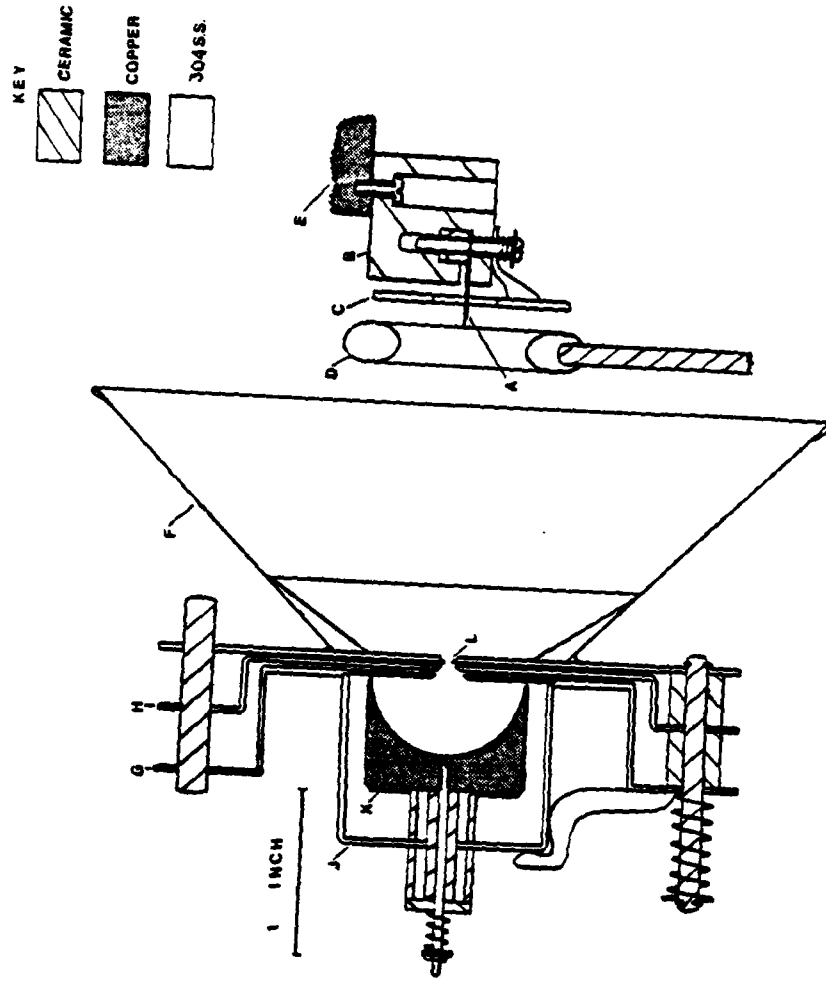


Figure 12. Van Oostrum Energy Analyzer. (A) Sample. (B) Ceramic holder. (C) Guard ring. (D) Anode ring. (E) End of cold finger. (F) Phosphor screen. (G) Faraday cup front. (H) Lens. (J) Detachable Faraday cup. (K) Au coated Cu collector. (L) Probe hole.

(b) Lens: 0.139 inch

(c) Faraday cup: 0.273 inch

The analyzer is shown in cross section in Figure 12.

Though a 10meV resolution was claimed by design, the measured resolution of the analyzer was only slightly better than 110meV, as judged by the Young-Kuyatt criterion [59]. This criterion defines the resolution as the energy difference between the 10% and 90% heights of the leading edge of a  $0^{\circ}\text{K}$  free electron emitter. The resolution was not improved noticeably by the inclusion of magnetic shielding within the UHV chamber. However, the resolution was significantly decreased by the presence of any external magnetic field sources in the vicinity of the chamber; for this reason, no ion pump was installed on the chamber. A typical tungsten calibration run appears in Figure 13.

One of the changes made in the design of the analyzer was to allow the collector Faraday cup to be removed. This allows optical alignment of the analyzer with the tip of the sample. The Ni foil screen was modified from a flat plate into a semi-spherical truncated cone, to reduce distortion of the electron image.

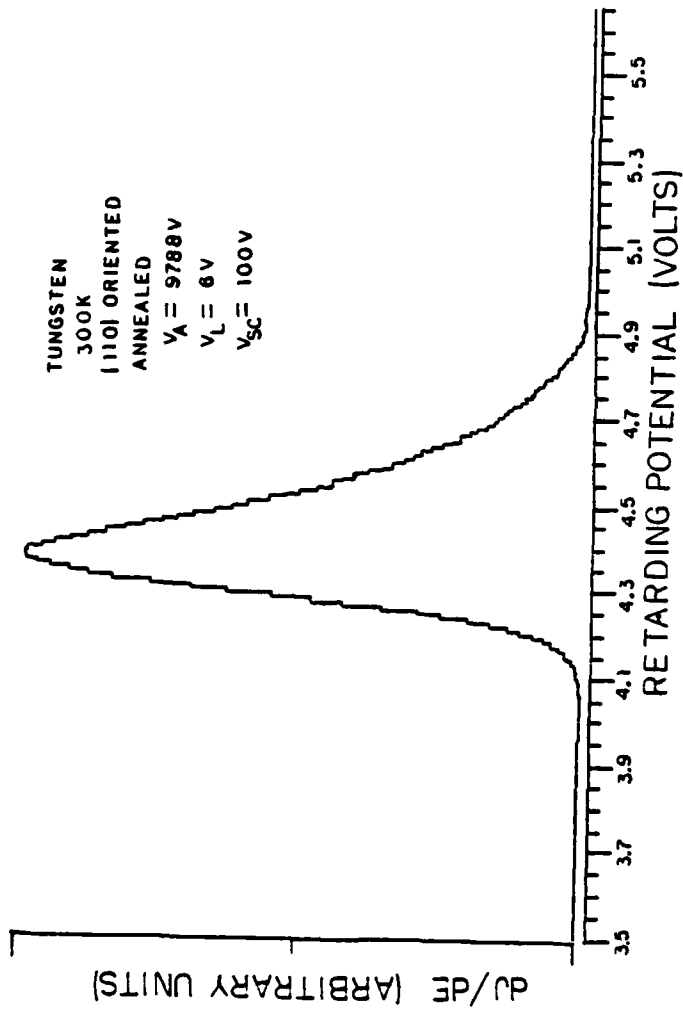


Figure 13. Tungsten Calibration Distribution.

Total Current-Voltage-Light Measurements

Although the energy analysis is computer interfaced, total current measurements as a function of light or anode voltage are recorded manually. In this case, light is supplied to the right side window, normal to the axis of the sample, by a Bausch and Lomb High Intensity Monochromator. The monochromator is comprised of a model BL33-86-39-01 Tungsten (Quartz-Iodine) Light Source, coupled to a model BL33-86-77 digital readout IR Grating. Slits on the monochromator are adjusted for a spectral width of 19nm. Two filters are employed to eliminate the second order from the grating--a #2403 Pyrex filter, with cutoff below 605nm, and a #7-56 Corning filter, with a 900nm cutoff. With these filters, the operational regime of the monochromator is 605nm to 1800nm.

Anode power is supplied by a Computer Power Systems model CPS-100 0-30kV regulated power supply. The output from this supply is applied both to the anode, via the 25kV Ceramaseal feedthrough, and a 200M:200kohm Victoreen resistor voltage divider. The divided anode voltage is measured with a 4.5 digit Data Precision DMM model 248.

Before taking I-V data, the surface of the sample is observed. This is undertaken by applying about 1kV to the phosphor screen of the analyzer. Screen voltage is provided by a Fluke model 408B High Voltage

maintained at about 100-200 volts. At this potential, negligible light intensity is generated by the phosphor, eliminating any photo-stimulation feedback to the sample.

Measurement of the surface potential at constant current is obtained in the following way. As shown in Figure 14, the collector cup is maintained at virtual ground using the Current-to-Voltage Converter (CVC), described in the Electronics section following, to measure the probe hole current. Output from the CVC is monitored on a Data Precision DVM. The anode potential is fixed in positive value. The negative tip potential is varied until a current increase is observed. This value is deemed the "cutoff potential." The tip potential is measured simultaneously using another Data Precision DVM. The cutoff potential, anode voltage, and probe hole current readings are manually recorded. Following these measurements, the total current is measured by applying the sum of the previous anode and offset voltages to the anode ring, and connecting an ammeter to the sample. Again, the sample is thus at "virtual ground" potential.

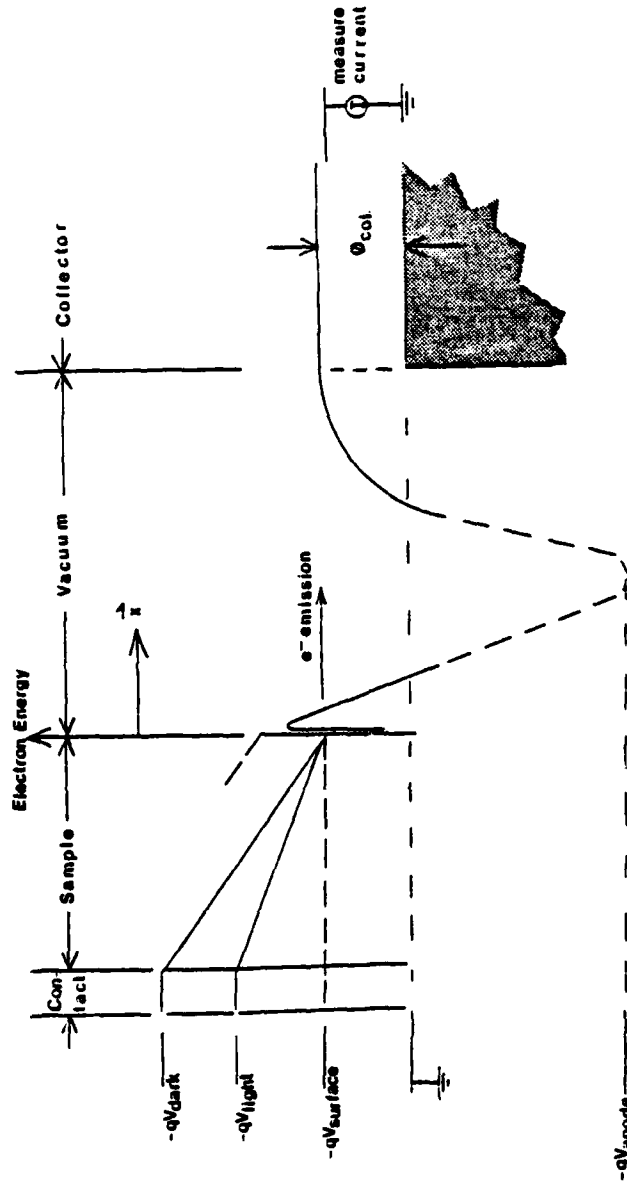


Figure 14. Energy Diagram for Surface Potential Measurements.

## Electronics

### Computer Interfacing

#### Hardware

The energy analyzer is completely run by a microcomputer. This provides rapid data acquisition, uniform and precise measurement, signal averaging, numerical differentiation and smoothing, and data storage. Further, both CRT and plotter outputs are available for rapid viewing or hardcopy output of data.

Outlined in Figure 15 is a flow chart of the hardware interfacing. Beginning with the Apple II microcomputer (uP), decoding of specific address codes sets an initial potential on the retarder supply. The current-to-voltage converter (CVC) measures the resulting current on the retarder cup. This signal is passed through a Butterworth filter and subsequently measured by the ADC, which converts it to a 12-bit binary number. In two operations, the uP reads the number, and adds it to previously accumulated data for the particular energy level.

Various addresses are reserved for special purposes. These address codes are decoded outside the computer and utilized to switch counters, control lines, or, in conjunction with the data bus, to put digital values onto the plotter digital-to-analog converters (DACs).

TABLE 1  
Hardware Addresses and Data Assignments.

Address		Assignment
Decimal	Hexadecimal	
28680	\$7007	V-Min, Byte #4, MSB
28681	7008	V-Min + 2.54mV, Byte #4, MSB
28682	7009	V-Min + 5.08mV, Byte #4, MSB
.		
32768	8000	R, #Readings/2.54mV step
32769	8001	L, #Loops of total voltage range
32770	8002	YA
32771	8003	YB
32772	8004	GA
32773	8005	GB
32774	8006	V1 = Tip voltage, LB
32775	8007	V1, HB
32776	8008	Anode voltage, LB
32777	8009	Anode voltage, HB
32778	800A	Tip type
32779	800B	Month
32780	800C	Day
32781	800D	Year
32782	800E	
32783	800F	Lens voltage/2
32784	8010	Temperature in Kelvin/4
32785	8011	Offset voltage, LB
32786	8012	Offset voltage, HB
32787	8013	
32788	8014	
32789	8015	V-min, LB
32790	8016	V-min, MB
32791	8017	V-min, HB
32792	8018	V-min + 2.54mV, LB
32793	8019	V-min + 2.54mV, MB
32793	801A	V-min + 2.54mV, HB
32794	801B	V-min + 5.08mV, LB
.		

Notes: For data storage, \$7007 to \$79FF and \$8015 to \$BFFF:  
LB = Lowest Byte MB = Next Highest Byte HB = Next Highest Byte  
MSB = Most Significant Byte

For parameters, at the remaining locations in this table:  
LB = Low Byte HB = High Byte

TABLE 1 (continued)  
Hardware Addresses and Data Assignments.

Address		Assignment
Decimal	Hexadecimal	
49410	\$C102	Increment Retarder DAC by 2.54meV.
49412	C104	Reset Retarder to 10eV
49416	C108	Data IB
49417	C109	Data High Nybble
49418	C10A	Reset and Start ADC
49419	C10B	Sample and Hold: Hold
49420	C10C	Sample and Hold: Sample
49421	C10D	Data Bus Diagnostic, = 255
49422	C10E	Data Bus Diagnostic, = 0
49424	C110	North Plotter Motion, 2.54eV increment ↑
49425	C111	Northeast Motion ↗
49426	C112	East Motion →
49427	C113	Southeast Motion ↘
49428	C114	South Motion ↓
49429	C115	Southwest Motion ↙
49430	C116	West Motion ←
49431	C117	Northwest Motion ↖
49432	C118	Pen Up--Not Connected
49433	C119	Pen Down--Not Connected
49434	C11A	Load X HB
49435	C11B	Load X Low Nybble
49436	C11C	Load Y HB
49437	C11D	Load Y Low Nybble
49438	C11E	Clear X
49439	C11F	Clear Y

The address codes used in the present interfacing are presented in Table 1.

The sections of the block diagram are shown in Figures 16 through 21. Each section is described briefly below.

1. Buffers. This wire-wrapped board, shown in Figure 16, slips into the Apple's interface slot #1. It protects the Apple from outside transients, and is powered from the Apple's own power supply. This board contains LS367 chips as unidirectional address bus buffers, and a National Semiconductor #8304 octal data bus transceiver.

2. Decoding and Plotter Control. This wire-wrapped board, shown in Figures 17 and 18, preliminarily reduces the designated 16-bit addresses to manageable 4-bit addresses. The 154 chip, shown in Figure 17, accomplishes this decoding. The addresses go to specific peripherals called by the uP program. In addition, certain addresses are completely decoded (using chips numbered 154 and LS42) to single commands, connected to cascaded 4-bit counters (LS193 chips). These counters drive two 12-bit DACs (Analog Devices AD DAC80-CBIV) for the "X" and "Y" directions of the plotter. The data bus allows any preset number to be placed on these DACs. This circuitry is depicted in Figure 18.

3. Retarder Controller. Shown in Figure 19, this section consists of a transformer isolated power supply and 7.5kV optoisolators, driving an isolated 12-bit DAC (Analog Devices AD DAC80-CBIV). This DAC is connected to provide precise 2.54mV potential steps to the tip through a unity gain 741 Op Amp buffer. Only two controls are utilized--a preset to -10V, and an increment command. The next increment after a

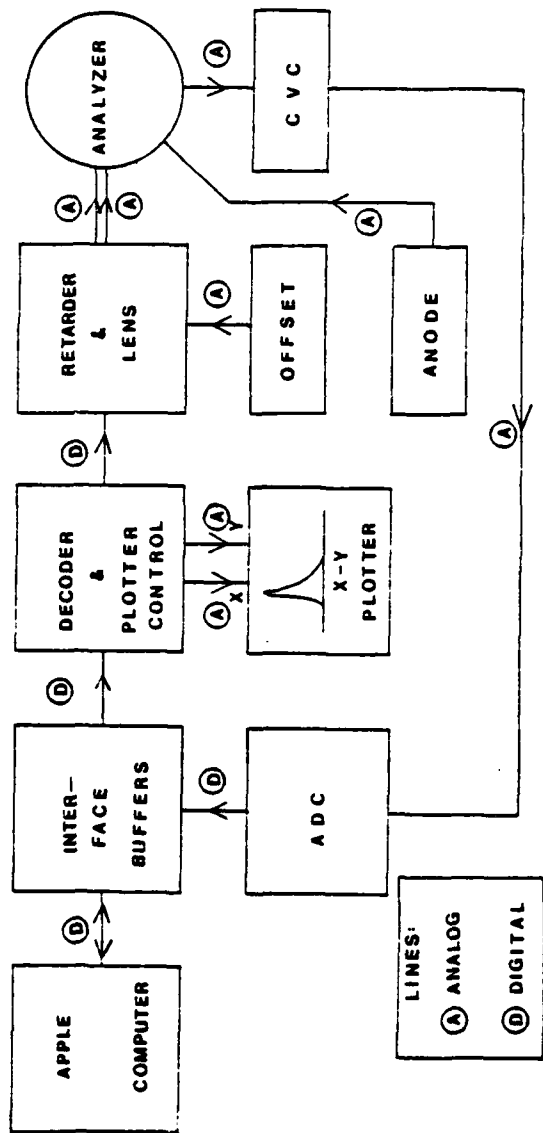


Figure 15. Block Diagram of Electronics.

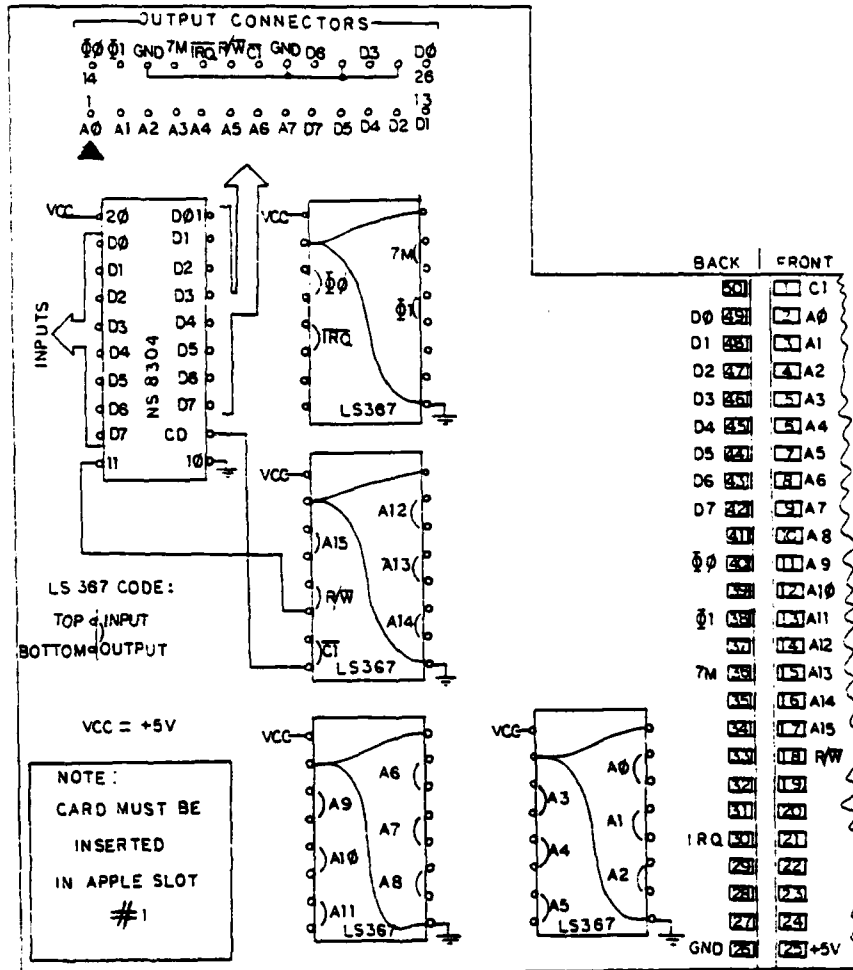


Figure 16. Buffer Board for Apple II Interfacing.

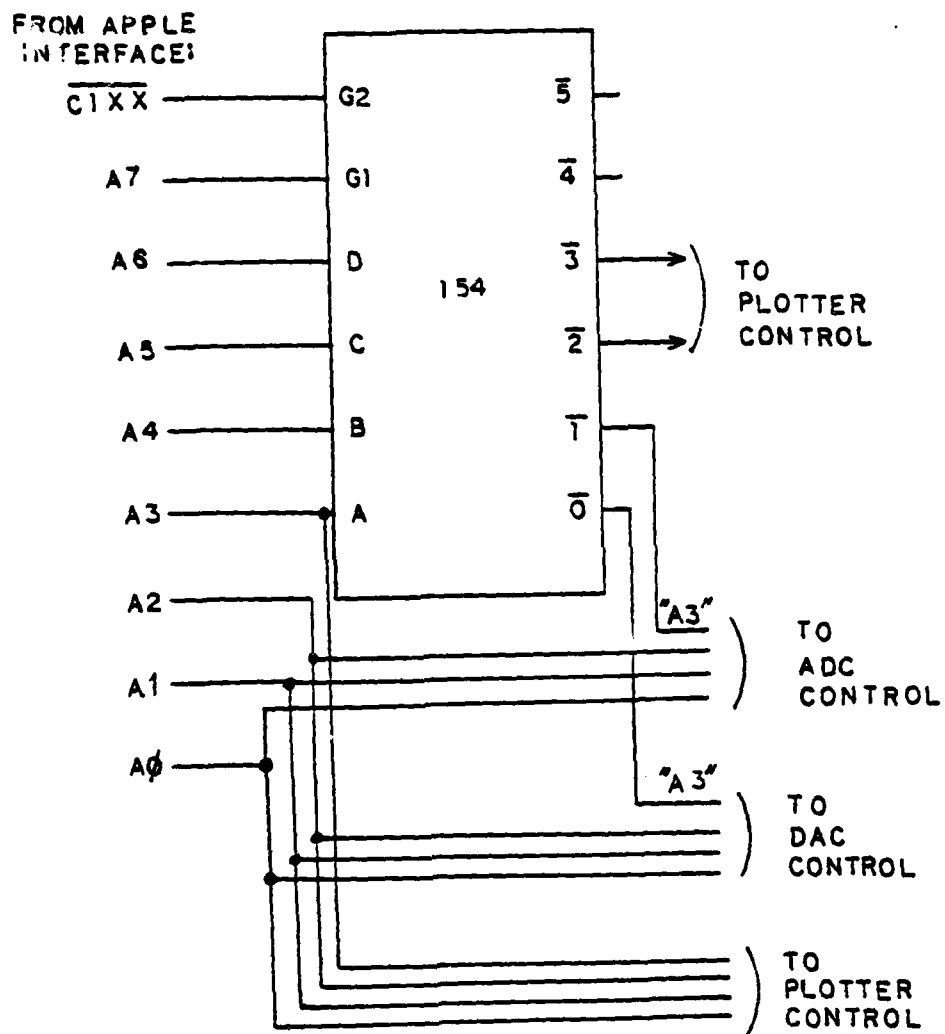


Figure 17. Address Decoding Section.

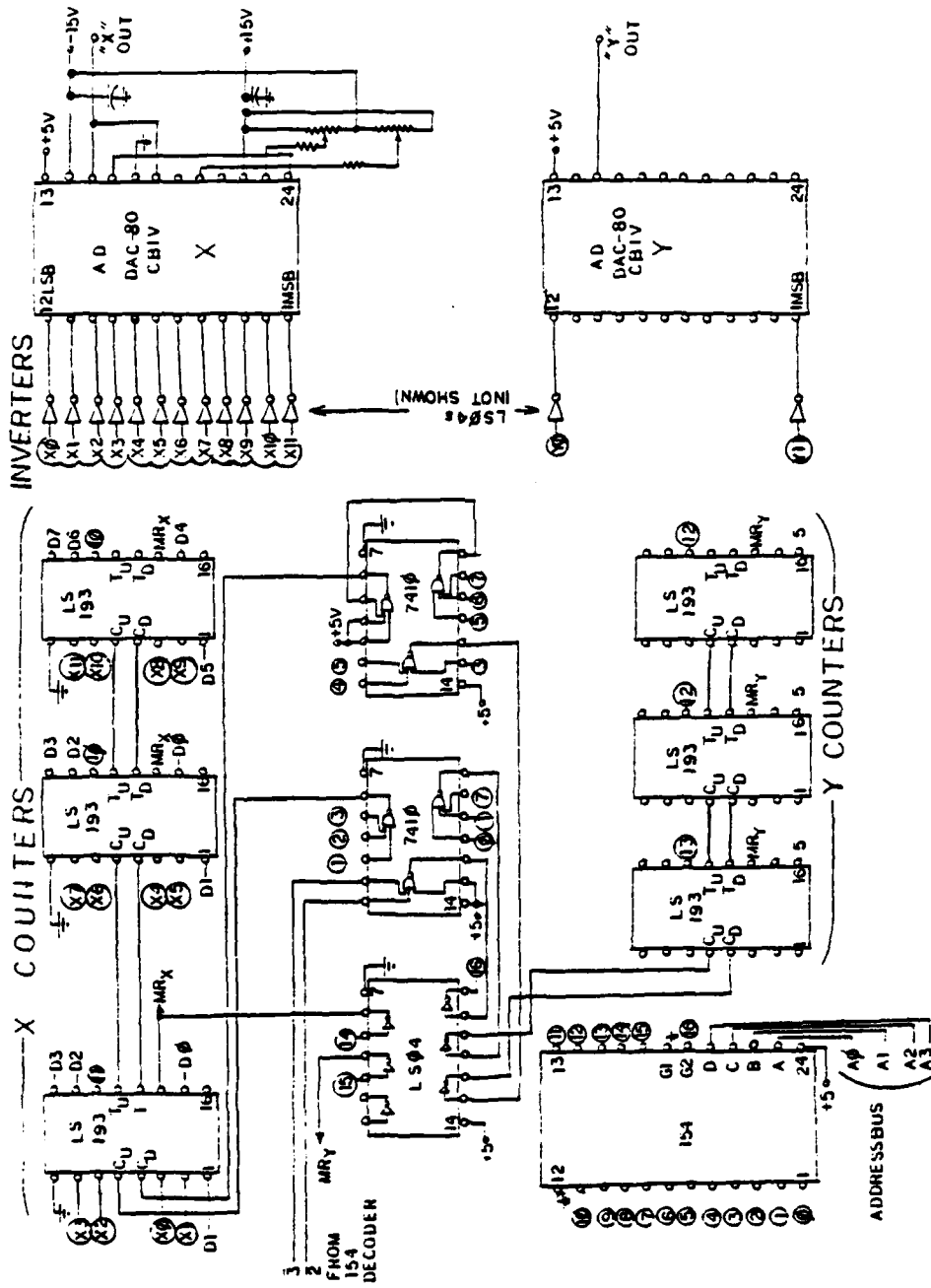


Figure 18. Plotter Controller. Y-side counters connect in analogous fashion as the X-side counters, shown.

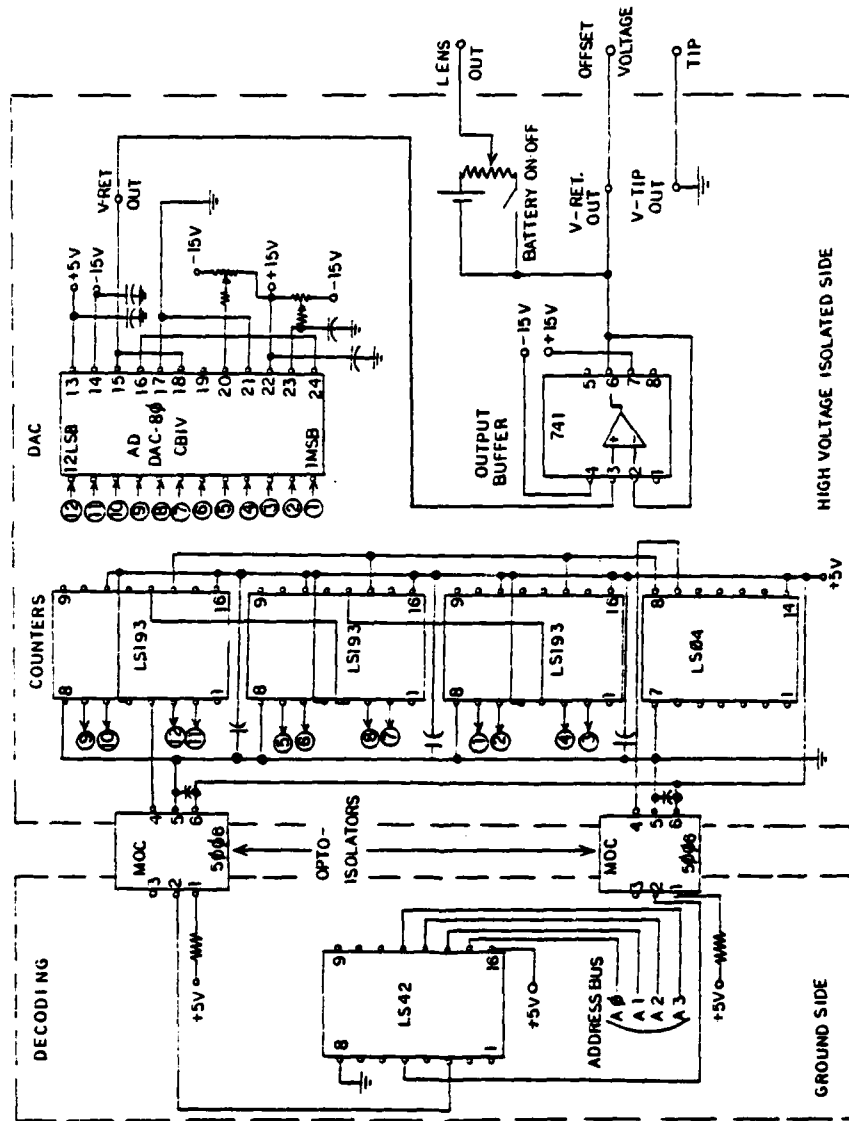


Figure 19. Retarder and Lens Controller.

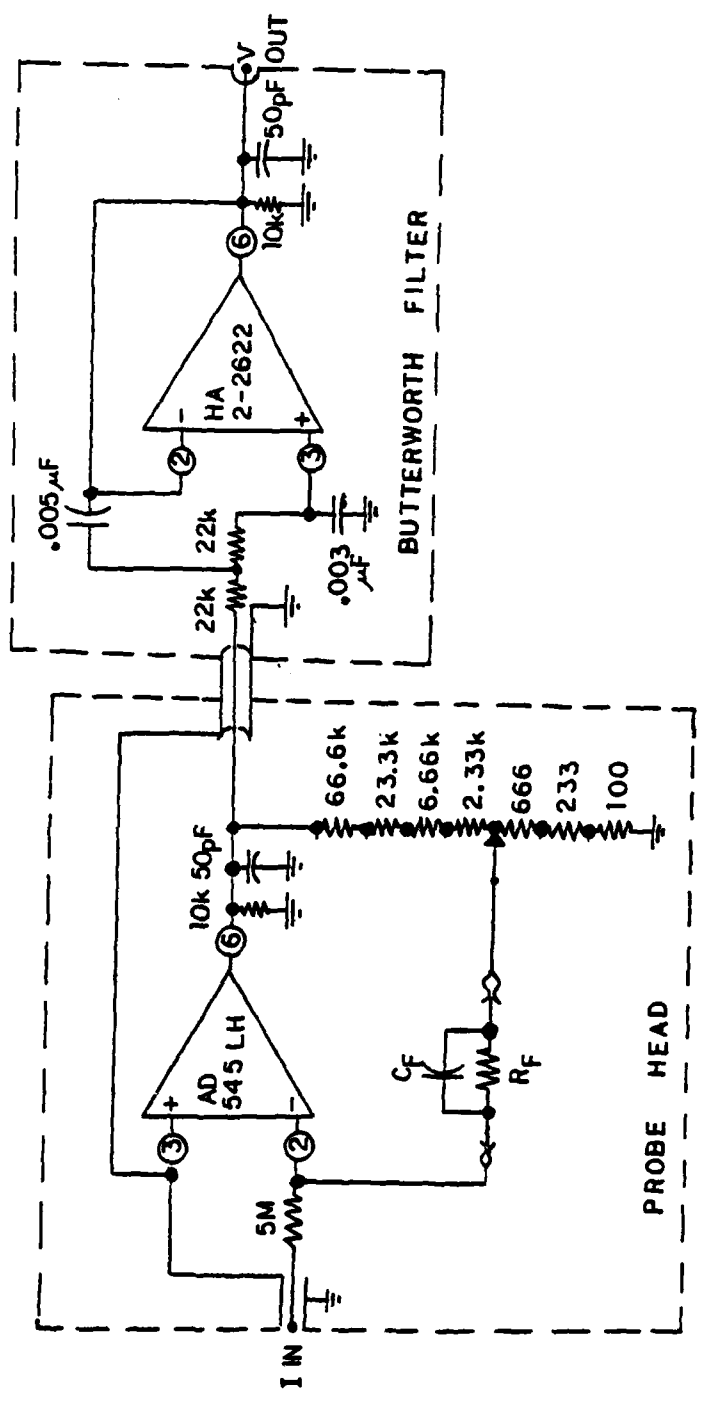


Figure 20. Current-to-Voltage Converter (CVC) and Butterworth Filter.

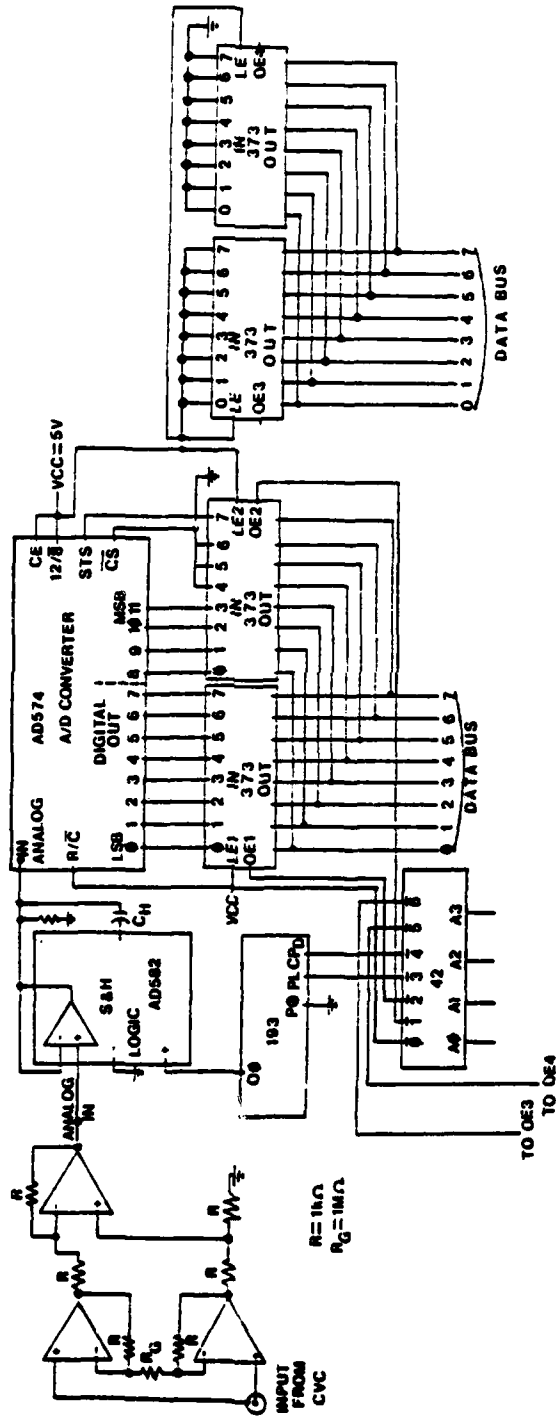


Figure 21. Analog-to-Digital Converter (ADC).

preset command sets the DAC to zero volts.

4. Current-to-Voltage Converter (CVC). The CVC consists of an ultra-high impedance ( $10^{15}$  ohm) precision FET Op Amp (Analog Devices AD545KD) connected in the current-to-voltage converter mode. Mounted on a solid teflon substrate to minimize leakage currents, this CVC features interchangeable feedback resistors  $R_F$ , giving output voltages of  $-I_{in} \times R_F$ . The output from the AD545 is connected to a Butterworth low pass filter. The CVC is illustrated in Figure 20.

5. Analog-to-Digital Converter (ADC). The ADC, shown in Figure 21, is a 12-bit chip (Analog Devices AD574KD), with a sample-and-hold (S&H) on its input. The S&H (Analog Devices AD582KD) maintains the input signal at a constant value during the "read" cycle of the AD574. In front of the S&H are connected three FET input Op Amps in an instrumentation amplifier scheme, to eliminate the common mode present in the ground loop from the UHV chamber to the ADC.

6. Offset. Offset voltage is provided by a Hewlett-Packard model HP6110A regulated DC power supply. The offset compensates for potential differences between the sample surface and ground. The offset need be applied only if the energy distribution cannot be measured with the 10eV range attainable with the bare DAC. Otherwise this point is grounded.

#### Software

The controlling program for data acquisition has two distinct parts. The first, programmed in Basic, allows the user to input

essential experimental information to the computer. This information is requested by the program input statements, and stored along with the actual acquired data for future reference. The date, sample type, lens and anode potentials, offset voltage, and sample temperature are polled, as well as the number of readings (R) and loops (L) desired and starting and ending voltages for each loop. These last two parameters are called YA, YB, GA, and GB in Table 1.

The second part of the control program is in 6502 machine language. Though less interactive with the user, the machine language performs 1000 times faster, and thus provides the necessary data acquisition speed. Multiple precision addition can also be performed easily and rapidly in machine language. The machine program's quadruple precision ability allows for  $2^{32}$  bits of information to be stored for each 2.54meV energy increment, corresponding to  $2^{20}$  full scale readings. This capability remains unused; for most applications, setting the experiment through L=50 loops and R=50 readings suffices. However, for increased data smoothing or large feedback resistances, which require longer settling times, up to R=255 and/or L=255 are possible.

The actual programs are contained on cassette tapes in the laboratory, and in an appendix to the thesis. One merely performs a ]LOAD from the Basic program into the Apple, then flips the tape, types ]CALL -151 to put the computer into a machine language mode, then types \*6B00.6CFFR for reading the tape into the proper memory locations. The user holds the Control button down and hits C to return to the Basic program, then types ]RUN to use the program.

Although most elements of the program are readily prompted by the Basic program, the plotting software is slightly complicated. The complications arise from the fact that the accumulated data appears as  $I(V)$ , and what is desired is  $dI/dV$ . Though this is a simple matter to take  $dI/dV = [I(i+1) - I(i-1)]/2$ , any fluctuations appearing in the original data cause large oscillations in the calculated derivative. To smooth the oscillations, one can change the definition of  $dI/dV$  to

$$dI/dV = [I(i+m) - I(i-m)]/(2m)$$

which reduces the oscillations by the factor  $m$ . The author has found that another manipulation will reduce the oscillations even further. This last method is to average the values at the points  $(i+m)$ , and  $(i-m)$ . Functionally, this amounts to defining  $I(i+m)$  to be

$$I(i+m) = \left[ \sum_{j=-n}^n I(i+m+j) \right] / [2n+1]$$

This implies that  $dI/dV$  should be

$$dI/dV = \left( \sum_{j=-n}^n [I(i+m+j) - I(i-m+j)] \right) / [(2n+1) \times 2m]$$

By appropriately choosing " $m$ ," called the "points to be averaged," and " $n$ ," the "mesh," the data may be smoothed very reasonably without eliminating any inherent characteristics of the energy distributions.

### Sample Preparation

#### Cutting Blanks from Wafers

Two methods have been successfully employed for creation of sample blanks in the "bridge structure" of D'Asaro [14]. The first, useful for thin wafers, of about 10 mils thickness, utilizes photolithography and produces specimens of precise dimensions. The second method, useful for wafers of about 40 mils thickness, relies upon hand cutting on an abrasive disk, glass cutting saw. These two methods are described below.

Before performing either method, the desired crystal orientation is first determined. This may be done by observing the backscattered Laue X-ray pattern, or by utilizing the cleavage characteristics of the sample. It is known, for example, that Si cleaves exclusively along the (111) plane. If one is using  $\langle 100 \rangle$  oriented wafers, the  $\langle 110 \rangle$  direction lies normal to the edge of the cleaved wafer, and is coplanar with the wafer surface. This is illustrated in Figure 22. This procedure eliminates the need to X-ray the samples if  $\langle 100 \rangle$  or  $\langle 110 \rangle$  orientations are desired.

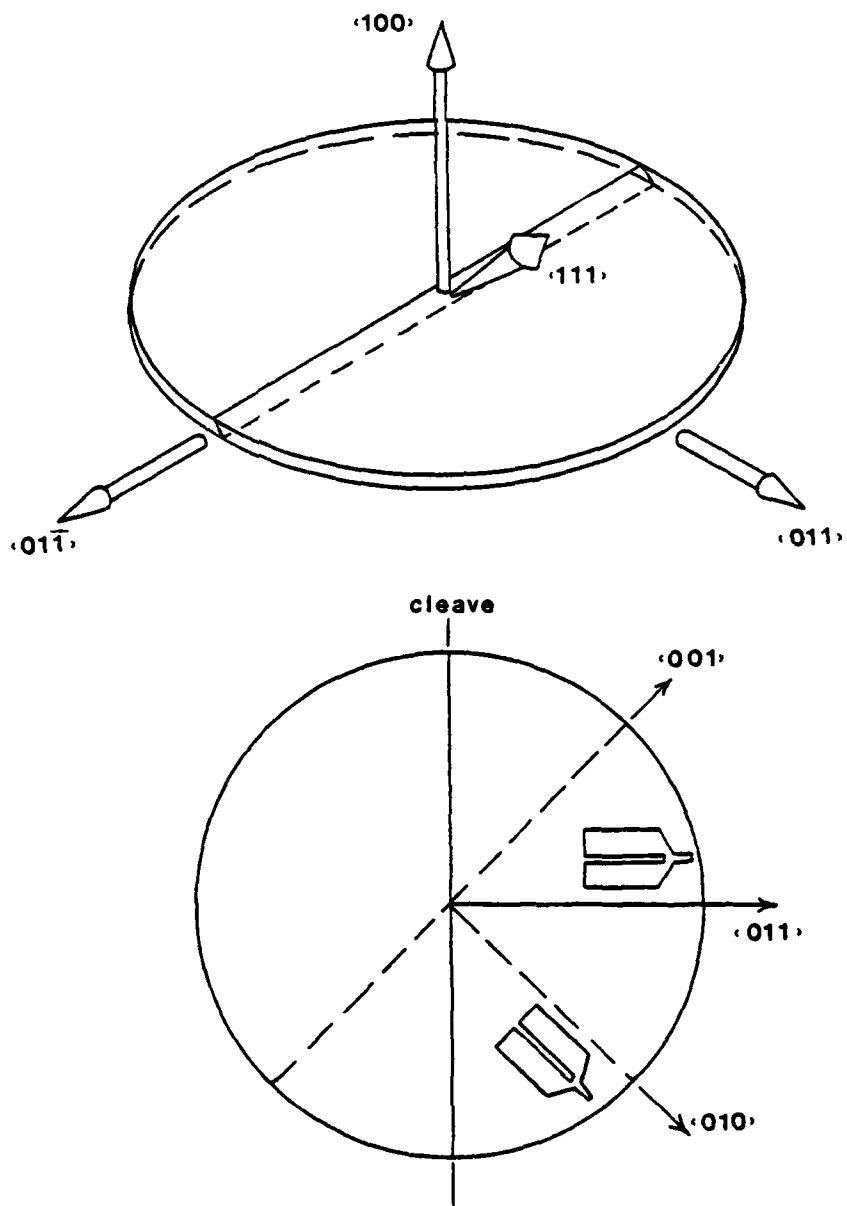


Figure 22. Cleavage Characteristics and Sample Orientation from  $\langle 100 \rangle$ -Oriented Si Wafers.

### Photolithography

Photolithography is a technique used extensively in solid state device manufacturing for precisely aligning and defining circuit elements, using an HF-acid resistant photoresist. The author has adapted this technique for the manufacture of thin, precisely defined Si sample blanks for use in FEM work.

Systematically, the method consists of first coating both sides of each wafer with Shipley AZ-1350 positive resist. The wafers are baked overnight at 90°C in a dry nitrogen ambient for good adhesion to the surface. Next, the wafers are clamped in a jig with two mirror-image contact masks, shown in Figure 23. Both sides of each wafer are exposed through the masks to a high intensity UV source for one to two minutes, depending upon photoresist thickness. Thereon, the exposed wafers are developed in corresponding Shipley developer, rinsed in deionized water (D.I.), and spun dry. The wafers are rebaked overnight as before.

Under a protective hood, one to four wafers are then held vertically in a slotted teflon basket. They are immersed into a plastic beaker of 48% HF, just large enough to contain and cover the wafers. Slowly, several drops of nitric acid are mixed into the beaker. As these acids react with the uncoated Si surface, gas bubbles are evolved and the surface of the Si slowly dissociates. As the surface etches, however, it heats, speeding the reaction. Thus, it is important to keep the wafers immersed in the liquid etchant bath else the resist will peel from the surface. In spite of the best precautions, the resist may

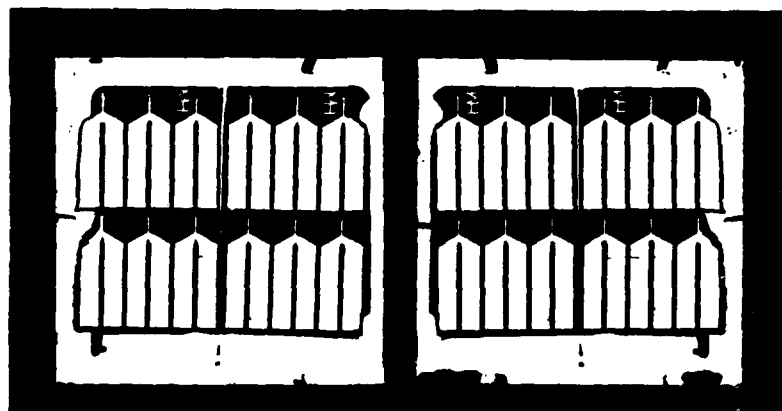
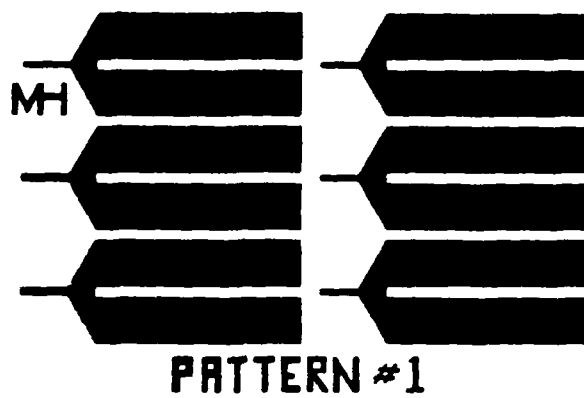


Figure 23. Photolithographic Mask Designs.  
(A) Photograph of Rubylith master.  
(B) Contact prints of front and back masks,  
reduced 20X from master.

begin to peel from the wafers. If this occurs, the wafers must be removed, cleaned, and recoated with resist.

When etching is complete, samples float to the surface of the acid bath, and are retrieved with a pair of tweezers. Subsequently, they are rinsed in D.I. water, then in acetone to remove the Shipley resist, and finally in D.I. water.

These samples are now sandblasted gently to round the tip end. After this treatment, the samples are etched electrolytically, as described in the next section.

#### Abrasive Cutting

This technique provides roughly equivalent, rapidly generated samples. It requires wafers of standard 4-inch diameter thickness, about 40 mils. Typically, one such 4-inch wafer is scribed and broken into quarters. Then these are cemented onto a 3/16-inch thick glass substrate with melted Cenco red wax. The glass and four stacked quarters are cut by hand on a standard glass-cutting abrasive wheel saw. The glass substrates and Si blanks are heated and the wax blotted off, then the blanks are cleaned in acetone. Finally, the tip ends of the blanks are sandblasted round. The rounding is necessary because the etching action is isotropic--elliptical cross sections are etched into "butter knives" with one dimension sharp and the other blunt.

### Electrolytic Etching

Electrolytic etching, rather than purely chemical etching, must be used for creation of successful, utilizable tips. Best results are obtained using the techniques described by Busch and Fischer [11], who suggest optimum ratios of HF:HNO<sub>3</sub> for various dopings of Si. In general, the ratio is 3:5 for resistivities greater than 10 ohm-cm, and drops to 1:10 for resistivities of 0.1 ohm-cm or less. Equally important is the use of a variable AC voltage supply, with a platinum wire immersed in the acid bath and another electrode attached to the Si sample. The voltage is regulated until small bubbles appear at both sample and Pt wire electrodes. This voltage may vary from a few tenths of a volt for high conductivity samples to 60 or more volts for nearly intrinsic samples. Lastly, the sample is rinsed in D.I. water, dried with compressed nitrogen, and stored in a closed container.

The electrode-to-Si contact must be excellent to assure consistent results. To this end, the author always strips the oxide from the "legs" of the sample with etchant, rinses the sample, then attaches a strong, flat clip. Loss of etching activity is almost always attributable to poor electrode-to-sample contact.

### Prevacuum Processing

Just prior to installation in the UHV system, a previously etched tip is removed from the closed container and given an "RCA clean." This consists of first a 4-minute dip in boiling  $\text{NH}_4\text{OH}:\text{H}_2\text{O}:\text{H}_2\text{O}_2$  (4:10:1), followed by a rinse in D.I. water. Secondly, the sample is dipped into boiling  $\text{HCl}:\text{H}_2\text{O}:\text{H}_2\text{O}_2$  (4:10:1), and again rinsed in D.I. water. Lastly, the sample is dipped in 48% HF, rinsed twice, and dried. After insertion into the cold finger tip holder, a resistance measurement between the tip feedthroughs indicates the contact resistance. If considered too high, another dip in HF and rinse usually eliminates the problem.

### In-Vacuum Processing

Once the sample has been mounted in the chamber, the system is pumped out. The procedure for evacuation is described in the section entitled "Vacuum System." After low  $10^{-11}$  torr has been obtained after bakeout, the experimenter is able to clean the sample with the following technique.

With pure hydrogen admitted through the sealed Pd tube to a pressure of  $10^{-3}$  torr, a novel method is employed to clean the Si. Following the work of Busch and Fischer [11], who described a faintly visible DC field desorption image of Si in  $\text{H}_2$ , the author performs

an AC field desorption-field emission cleaning. This method allows a better view of the surface cleaning than the DC desorption technique. Following Cooper and Muller [13], who first used the technique to clean tungsten in vacuum, an adjustable high voltage AC is applied to the tip while an adjustable negative DC voltage is applied to the ring "anode" of the analyzer. A positive voltage of 3 kV is put on the phosphor screen. The resulting field at the sample surface oscillates between field emission and field desorption. The field emission gives the experimenter an excellent view of the sample surface as the cleaning is occurring. The  $H_2$  reacts with the silicon dioxide during desorption, enhancing the removal of this strongly bonded impurity, and exposes the silicon surface.

While the AC field is on, the  $H_2$  is pumped out. After a short time, the AC is cut off, and the system is again baked. This second bakeout leaves the system in low  $10^{-11}$  torr. At this point, another AC field desorption-field emission cleaning is performed, this time in vacuum without hydrogen.

If the "RCA clean" procedure, outlined in the section on prevacuum processing, is followed rigorously, the author has found that the hydrogen reaction described above may be eliminated altogether. This allows the experimenter to maintain a sharp tip from the onset, and obviates the extra bakeout required with the hydrogen cleaning.

If annealing is desired, a current is passed through the tip "legs," and the sample is resistively heated and annealed. As Si has a negative coefficient of resistance, ballast protection resistors must be used for high resistivity samples [43]. For low resistivity samples, a

transistor-regulated constant-current power supply suffices to heat the sample, automatically adjusting for resistance changes.

## CHAPTER IV

## EXPERIMENTAL RESULTS

Results of the experimental measurement of the field emission energy distribution (FEED), and Fowler Nordheim current-voltage (F-N) plots, from silicon of various dopings are presented in this section. It was observed by the author that surface conditions, as well as temperature and doping, affected the results. For this reason, photographs of the various surface conditions are presented in Figure 24.

Lightly Doped Silicon

## Energy Distributions

One of the main objectives of the thesis was to ascertain obvious differences in the FEED of Si under PFE conditions. To this end, samples were cut from very pure p-type Si wafers. These samples yielded results typified in Figure 25. The FEEDs obtained from these samples were characteristically wide ( $\text{FWHM} > 0.75\text{eV}$ ) and Gaussian in shape at both 300K and 78K. Further, the FEED generally contained large, non-reproducible fluctuations in amplitude at points of the distribution. The only obvious difference in the FEED, between light and dark conditions, is the offset potential. There are no distinguishing differences in the shapes of the distributions, even though the PFE

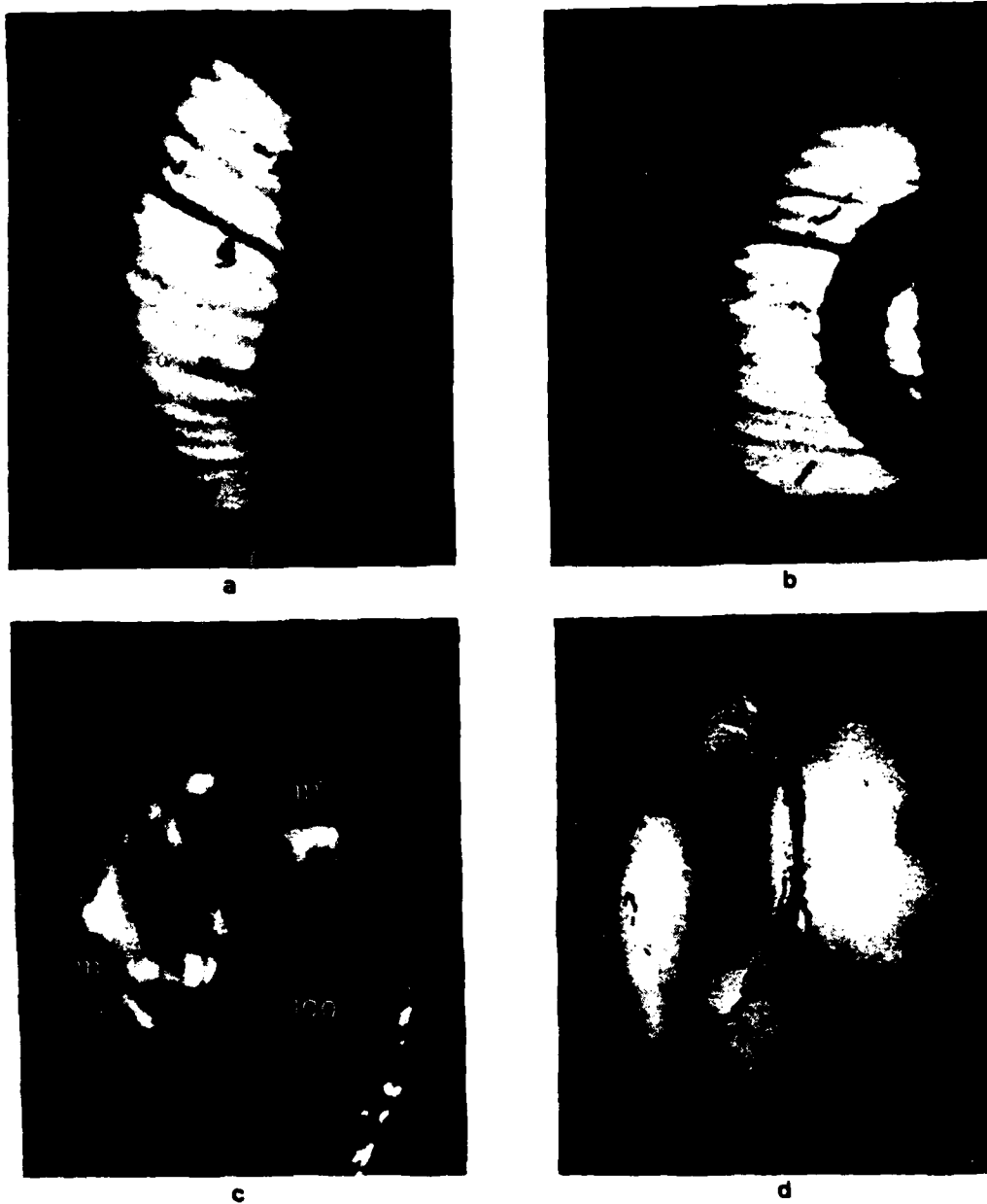
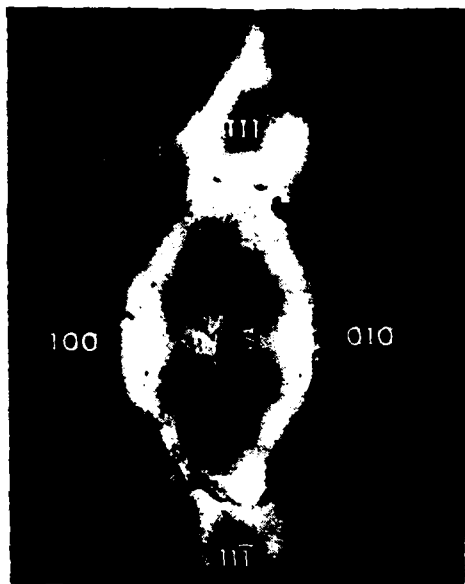


Figure 24. Various Surface Conditions Observed for Emitters.  
(a) N-type, 0.001 ohm-cm, field desorbed, (110) oriented, side view.  
(b) Same as (a), rear view.  
(c) P-type, 60-100 ohm-cm, thermally annealed, (110) oriented, side view.  
(d) Tungsten, thermally annealed, (110) oriented, side view.



e



f



g



h

Figure 24 (continued).

- (e) N-type, 0.001 ohm-cm, thermally annealed,  
(110) oriented, side view.
- (f) Same as (e), rear view.
- (g) P-type, 60-100 ohm-cm, field desorbed,  
(110) oriented, rear view.
- (h) Same as (g), thermally annealed at  $T < 700^\circ\text{C}$ ,  
(110) oriented, rear view, showing ring formation.

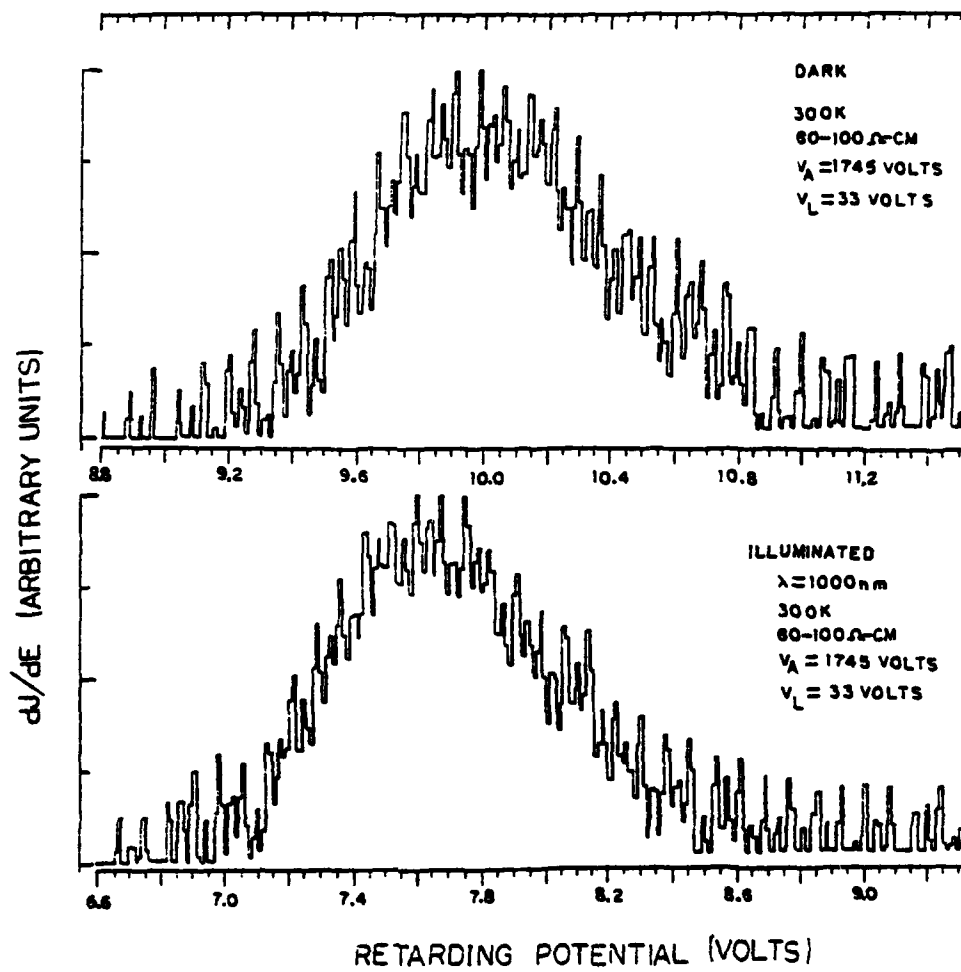


Figure 25. Illuminated vs. Dark FEEDs from High Resistivity P-Type Si.

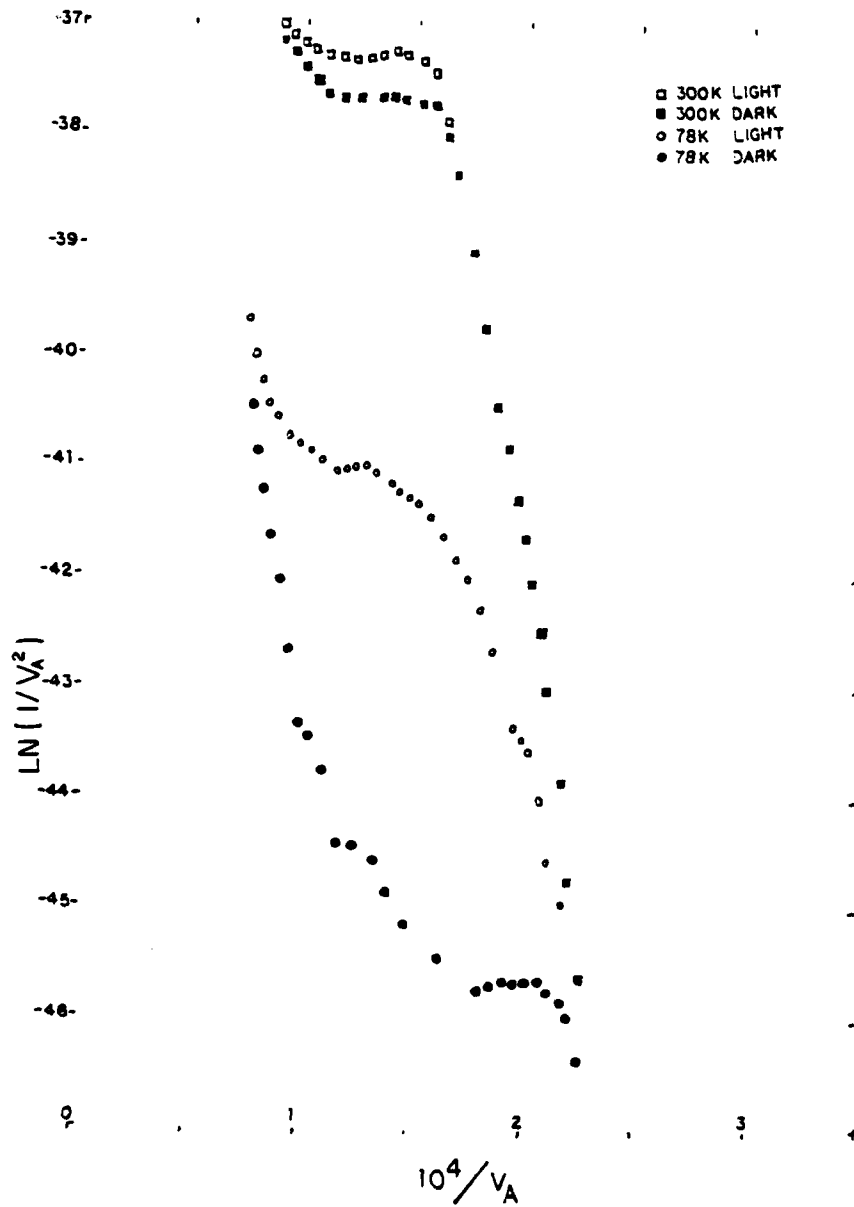


Figure 26. Photo-Field-Emission (PFE) Fowler-Nordheim Plot.

TABLE 2  
Photo-Field Emission Surface Potential Measurements.

Anode-Surface Voltage (Volts)	Base Contact-Surface Voltage (Volts)		Total Emitter Current (Amps x 10 <sup>+10</sup> )	
	Dark	Light	Dark	Light
1650	7.1	6.7	2.40	2.41
1680	9.5	8.7	3.30	3.40
1710	12.0	11.0	4.18	4.35
1740	19.0	17.0	4.90	5.20
1770	25.5	23.7	5.50	5.95
1800	32.6	31.5	6.00	6.40
1830	41.5	39.9	6.41	6.85
1860	49.0	47.6	6.80	7.23
1890	58.6	56.9	7.20	7.70
			Scale Change (Amps x 10 <sup>+9</sup> )	
			0.75	0.81
1920	68.0	65.8	0.77	0.84
1950	76.0	73.8	0.82	0.87
1980	85.7	85.7	0.85	0.92
2010	93.9	92.4	0.87	0.94
2040			0.92	0.97
2070	109.5	107.4	0.94	1.00
2100	118.2	116.3	0.97	1.04
2130	127.0	125.7	1.00	1.06
2160	138.3	135.3	1.03	1.08
2190	146.0	144.0	1.05	1.12

Notes: Light source: B&L High Intensity Monochromator.

Setting: 1000mm.

Filter: Pyrex #2403.

Sample: 60-100 ohm-cm p-type.

Temperature: 300K.

Surface: Field desorbed.

Pressure:  $2 \times 10^{-11}$  torr.

current at 78K, with photo-stimulation, was usually several orders of magnitude larger than the dark current.

Using the FEED to determine the offset potential, the author measured the  $I-V_{\text{offset}}$  relation of the sample. At various fixed offset potentials, the PFE current was always slightly higher than the dark current at the same offset potential. Data on this effect is presented in Table 2.

This FEED information may indicate several possibilities. The wide energy distributions, accompanied by fluctuations, appear to indicate some non-equilibrium situation. Indeed, various researchers have argued that the width is indicative of hot electron effects in the sample. Distributions up to 4eV in width were reported by Kagan, et al. [32]. As pointed out by Stratton [52], this implies that these electrons have energy larger than the barrier height and that a complete reformulation of field emission theory is then necessary.

#### Current-Voltage-Light Characteristics

Fowler-Nordheim plots of data from lightly doped p-type Si follow the same pattern regardless of surface condition. An example is shown in Figure 26. However, the ratio R of photostimulated current to dark current at 300K is highest for the field desorbed surface. The effect of slight annealing at  $T < 700\text{C}$  is the formation of a ring on the previously desorbed surface, and a consequent reduction in R, from 1.68 to 1.42. This surface is shown in Figure 24g. The Current-Voltage plots illustrating this effect appear in Figure 27.

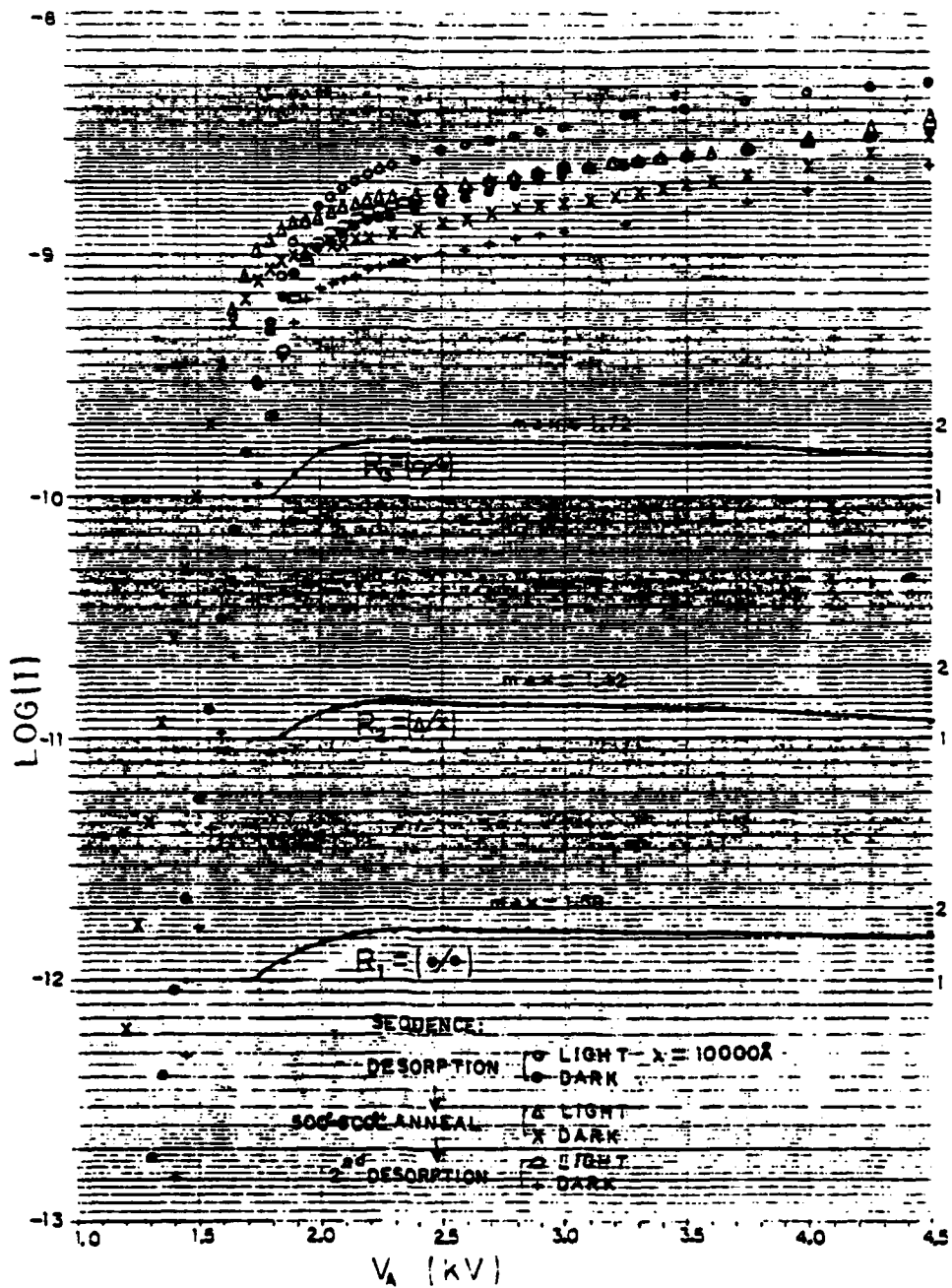


Figure 27. Effect of Surface Condition on FFE Light/Dark Current Ratio.

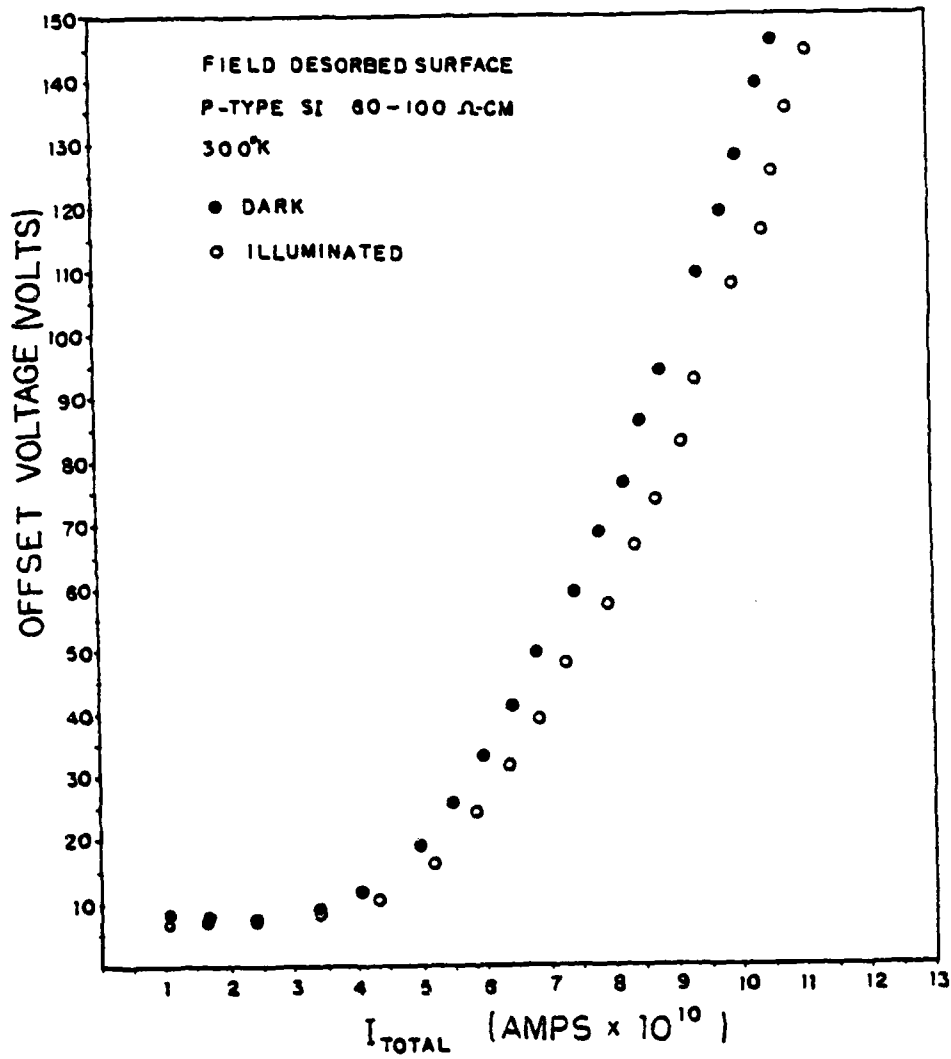


Figure 28. PFE Offset Voltage as a Function of Total Current.

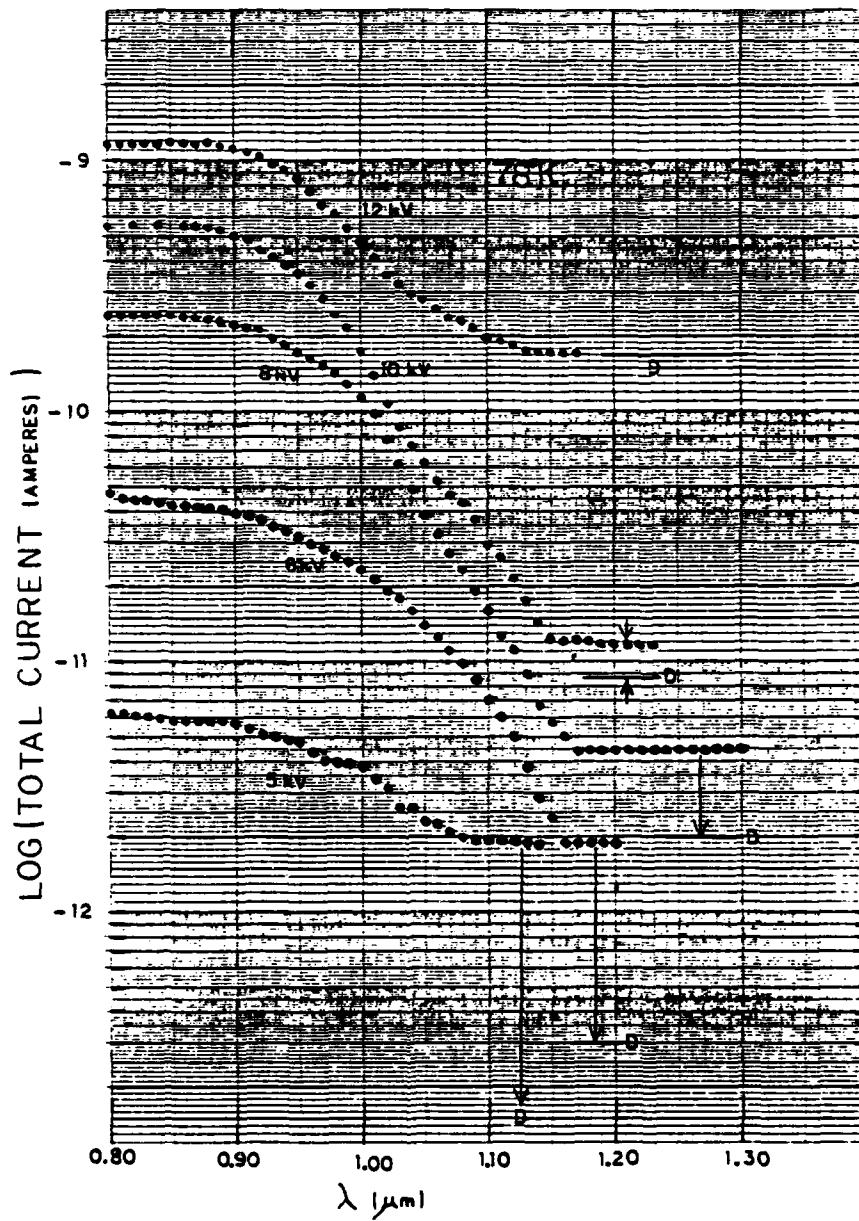


Figure 29. 78K PFE Current as a Function of Illumination Wavelength at Fixed Applied Voltage. "D" denoted dark current level. Voltages denote applied anode potential. Monochromator spectral width: 19nm.

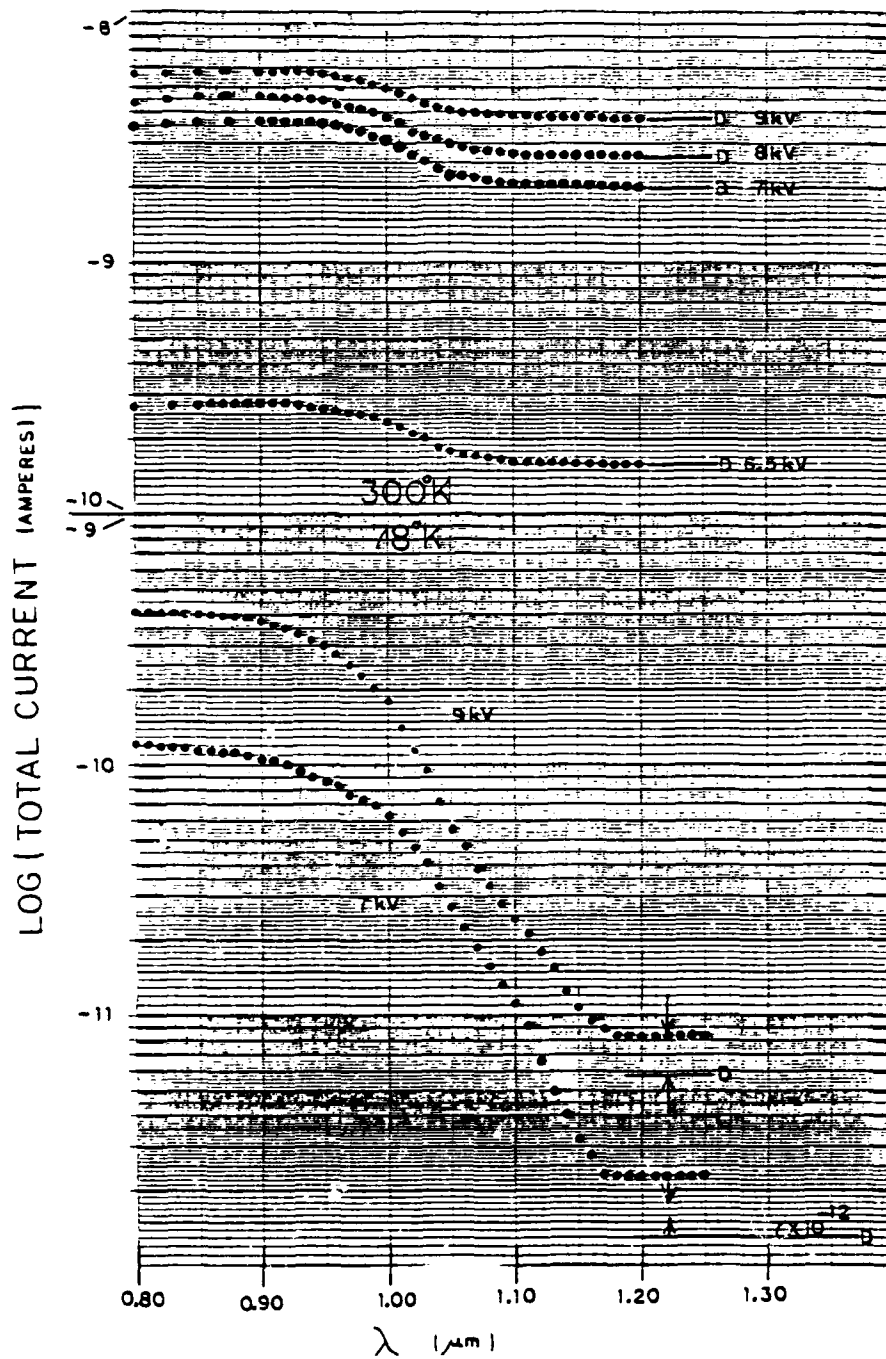


Figure 30. 300K and 78K PFE Current as a Function of Illumination Wavelength at Fixed Applied Voltage. "D" denotes dark current. Voltages denote applied anode potential. Monochromator spectral width: 19nm.

Also, the offset potentials, or IR drops, indicated non-ohmic behavior, with resistances of up to  $10^{12}$  ohms at 300K, as indicated in Figure 28.

Additionally, the PFE increase varies with wavelength and field. This behavior is demonstrated in Figures 29 and 30, with Log of Current vs. Illumination Wavelength at fixed values of  $V_A$ . As indicated, the photocurrent is substantially larger at fixed  $V_A$  for photon energies larger than the thermal band gap. Nevertheless, residual enhancement does exist at 78K for photons of energy down to 1.03eV, corresponding to 1200nm. As discussed by Borzyak, et al. [10], this residual enhancement may be due to absorption by carriers in surface states, or perhaps by free carrier or impurity absorption.

### Heavily N-Doped Silicon

#### Energy Distributions

Because the FEED studies on lightly doped Si showed no obvious differences in energy structure, the author decided to elicit information from more heavily doped samples. It was hoped that the increased doping would eliminate the large offset voltages and current fluctuations accompanying the previous data. Further, it was expected that the heavily n-doped Si used (0.001 ohm-cm resistivity,  $10^{19}$  per  $\text{cm}^3$  Sb doped) would show a metallic energy distribution and provide a starting point for further data comparison.

These expectations were largely unfulfilled. Although current

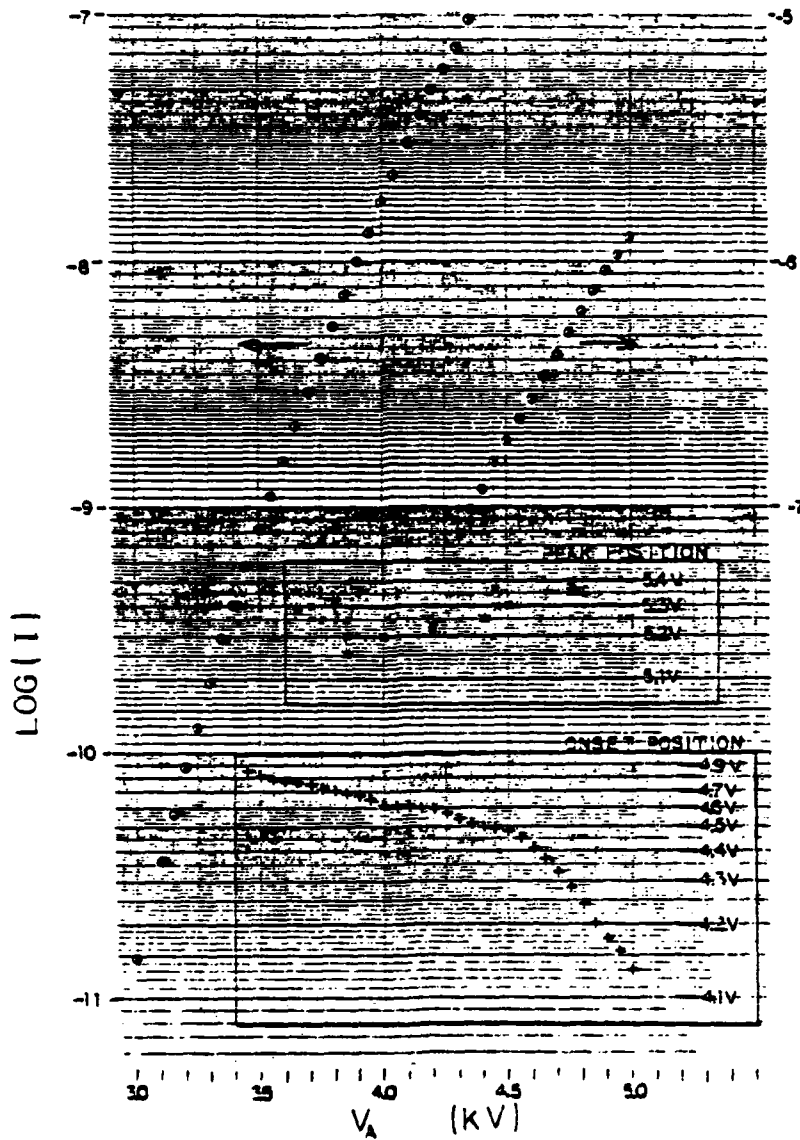


Figure 31. Onset, Peak Position, and Total Current as a Function of Applied Voltage for Heavily N-Doped Si. Temperature = 300K.

fluctuations were eliminated for desorbed or annealed samples, the zero offset distributions expected for metallic emitters were never observed. Attempts to connect the non-zero offset voltage to an IR drop were completely unsuccessful. Indeed, the "onset" potential, defined by the author to be the offset voltage yielding  $10^{-13}$  Amp probe hole current, actually decreased with increasing total tip current. This behavior is shown with the current-voltage data, in Figure 31.

#### Field Desorbed Surface

The field desorbed surface, shown in Figure 24b, yielded reproducible FEED results. These results appear in Figures 32 and 33. The energy distributions may be characterized as follows [28]:

(a) 300K: A single peak, which shifts downward in energy and broadens with increasing field. The peak is initially about 0.4eV below Fermi level.

(b) 78K: The single peak broadens and shifts as in (a), but at some particular field there arises a subsidiary peak from below the Fermi level. The subsidiary peak increases in magnitude with respect to the larger, low energy peak.

#### Thermally Annealed Surface

Thermally annealed surfaces show little general qualitative differences to the results from desorbed surfaces at 300K in that both types show an energy shift. FEEDs performed on the surface shown in Figure 24e yielded a single peak, which shifted down in energy with increasing field. The FEED measurements made from the annealed surface,

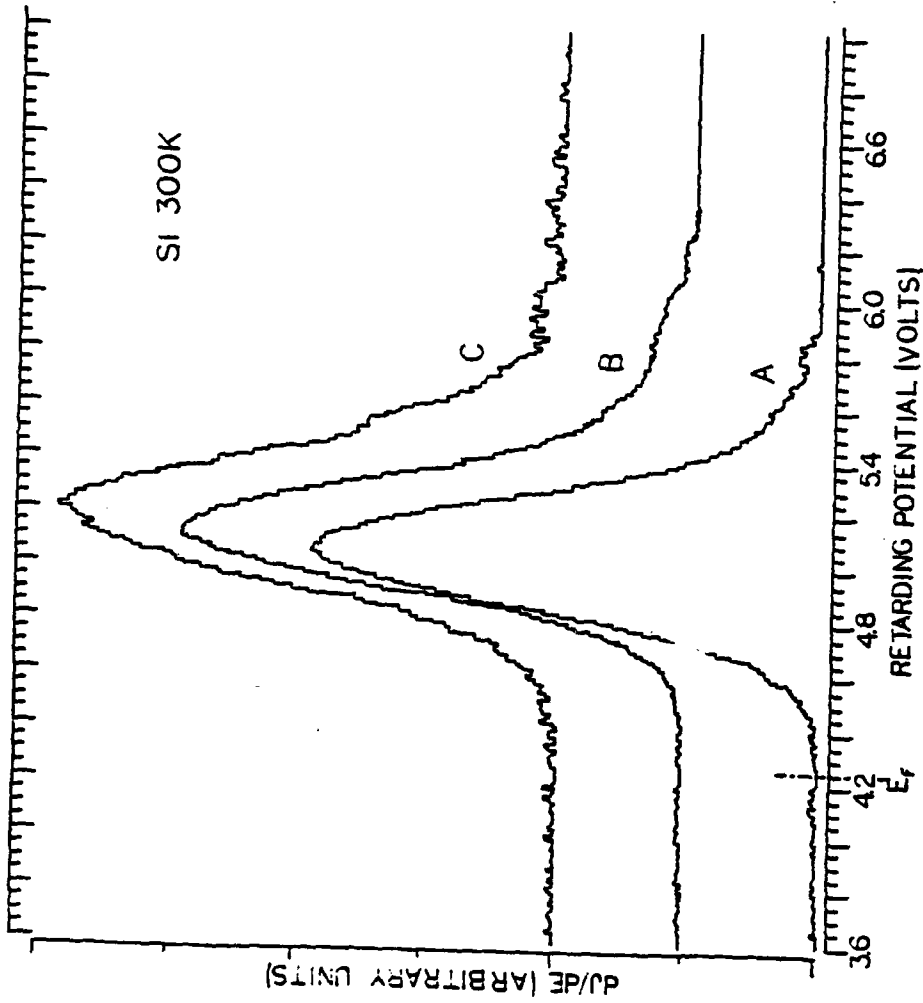


Figure 32. 300K FEED of Heavily N-Doped Si for Various Fields. (A) 4000V, (0.30 V/A); (B) 4480V, (0.34 V/A); (C) 4750V, (0.36 V/A)

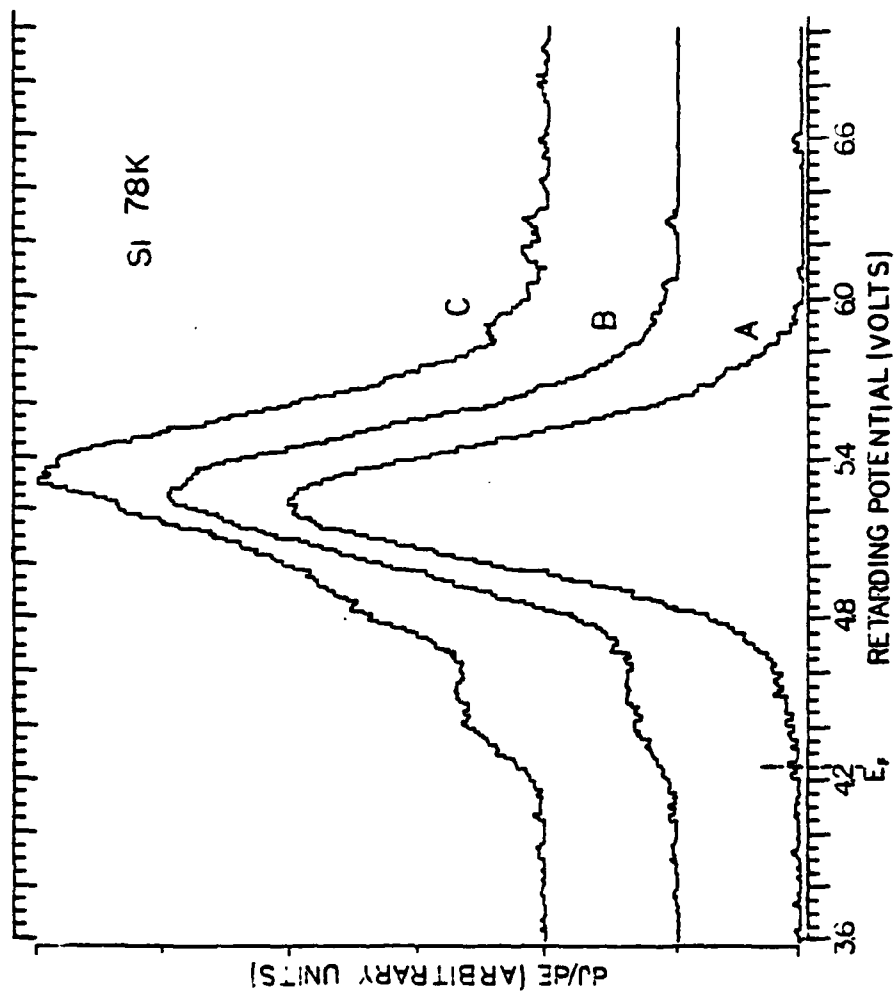


Figure 33. 78K FEED of Heavily N-Doped Si for Various Fields. (A) 4700V, (0.36 V/A); (B) 4950V, (0.38 V/A); (C) 5150V, (0.39 V/A)

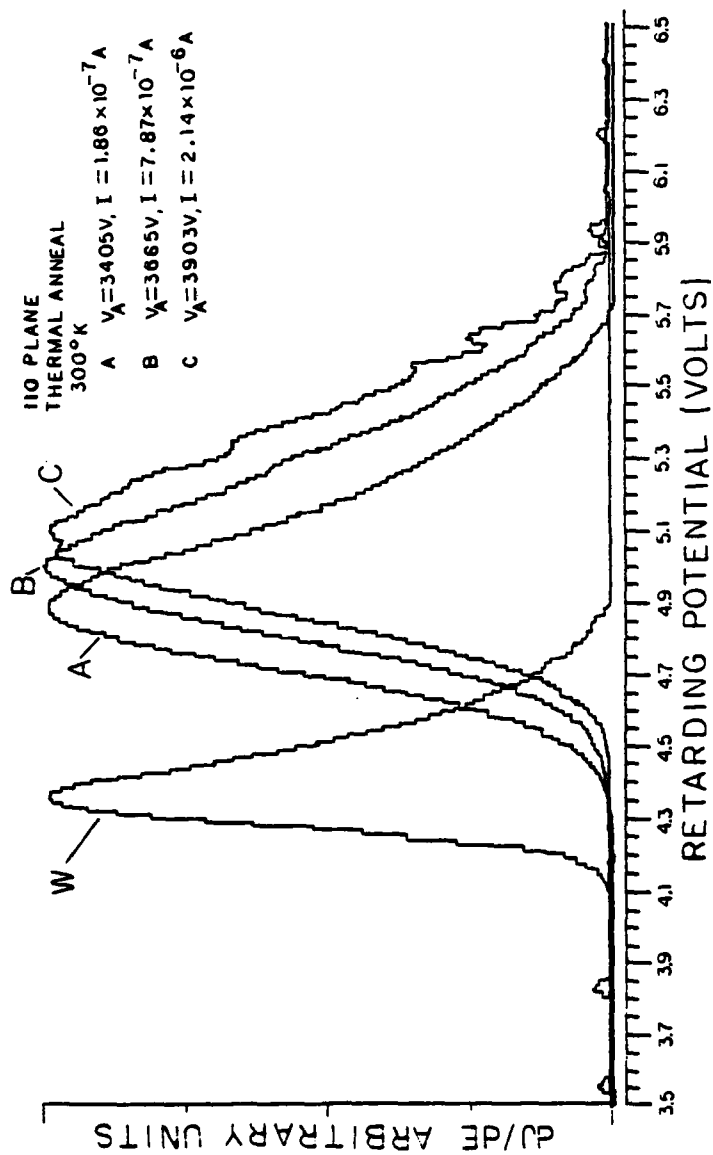


Figure 34. 300K FEED of Heavily N-Doped, Annealed Si.

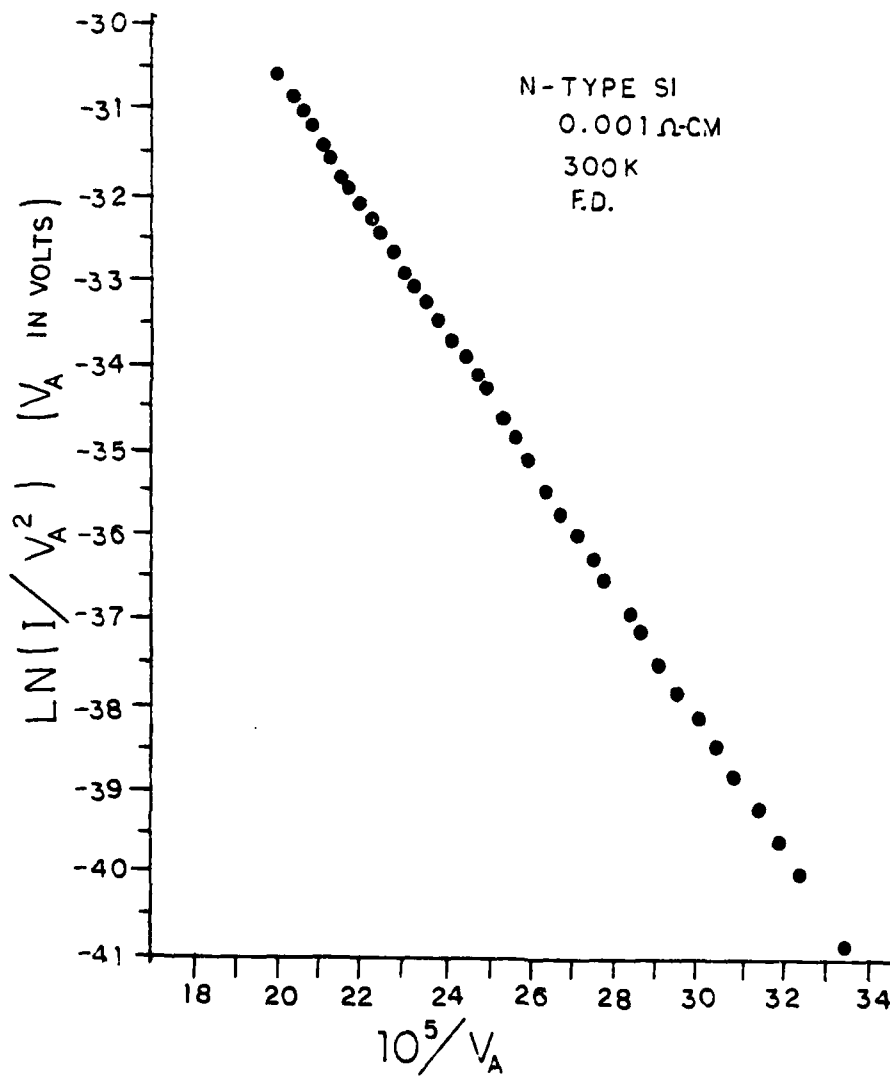


Figure 35. Fowler-Nordheim Plot for Heavily N-Doped Si.

shown in Figure 34, evidence this observation. However, the general shape of the energy distribution from the annealed surface appears slightly different from that of the desorbed surface. In particular, the annealed surface FEED shows a longer "tail" on the lower energy edge of the distribution. Such a change in the distribution shape is not predicted for valence band emission in the Stratton theory.

#### Current-Voltage Characteristics

The current-voltage behavior of the heavily n-doped Si appears to follow the F-N equation fairly well. A F-N plot of data from the field desorbed surface appears in Figure 35. No severe deviations from F-N behavior are observed, in contrast to the data obtained from high resistivity p-type material.

#### Heavily P-Doped Silicon

Only one sample of (110) oriented P<sup>+</sup> Si was studied. This sample had a resistivity of 0.015 ohm-cm, and was produced from a Monsanto-supplied wafer. The surface was field desorbed. FEEDs from this sample, which appear in Figure 36, show a single peak, located below the Fermi level, similar to the data obtained from heavily n-doped Si. Unlike the behavior of the n-type samples, however, the "onset" potential increased with increasing field as demonstrated in Figure 37. Thus, although the peak appears below  $E_F$ , it also may be

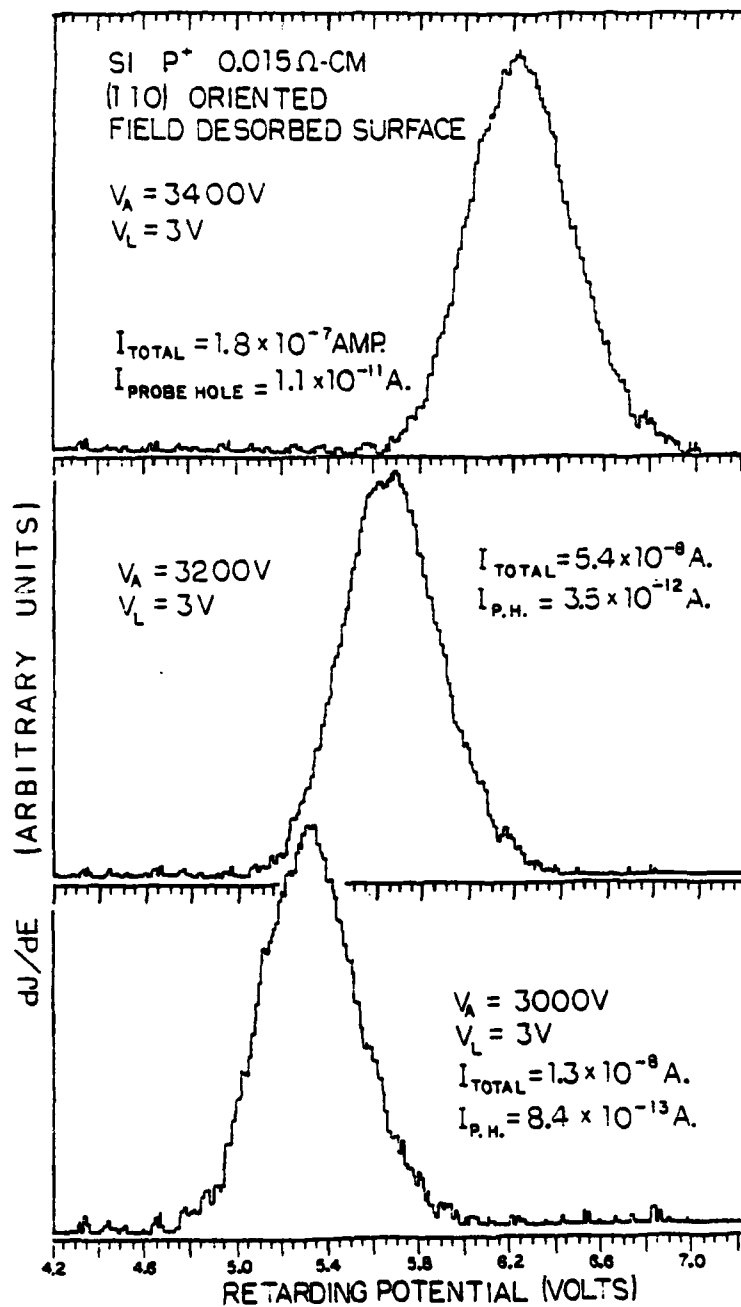


Figure 36. 300K FEEDs of Heavily P-Doped Si at Various Fields.

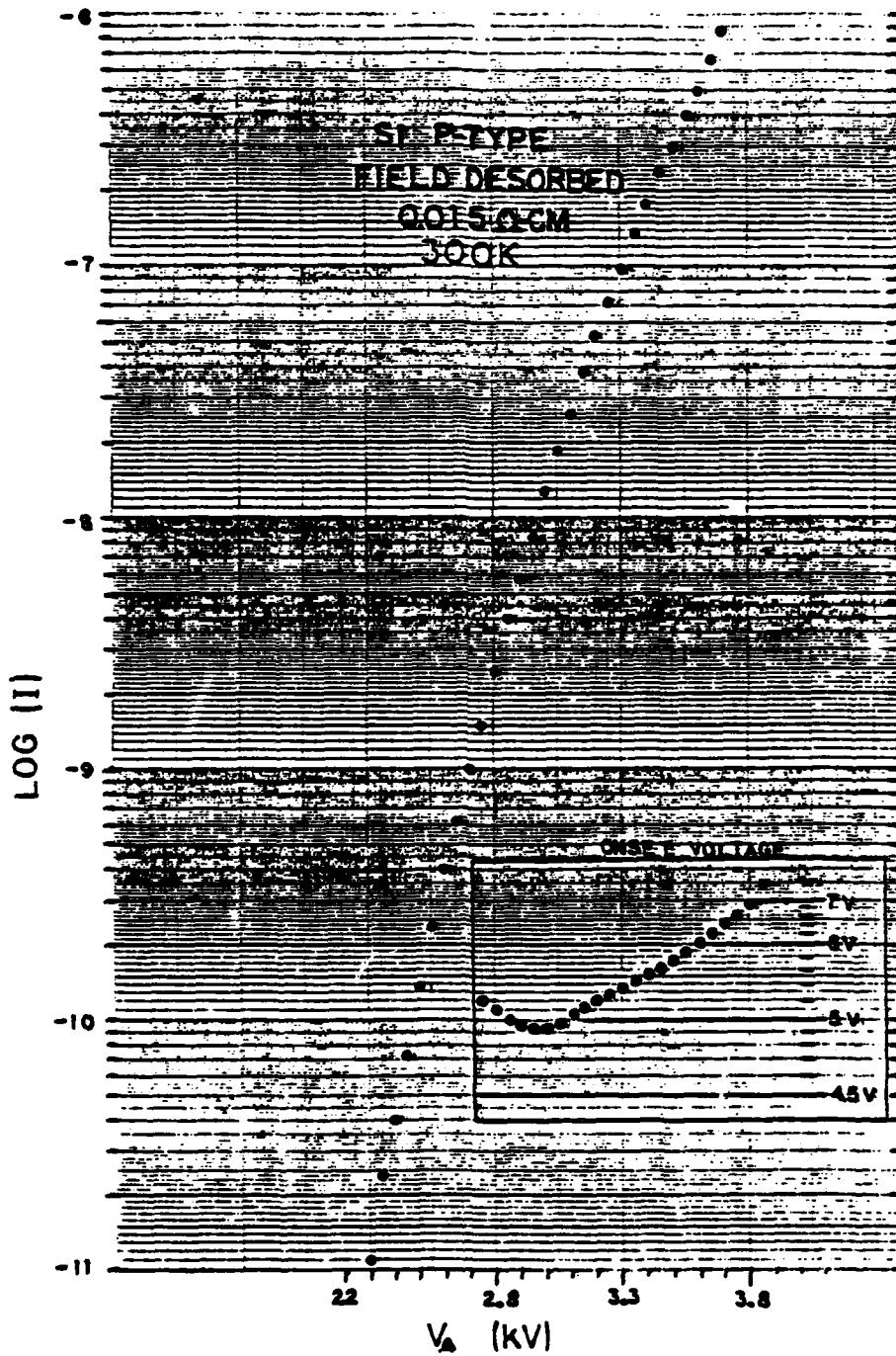


Figure 37. Onset Position and Total Current as a Function of Applied Voltage for Heavily P-Doped Si.

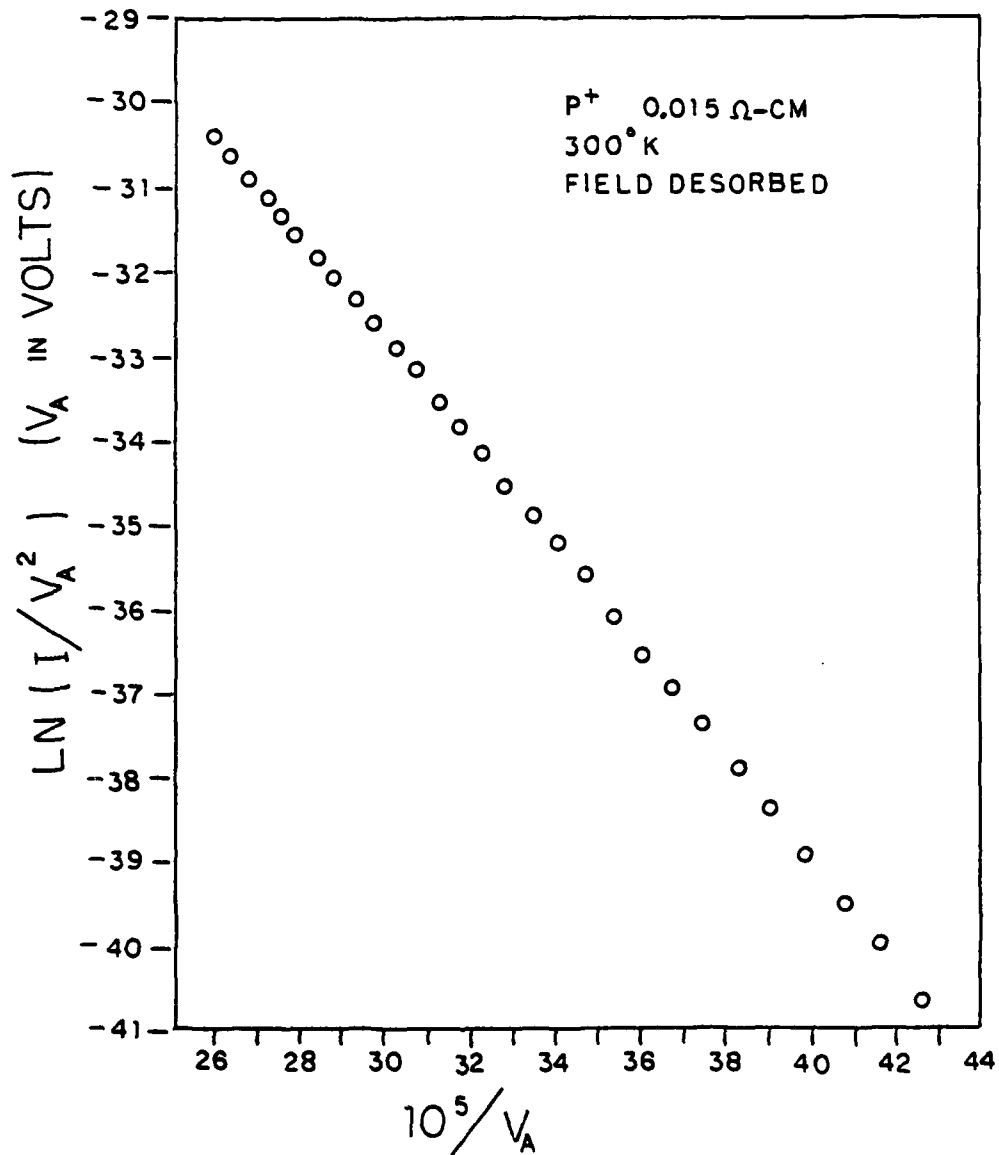


Figure 38. Fowler-Nordheim Plot for Heavily P-Doped Si.

true that a potential drop exists within the sample. The F-N plot associated with this data appears in Figure 38.

### Discussion and Comparison of Results

#### Previous Work on Si

FEED studies have been performed on Si and other semiconductors previously. For Si, Russell and Litov [45] reported a single peak which, upon "fracture," two peaks, with maxima separated by the thermal gap energy of about 1.2eV. There appeared to those authors a simple identification of the lower energy peak with the valence band, and of the upper peak with the conduction band. However, this identification was questioned by Stratton [52], who pointed out that the peak separation for bulk states emission should be greater than the gap energy, and the energy distribution should have zero amplitude for energies of the gap region. Russell and Litov argued that the poor resolution of their analyzer had spread the expected sharp peaks into the broad shapes which they observed.

Russell and Litov [45] apparently encountered some experimental problems [52]. These authors were unable to measure the offset of their sample, recording only the transient response of the lock-in amplifier on an oscilloscope. Further, they claimed to see no symmetric pattern, which generally indicates either contamination or, as described by D'Asaro [14], multiple "triplets." No information on vacuum quality is provided in their paper. The FWHM of their tungsten distribution was

reported to be 0.6eV, in contrast to the accepted width of 0.25eV at 300K.

Rather improved studies on Si were made by Kleint and Kusch [36]. They investigated 0.2 to 0.8 ohm-cm n-type Si, of (111) orientation. Using a high quality analyzer designed by Young [60], these authors described three distinct cases. First, they described seeing a single peak, showing enlargement of width and energy displacement with increasing field. Secondly, they found two peaks, with maxima separated by about 1.2eV. Thirdly, they reported two peaks separated by approximately 2.5eV. Although no basis was given, these authors attributed the peak of lowest energy to valence band emission, and that of higher energy to the conduction band, as had Russell and Litov.

#### Previous Work on Other Semiconductors

Work on GaAs was performed by Hughes and White [30]. They used heavily doped, n-type, 0.0001 ohm-cm resistivity material, and a field desorbed surface. Using a Young style analyzer, having excellent resolution, these authors found a large wide peak located almost 0.4eV below  $E_F$ , and a small subsidiary peak appearing at  $E_F$  and lower. Their data appeared similar to this author's own data on heavily n-doped Si. In addition, Hughes and White described small sharp peaks, located between  $E_F$  and the large peak, which appeared and disappeared on consecutive sweeps of their retarder. They ascribed the large peak to the valence band, and the subsidiary peaks to surface

AD-A114 896 PENNSYLVANIA STATE UNIV UNIVERSITY PARK APPLIED RESE--ETC F/G 7/4  
PHOTO FIELD EMISSION AND FIELD EMISSION ENERGY DISTRIBUTIONS FR--ETC (U)  
UNCLASSIFIED JUL 82 M H HERMAN N00024-79-C-6043  
ARL/PSU/TH-82-177 NL

2 - 2

1-5000

END  
DATE  
FILMED  
11 82  
DT \*

state emission. Those authors argued that conduction band emission was absent due to band structure effects, even though GaAs is a direct gap material and transverse momentum considerations would be of negligible importance. Further, one can show that GaAs of the quoted resistivity implies that the Fermi level is within the conduction band--the sample is degenerately n-type.

On Ge, several researchers have published results. Arthur [5] demonstrated a wide, single peak appearing below  $E_F$ . This peak occasionally showed small oscillations, especially evident at low temperature. Arthur argued that such a wide peak was consistent with a severely degenerate conduction band at the surface. Also, Arthur's results seemed independent of doping type, yielding a large single peak in all circumstances.

Further work on n-type Ge was performed by Shepherd and Peria [47]. Attached to a smaller, wide peak, these researchers found a very strong, sharp peak, of width 0.1 eV. The sharp peak was angularly localized at a particular bright feature of the annealed Ge pattern. For other emission directions, the amplitude of the subsidiary peak varied. The strong sharp peak was ascribed to a surface state, as it does not fit the theory for the Ge (100) direction emission, and it was sensitive to surface contamination. The broader, low amplitude peak was argued by these authors to be valence band emission, as it appeared below  $E_F$  and had the expected shape of valence band emission.

Lastly, Kisker, Mahan, and Reihl studied the FEED of a 370Å thick semiconducting EuS film deposited upon a W emitter [34]. Their published data shows a large, wide peak, located nearly 3eV below

$E_F$ , with a smaller, subsidiary peak beginning at  $E_F$  and tailing lower in energy. These authors note that the large peak shifts toward lower energy and broadens with increasing field, though the subsidiary peak grows in relative amplitude and remains close to  $E_F$ .

Thus, their data corresponds in general shape to that of other researchers. Kisker, et al. argued that inelastic scattering of electrons entering the EuS layer could account for the observed distribution. Those electrons which arrive at the surface unscattered by traps are emitted with energy equal to the Fermi level. Inelastic scattering reduces the energy of many electrons, however, and they drop down to the conduction band edge or to trap levels within the conduction band. Therefore, a large electron population exists at and near the conduction band edge, giving the large peak. As the applied field is increased, they argue, the large peak shifts downward with the conduction band, while the small peak remains near the Fermi level.

### Generalization and Discussion

Comparing all of the accumulated data of these researchers, one sees a general trend. Consistently, a single large peak dominates the energy distributions. This single peak shifts down in energy with increasing field, and a subsidiary peak arises just below  $E_F$ . With increasing field, this subsidiary peak increases in amplitude compared to the lower energy peak. The subsidiary invariably appears with nearly pure, high resistivity semiconductors, or with heavily doped semiconductors operated at low (78K) temperature. This implies that free carrier density is strongly related to the FEED characteristics.

Although the explanation put forth by Kisker, et al. [34] is sensible and attractive for their thin film data, it is not applicable to the other samples. For example, their model supposes a perfectly dielectric semiconductor, with the Fermi level bending down parallel to the assumed bending of the valence and conduction bands. We expect band bending of the order of  $\rho Jx$ . We may take the maximum value of  $J$  to be 1000 Amps/cm<sup>2</sup>, so that for resistivities  $\rho$  of order .001 ohm-cm, one volt would develop for an emitter of length one centimeter. This is an unreasonably large estimate for typical emitters, implying that this mechanism is unrealistic. For this reason, we must discard the model of Mahan, et al. as too limited to explain the diverse results accumulated on many samples of high conductivity semiconductor.

Alternatively, let us consider another model, based upon photoemission work. To explain their photoemission data, Wagner and Spicer [55] proposed that the Si surface was covered by a large density of surface acceptor states. For their cleaved  $n^+$ , 0.001 ohm-cm  $\epsilon$ i sample, they concluded that the density of surface states was of order  $8 \times 10^{14}/\text{cm}^2$  --approximately one surface state per surface atom. Moreover, they concluded that Figure 39 is an acceptable distribution in energy of these surface acceptor states. From that figure, we find the surface states overlapping the valence band, and tapering off to zero density below the conduction band edge.

This picture of the surface state density leads to band bending without an externally applied field. Wagner and Spicer calculated that the band bending, for the planar surface, would give a 0.2 eV difference from the flat-band condition at a distance of 12 Å from the surface. This bending could alternatively arise from an imaginary external field of  $-0.51 \text{ V}/\text{Å}$  [28]. Also, there is no net external field, due to the surface states, because the band bending causes a buildup of positive charge both in the valence band and on ionized donor states near the conduction band.

The application of an external field will flatten the bands. Assuming that the surface states are filled, the electrostatic fields will add vectorially. In this case the imaginary internal surface field of  $0.51 \text{ V}/\text{Å}$  will add to the emission field  $F/K$ , with  $K$  the dielectric constant. The band curvature will be  $V(x) = V_0(F) \exp(-x/L_D)$ . Here,  $L_D = [ \epsilon kT/q^2 N_D ]^{1/2} = 13 \text{ Å}$ . The field just within the surface will be  $dV(x)/dx = V_0(F)/L_D$ . Thus,  $V_0(F) = (L_D \times [ 0.51 \text{ V}/\text{Å} - F ] / K)$  is the

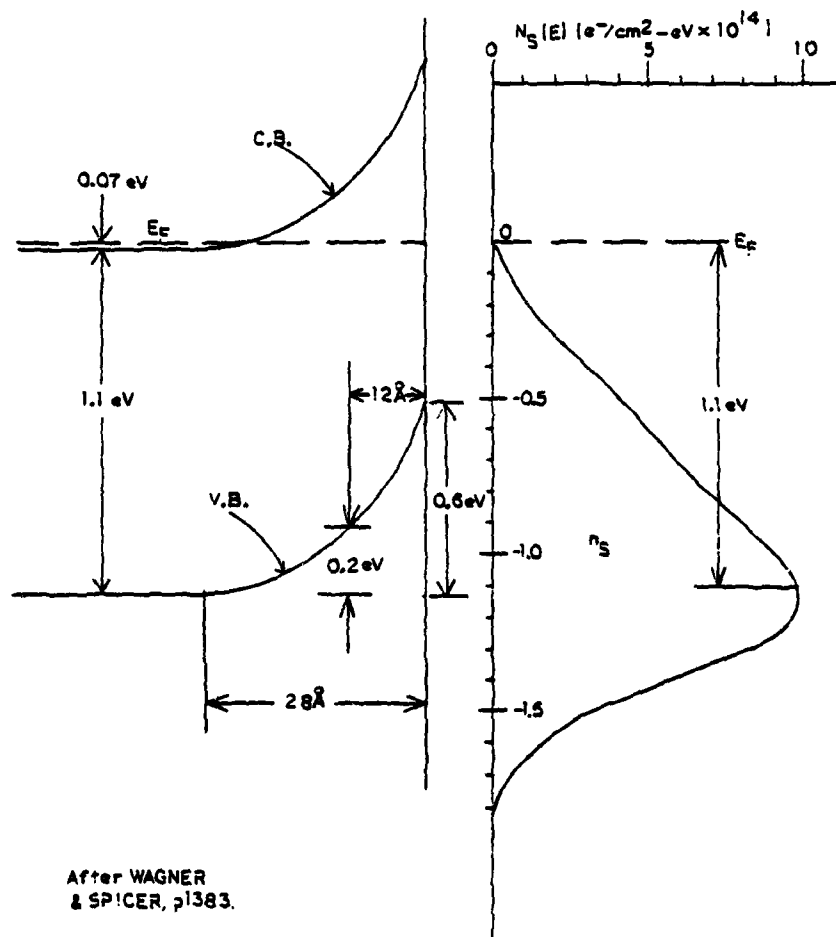


Figure 39. Proposed Model of Surface-State Density from Photoemission Experiments.

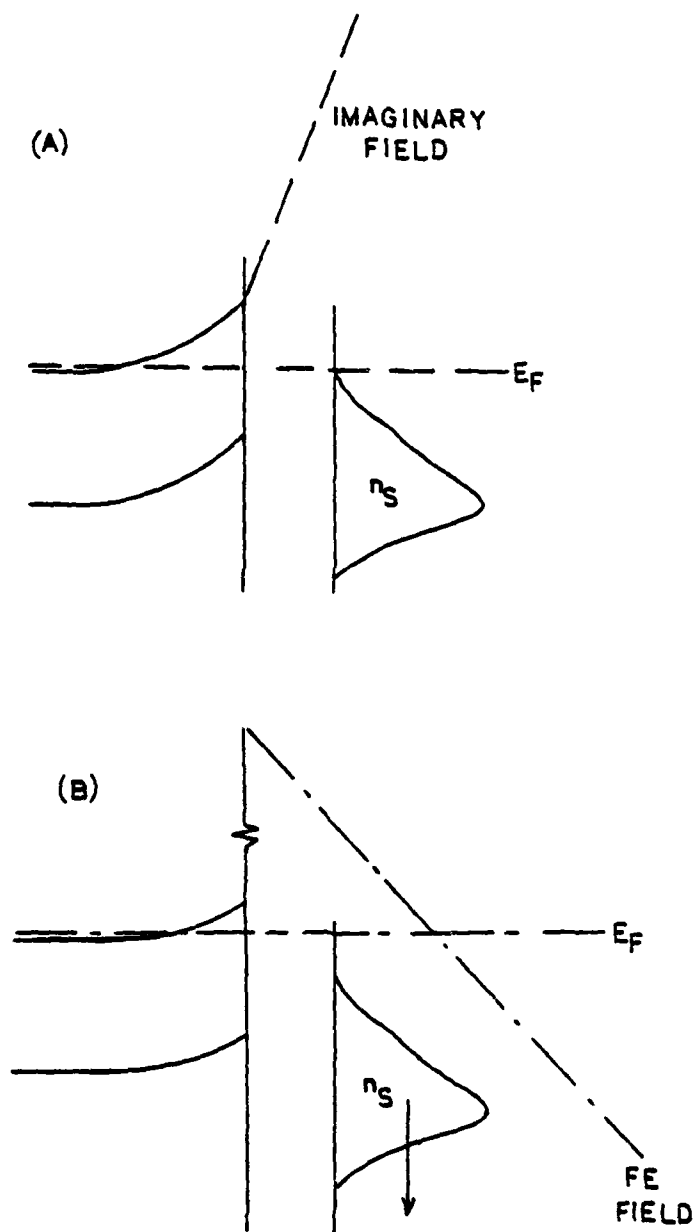


Figure 40. Extension of Proposed Surface-State Model to Field Emission from N-Type Si.

extent of the internal band bending. As shown in Figure 40(b), the external field of order  $0.3V/\text{\AA}$  shifts the entire surface state density below  $E_F$ , with the high energy tail remaining some few tenths of an eV below  $E_F$ .

This analysis of Wagner and Spicer's photoemission data suggests an alternative mechanism of semiconductor field emission. It suggests that emission occurs primarily from surface states, rather than the two bands, at low fields. This proposition adequately explains why the large, major peak occurs below  $E_F$  and why it shifts downward in energy with increasing field. It explains why the shift is not attributable to an IR drop in the sample.

Further, the invocation of surface state emission may explain the discrepancy in shapes of the FEEDs. The theoretically predicted width of conduction band emission is very narrow--narrower than the metallic distributions observed for W. The experimentally observed distributions are always much wider than the metallic distributions. Also the theoretical valence band distribution does not change width with increasing field; it only changes amplitude. This is in contrast to the experimental observation that the width increases with increasing field. In addition, the wide shape of the experimental distribution may be a consequence of the increasing density of surface states with lower energy--similar to the case for valence band emission, which also gives a wide distribution. Also, a change in the surface state density, effected by annealing or desorbing the surface, would yield a change in the FEED. This is observed in the experimental distributions.

In certain circumstances, emission will also come from the

conduction band. This will occur if the charge on the surface states is insufficient to prevent the externally applied field from bending the bands downward at the surface. Such will be the case if emission of electrons from the surface states causes their population to diminish sufficiently. Wagner and Spicer's data implies that the bands will never bend downward for typical emission fields of up to  $5 \times 10^7$  V/cm, in the absence of emission. Indeed, for heavily n-doped semiconductors, we do not generally see emission at energies near  $E_F$ . However, for lightly doped semiconductors, or heavily doped semiconductors at low temperatures, we do see emission at these higher energies. Thus, the concentration of electrons in the surface states must diminish under these emission conditions, to about 0.8 of the original surface electron density.

This simple model employing the conduction band and a band of surface acceptor states, seems to explain a majority of the experimental work. The experimental reports of two broad peaks can be ascribed to these two sources. This model easily covers the observation of only one peak, that of the lower energy surface states, as well as that of the double peaks. It also handles the observed fact that the energy separation between peaks increases with field, and that the higher energy peak increases in amplitude with increasing field.

## CHAPTER V

## PHOTO-FIELD EMISSION

Introduction

The effect known as Photo-Field Emission (PFE) or alternatively as Photo-assisted Field Emission, was found in Si by Busch and Fischer in 1963 [11]. It had been discovered much earlier by Apker and Taft [4] that CdS emitters demonstrated a large increase in FE current, which was attributed to purely to photoconductivity [4]. The characteristic non-linear F-N curves, along with the spectral response of Si and Ge, implied to many researchers that the effect was also totally attributable to photoconductivity. Indeed, typical data taken from a field desorbed Si sample, which has been plotted in Figure 29, shows that the effect cuts off at approximately the band gap energy.

The photoconductivity argument supposes that the F-N relation holds true at the surface. The F-N equation then relates the total current to the true surface potential,  $V_s$ .  $V_s$  is related to the applied voltage  $V_A$  by

$$V_s = V_A - IR \quad (64a)$$

$$R = R(T, l, I_n, \dots) \quad (64b)$$

Thus the F-N equation becomes

$$I = aF^2 \exp(-0.685 \phi^{3/2}/F) \quad (65)$$

$$F = \beta(V_A - IR) = \beta V_s \quad (66)$$

Solution of the transcendental equations (65) and (66), for assumed typical values of the constants  $a$ ,  $\beta$ ,  $R$  yields the graphed curves shown in Figure 41. Notice that the shape of these curves closely resembles the experimentally observed graphs, shown in Figure 26, when the results are plotted as  $\text{Log}(I)$  vs.  $1/V_A$ .

However, the results do not appear as attractive when plotted in F-N form as  $\text{Log}(I/V_A^2)$  vs.  $1/V_A$ , as in Figure 42. Although the data appears to fit theory for one regime, namely low  $V$ , it does not fit the high  $V$  case. Further, it is observed that p-type Si shows a stronger PFE effect than n-type Si of the same resistivity. If photoconductivity were the only rationale for this effect, the doping type would be inconsequential. In addition, researchers found that the F-N equation is not obeyed at the surface. Using a retarding potential analyzer, the surface potential can be found, and F-N plots of the resulting data show non-linearities. Lastly, the PFE current always exceeds the dark current, even with identical surface potentials. My data on this latter effect is shown in Table 2.

For these reasons, the photoconductivity explanation was rejected for a more rigorous model by Yatsenko [56]. Yatsenko attempted to model PFE as an extension of the planar MOS structure in the "quasi-dielectric" limit. This planar structure admittedly neglected geometrical effects of the actual spherical surface, but was felt to involve the same physical properties as the PFE problem. The model presented the sample in terms of a base region, a depletion region, a

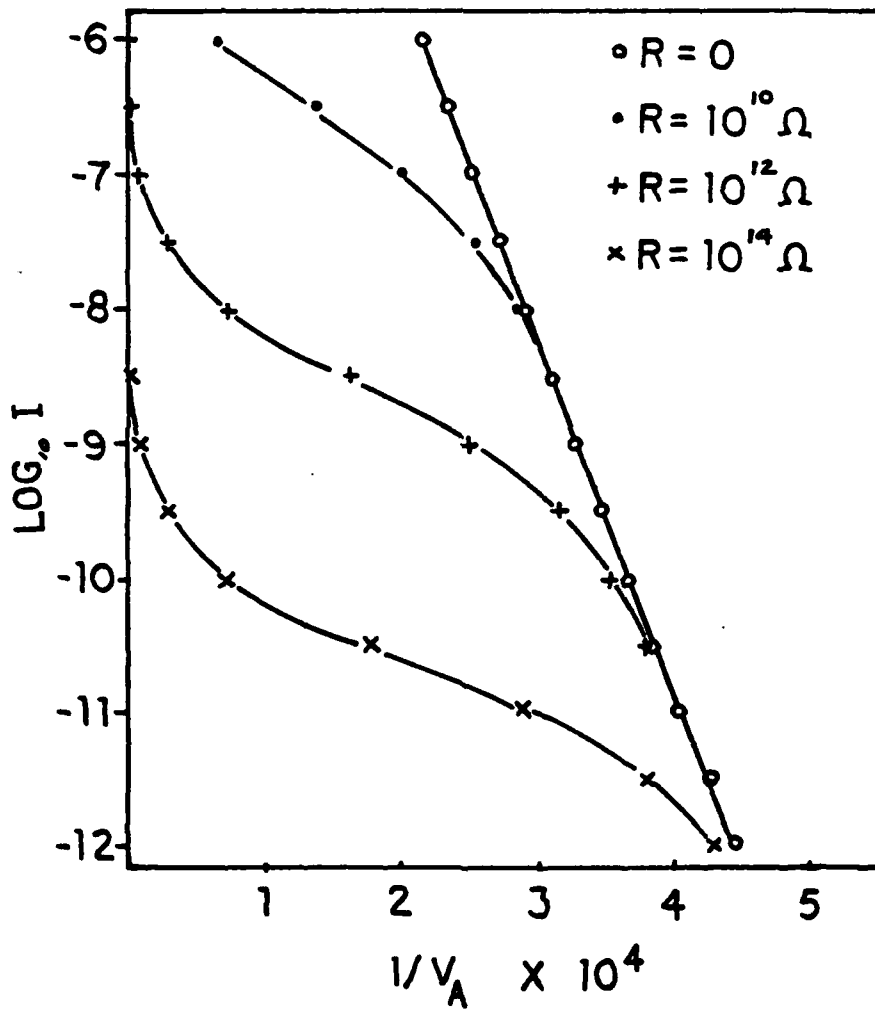


Figure 41. Log of Total Current as a Function of Inverse of Applied Voltage for Photoconductivity Correction to F-N Theory.

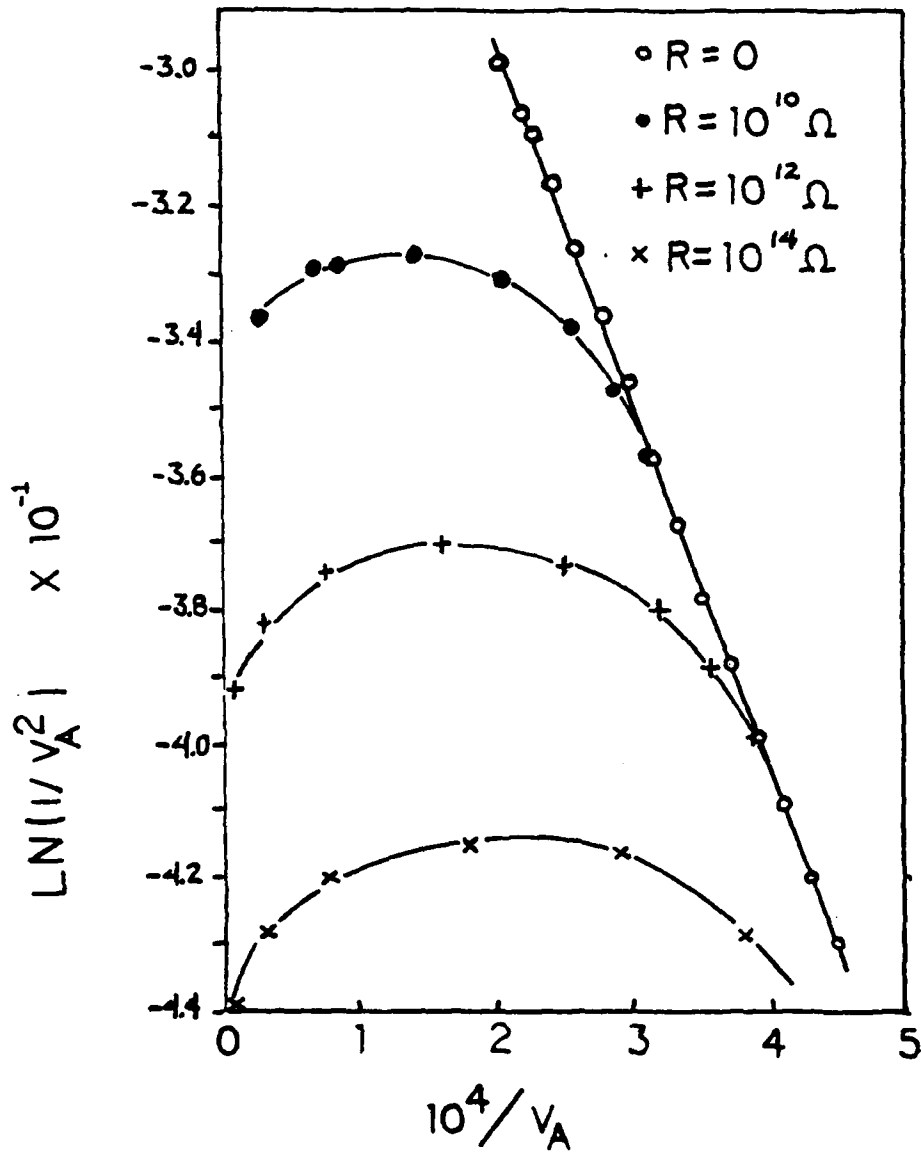


Figure 42. Fowler-Nordheim Plot of Photoconductivity Correction to F-N Theory.

surface inversion layer, and a surface barrier regime. After analyzing the MOS structure, Yatsenko concluded that under all typical FE conditions, the internal surface field would be higher than the avalanche breakdown field in Si, typically  $10^5$  V/cm. This paradox led Yatsenko to conclude that surface states must therefore be screening the sample from the emission field, for under avalanche breakdown conditions, he reasoned that the current would increase unreasonably-- behavior not experimentally observed.

The conjecture of surface states screening the sample is reasonable. As demonstrated by my data, presented in the section on FEED of Si, the energy lowering of the main peak with increasing field conforms with this interpretation. Further, the width of the distribution, even for heavily doped Si, may indicate that an increasing density of surface states with lower energy, as discussed in that section. In addition, Stetsenko, Yatsenko, and Miroshnichenko [50] found that a single applied voltage pulse broke into two current segments of discernably different time constants; presumably the two were due to emission from bulk states and from surface states. Lastly, the two peak amplitudes showed hysteresis, interpreted to be further evidence of the surface states having a larger time constant than bulk states.

In spite of the reasonable argument that surface states are screening the bulk from the external field, Yatsenko overlooks several important points. First, the observation of PFE coincides with a shift in the dark surface potential. Second, the large sample resistance limits the current, even if avalanche breakdown occurs in the surface

region. Both these points suggest that the sample resistance must be taken into account more explicitly than in Yatsenko's treatment. Further, FEED data on low temperature Si, and the hysteresis data of Stetsenko, et al., indicate that the surface states deplete to some extent during PFE emission.

This last point indicates that Yatsenko was correct in his initial assumptions about the mechanisms of PFE, namely that PFE occurs at the point where the surface states become depleted. However, his theory showed that avalanche breakdown must occur at the surface region if the surface states deplete substantially. Yatsenko reasoned that such a breakdown must necessarily be catastrophic, as current is a continuous quantity throughout the sample. Plagued by the conclusion of avalanche breakdown, he was unable to forfeit the role of surface states in the model. In other words, if the surface states alone control the emission characteristics, then one must be left with the pure photo-conductivity argument. However, if both surface states and the bands contribute to emission, then additional current terms come into play.

#### A Second Model

Rather than revise Yatsenko's model, I propose the following, second model. This model simplifies the PFE by considering emission from two energy regimes. In reality, three energy regimes are possible-- the surface states, and two bulk bands. However, as no knowledge is

presumed of the actual form of the surface state wavefunctions, I will take the valence band as a "reasonable" substitute for the surface state emission. Further, I will assume that the conduction electrons may possess a zero minimum transverse energy, i.e. a free electron, spherical energy surface for the conduction band.

#### Account of Photoconductivity

To take account of photoconductivity, we will again assume that the surface potential  $V_s$  and the field  $F$  are directly proportional.

Thus,

$$F = \beta(V_A - IR_\lambda) = \beta V_s \quad (67)$$

and

$$\beta \cong 1 / (5 r_t) \quad (68)$$

In determining  $R$ , we use

$$R_\lambda = R(\rho_\lambda, \text{sample dimensions}) \quad (69)$$

$$\rho_\lambda^{-1} = \sigma_\lambda = \sigma_0 + \Delta\sigma \quad (70)$$

$$\sigma_\lambda = (n\mu_n + p\mu_p) + (\Delta n\mu_n + \Delta p\mu_p) \quad (71)$$

now  $\Delta n = \Delta p = A'(\text{Intensity } I_n, \lambda, \text{Reflection coeff., } \alpha(\lambda) \dots)$  (72)

$$n \cdot p = n_i^2 = 1.4 \times 10^{20} / \text{cm}^6 \times (T/300K)^3 \quad (73)$$

For p-type Si,  $p = N_A$ ,  $n = n_i^2 / N_A$ . At 78K,  $n = 3.44 \times 10^{18} / N_A$ .

For lightly doped Si, say  $10^{14} / \text{cm}^3$ , this gives  $n = 3.44 \times 10^4 / \text{cm}^3$ . So

$$\frac{\rho_{\lambda}}{\rho_{\text{dark}}} = \frac{\sigma_{\text{dark}}}{\sigma_{\lambda}} = \frac{n e \mu_n + p e \mu_p}{(n + A') e \mu_n + (p + A') e \mu_p} \quad (74a)$$

$$= N_A e \mu_p / [A' e \mu_n + (N_A + A') e \mu_p] \quad (74b)$$

with

$$\rho_{\text{dark}} = 1/\sigma_{\text{dark}} = 1/[N_A e \mu_p] \quad (75)$$

To determine  $A'$  ( $I_n, \lambda, R, \dots$ ), we assume that each generated carrier has a lifetime  $\tau$ . The reflection coefficient,  $R$ , is taken to be 0.3. Complete absorption is assumed--in reality absorption is related to the sample thickness and the absorption coefficient at the wavelength of the incident radiation. With these approximations,

$$A' = (\#e^-/\text{cm}^3) = (\#e^- \text{ generated}/\text{cm}^2\text{-sec}) \times (2\pi \bar{r} L_0 / \pi r^2 L_0) \times (1 - R) \times \tau \quad (76)$$

$$A' = [I_n \lambda 5.03 \times 10^{14} / \text{cm}^2\text{-sec}] \times [2/\bar{r}] \times 0.7 \tau \quad (77)$$

with  $\lambda$  in Å,  $I_n$  = intensity in Watts/cm<sup>2</sup>. The variable  $\bar{r}$  is an average radius of the sample =  $(r_b + r_t)/2$ , in cm. In this approximation, effects of surface absorption, bulk absorption, etc. are ignored. We aim here only to arrive at a functional approximation to the absorption.

#### Note on the Lifetime

The recombination of carriers follows the law

$$dn/dt = -Cn \cdot p \quad (78)$$

with  $C$  a proportionality constant. If  $p = N_A$ , the solution is

$$n = n_0 \exp(-CN_A t) = n_0 \exp(-t/\tau) \quad (79)$$

so  $\tau = \tau_n = 1/CN_A$ . This means that the reduction in carrier lifetime eliminates or substantially reduces the PFE effect for heavily p-doped samples.

#### Sample Resistance

We determine  $R_{\text{dark}}$  from the classical expression  $R = \rho L/A$  applied to a cone shaped sample of length  $L_0$  and having a base and tip of radii  $r_b$  and  $r_t$  respectively. The angle of the cone is  $\nu = (r_b - r_t)/L_0$ . Applying the resistance formula yields

$$R_1 = \rho_{\lambda} \int_0^{L_0} dL / [A(L)] = (\rho_{\lambda} / \pi) \int_0^{L_0} dL / [(r_b - \nu L)^2] \quad (80a)$$

$$= (\rho_{\lambda} / \pi \nu) \times (1/r_t - 1/r_b)$$

$$= \rho_{\lambda} L_0 / \pi r_t r_b$$

or

$$= \rho_{\lambda} / \pi \nu r_t \quad (r_b \gg r_t) \quad (80b)$$

The contribution of the hemispherical cap on the resistance is negligible, as the path length involved is only of order  $r_t \ll L_0$ .

#### Photogeneration of Carriers

The photogeneration of free carriers does more, qualitatively, than just change the sample resistivity. Free electrons are accelerated toward the surface by the internal field. These photogenerated electrons have higher total energy than those in surface states or the valence band. Thus, these conduction electrons may be emitted

preferentially, possessing substantially higher tunnelling probability. If not emitted, these electrons may become trapped at the surface, cascading into the lower energy surface states.

We proceed along these lines as follows.

Let

$$J_{\text{total}} = J_{\text{dark}}(\lambda) + J_{\text{light}}(\lambda) \quad (81)$$

where  $J_{\text{dark}}(\lambda)$  is the valence band current, calculated with  $R_1$  used.  $J_{\text{light}}(\lambda)$  is the contribution from the electrons generated by light. We approximate the dark current by the valence band contribution, neglecting surface state emission, taking

$$J_{\text{dark}}(\lambda) = J_v(F) \quad (82)$$

$$\text{and } I = J_{\text{total}} \times \text{Area of tip.} \quad (83)$$

In turn,  $J_v(F)$  is evaluated using the Stratton model and free electron mass for the holes. This calculation may be approximated by

$$J_v(F) = 8\pi m e f(E) \frac{3\hbar e F^2}{[9\hbar^3 (2m)^{1/2} 4 (X + E_g)]} \times \exp[-4(2m)^{1/2} (X + E_g)^{3/2} / 3\hbar e F] \quad (84a)$$

$$\text{or, } J_v(F) = [7.6 \times 10^9 \text{ Amps/cm}^2] \times F^2 \times (1/(X + E_g)) \times \exp[-0.685(X + E_g)^{3/2}/F] \quad (84b)$$

with  $X$ ,  $E_g$ , in eV, and  $F$  in V/Å.

To evaluate  $J_{\text{light}}(\lambda)$ , we assume that all electrons are at the bottom of the conduction band. Therefore, we may express

$$\begin{aligned} I_{\text{light}} &= \text{Area of tip} \times J_{\text{light}}(\lambda) \\ &= [1-R] \times [\text{\#photons generated/cm}^2\text{-sec}] \times \\ &\quad [\text{Active area}] \times \\ &\quad [\text{Probability of emission}] \times \\ &\quad [1.6 \times 10^{-19} \text{ coul/photon absorbed}] \end{aligned} \quad (85)$$

The components of (85) are evaluated below.

(1) R = reflection coefficient. Assuming normal incidence of unpolarized light,  $R = [((n_2 - n_1)^2 + k^2)/((n_2 + n_1)^2 + k^2)]$ . The extinction coefficient,  $k$ , is negligibly small for photons of energy below 1.2eV. Here,  $n_1 = 1$  for vacuum,  $n_2 = \sqrt{\epsilon} = 3.435$  for Si. So  $(1-R) \approx 4n_1n_2/(n_1 + n_2)^2 = 0.7$ .

(2) #Photons generated/cm<sup>2</sup>-sec. This is the intensity  $I_n$  divided by the energy per photon, or

$$\begin{aligned} [\text{\#photons/cm}^2\text{-sec}] &= I_n \lambda (\text{\AA})/hc \\ &= [5.03 \times 10^{14} \lambda (\text{\AA}) I_n (\text{Watts/cm}^2)]/(\text{cm}^2\text{-sec}) \end{aligned}$$

(3) Active area. This is the area of the sample in which generated electrons reach the surface. If we assume a recombination lifetime,  $\tau$ , for the excess electrons, then

$$n(t) = n_0 \exp(-t/\tau)$$

is the number left at time  $t$  after generation at time  $t=0$ . Assuming a drift velocity  $v_d = \mu E$ , we get  $x = v_d t$  and

$$n(x) = n_0 \exp(-x/v_d \tau).$$

The number arriving at the surface  $x=0$  from a distance  $x$  away will be  $N_s = \int_0^{\infty} n(x) W(x) dx$ . Here,  $W(x)$  is the width of the conical shaped tip of angle defined just before Equation 80. Thus,  $W(x) = (2r_t + 2\nu x)$ .

Integration yields

$$N = 2n_0 v_d \tau (r_t + \nu v_d \tau).$$

Therefore, the effective area is  $N_s/n_0$ , or  $[\text{Active area}] = 2v_d \tau (r_t + \nu v_d \tau)$  or  $(r_b \times L_0)/2$ , whichever is less.

(4) Probability of emission. We will take this to be the WKB solution at the conduction band energy, neglecting the image potential and band

structure effects, and assuming the free electron solution. Thus,

$$[\text{Probability of emission}] = D(E_c) = \exp(-0.685X^{3/2}/F).$$

(5) [Surface emission area]. We take this to be  $2\pi r_t^2$ , neglecting obvious structure characteristics, such as faceting, which reduces the emitting area of the surface. The field desorbed surface appears to have uniform emission, and is more closely represented by this expression.

Therefore, substituting the above into equation (85) yields:

$$J_{\text{light}}(\lambda) = [I_n \lambda (1.35 \times 10^{-4}) v_d \tau] \times \\ [r_t + \gamma v_d \tau] \text{Amps/cm}^2 \times \\ (\exp[-0.685X^{3/2}/F]) / [2\pi r_t^2] \quad (86)$$

$$\text{or} \quad = [I_n \lambda (1.35 \times 10^{-4}) / 4] \times [r_b \times L_o] \times \\ \exp[-0.685X^{3/2}/F] / [2\pi r_t^2]$$

To this point, we have a formulation of PFE embodied in equations (67) through (86). Graphs of data appear in Figure 43, with the approximations taken below:

$I_n = I_n \times 1 \text{Watt/cm}^2$	$E_g = 1.1 \text{eV}$
$N_A = 10^{14} / \text{cm}^3$	$\lambda = 10^4 \text{\AA}$
$v_d = 10^6 \text{cm/sec}$	$X = 4 \text{eV}$
$\tau = 10^{-4} \text{sec} \times (10^{14} / N_A)$	$L_o = 5 \text{mm} = 0.5 \text{cm}$
$r_t = 3000 \text{\AA} = 3 \times 10^{-5} \text{cm}$	$\mu_p = 500 \text{cm}^2 / \text{V-sec}$
$r_b = 5 \times 10^{-3} \text{cm}$	$\mu_n = 1500 \text{cm}^2 / \text{V-sec}$
$\gamma = (r_b - r_t) / L_o = 10^{-2} \text{radians}$	

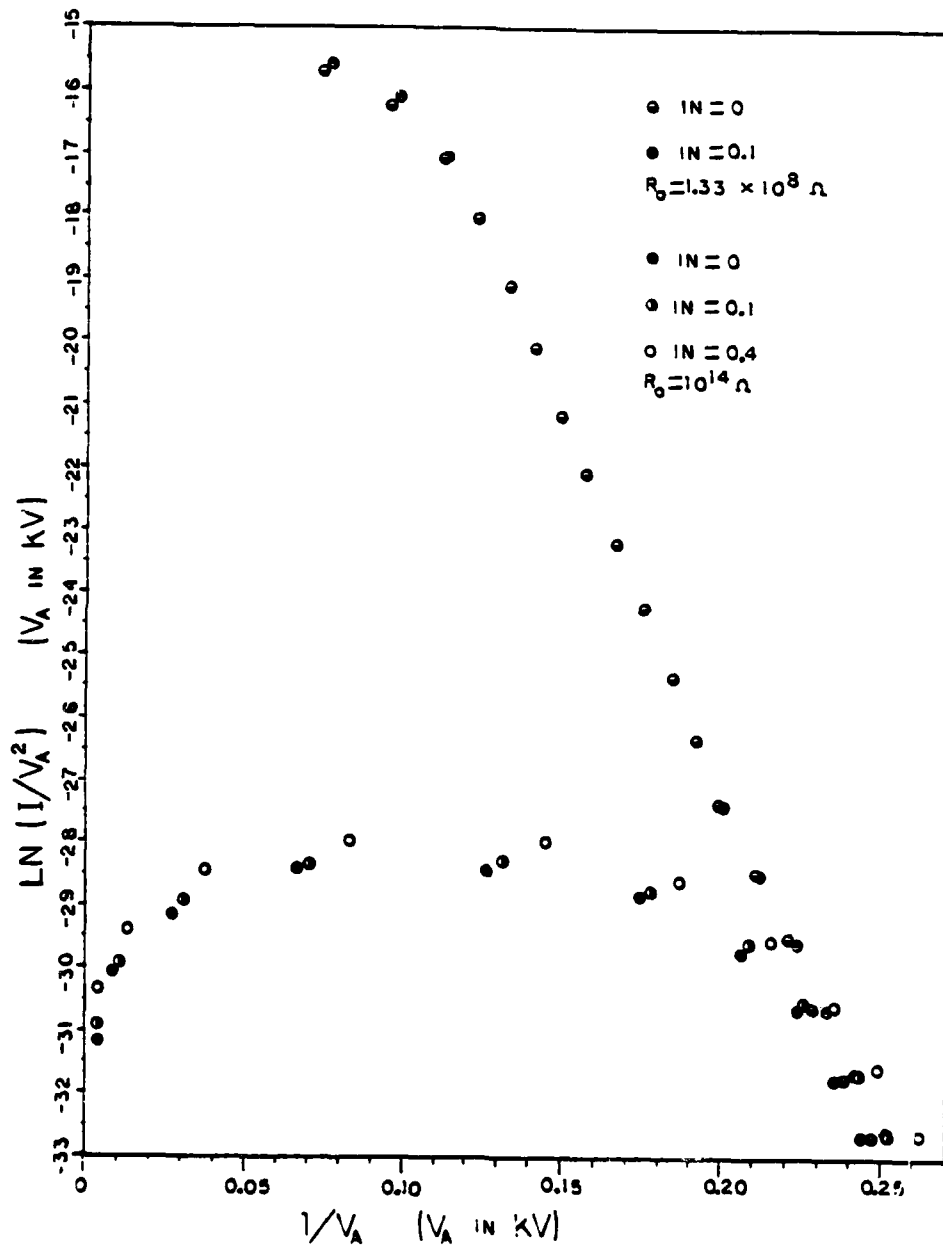


Figure 43. Fowler-Nordheim Plot of Revised Theory Without Breakdown.

With these values, the set of equations reduce to the five below:

$$\begin{aligned}
 F(V/\text{\AA}) &= (V_A \times 10^3 - I \times R_\lambda) / (1.5 \times 10^4 \text{\AA}) \\
 J_{\text{light}} (\text{A/cm}^2) &= (1.245 \times 10^5) \times I_n \times \exp[-5.48/F] \\
 J_{\text{dark}} (\text{A/cm}^2) &= (1.49 \times 10^9 \times F^2) \times \exp[-7.89/F] \\
 I(\text{A}) &= (J_{\text{light}} + J_{\text{dark}}) \times (5.65 \times 10^{-9}) \\
 R_\lambda (\text{ohms}) &= (1.33 \times 10^8) \times [1 + 1.13 \times I_n]^{-1} \quad (87)
 \end{aligned}$$

We observe from Figure 43 that, while this formulation of the model does give a PFE current with light incident that exceeds the dark current at the same surface potential, it does not yield the up-turn behavior at high  $V$  near the origin of the abscissa. For this reason, we must postulate that a breakdown mechanism exists at high cross-sample voltages.

Two types of breakdown mechanism seem possible. The first, avalanche breakdown, may occur when the internal field within the Si reaches the breakdown field. For Si, this breakdown field is a function of doping, and is of order  $10^5 \text{V/cm}$  for a background doping of  $10^{14}/\text{cm}^3$ . Avalanche breakdown will multiply the expected current at a particular cross-sample voltage by some factor  $M$ . This implies that the cross-sample resistance  $R_\lambda$  should be multiplied by the factor  $1/M$ . However, the avalanche breakdown mechanism reduces the resistance only in the region of the sample which is actually supporting the breakdown field--the rest of the sample must retain the same resistivity.

Therefore, we may envision that the surface region of the sample will breakdown earliest, and that a breakdown region will grow in length back toward the sample base.

The second mechanism is punch-through. Punch-through is typically a bipolar transistor breakdown mechanism, in which the base region is covered by the depletion regions of the emitter and collector. In our case, the depletion region extends from the surface back toward the base of the sample, as described above.

Slight differences exist in the application of these two mechanisms. In the second, the depletion region is assumed to have zero resistance. In avalanche, however, the resistivity is merely reduced to  $1/M$  of its original value. The avalanche mechanism will be utilized in the breakdown mechanism in this model.

#### Dielectric Model

The simplest model of the sample is that of a pure dielectric. Thus we will get a contribution to the dark current from the avalanche throughout the sample.

To compute the avalanche current, we assume that the non-avalanched current is multiplied by some factor  $M$ . As this occurs at some fixed cross-sample voltage  $V$ , the original sample resistance  $R$  must be reduced to a value  $R/M$ . Further, some of the avalanche generated electrons go into the conduction band where they may be emitted.

To evaluate the number entering the conduction band, we note that the conductivity increases by the same factor  $M$ , so

$$\sigma M = \sigma + (M-1)\sigma = \sigma + (\text{excess } \sigma)$$

$$= \sigma + \hat{n}e\mu_n + \hat{p}e\mu_p$$

with  $\hat{n}$  and  $\hat{p}$  representing excess carriers generated by the avalanche process. We assume that  $\mu_n = 3\mu_p$ , and that the number of excess holes generated equals the number of electrons generated. Thus,

$$(M-1)\sigma = 4pe\mu$$

$$\text{or } \hat{n} = \hat{p} = (M-1)\sigma/4e\mu_p$$

$$\text{Using } \sigma = [N_A + A']e\mu_p + [A' + n_i/N_A]e\mu_n$$

Combining terms,

$$\sigma = [N_A + 3n_i^2/N_A + 4A']e\mu_p$$

$$\text{Thus } \hat{n} = (M-1)/4 \times [N_A + 3n_i^2/N_A + 4A']$$

The number of these  $\hat{n}$  electrons which arrive at the surface per unit time per unit area,  $N$ , must be evaluated. Using a Maxwellian distribution of velocities leads to:

$$N = \int_{v_x > 0} v_x f_{MB}(\vec{v}) d^3v$$

$$\text{With } A = m/2kT,$$

$$f_{MB}(\vec{v}) = \hat{n}[A/\pi]^{3/2} \times \exp(-A \cdot v^2)$$

$$\text{Thus, } N = \hat{n}[A/\pi] \times \int_0^{\infty} v_x \exp(-Av_x^2) dv_x \times$$

$$\int_{-\infty}^{\infty} \exp(-Av_y^2) dv_y \times \int_{-\infty}^{\infty} \exp(-Av_z^2) dv_z$$

$$\text{so } N = \hat{n}[A/\pi]^{3/2} [1/2A][\pi/A]$$

$$\text{yielding } N = \hat{n}[kT/2\pi m]^{1/2}$$

We also require an expression for  $M$  itself. Bar-Lev gives an empirical expression for diode breakdown as [7]:

$$M = 1 / [1 - (E/E_{AB})^{2m}]$$

The variable  $m$  is empirically determined, and is usually between 3 and 6. To a first approximation, we may take the internal field to be the total IR drop across the sample divided by the total length of about 5mm. Then, taking  $E_{AB}$  for Si of light doping to be  $2 \times 10^5$  V/cm, and  $m=3$ , we get:

$$M = 1 / [1 - (IR / (0.5 \text{ cm} \times 2 \times 10^5 \text{ V/cm}))^6]$$

or 
$$M = 1 / [1 - (IR/10^5)^6]$$

The effect of choosing a multiplier function which is less "hard," such as  $M = [1 - IR/10^5]^{-6}$  will also be demonstrated. The model employing the latter equation will be termed "soft" breakdown.

Thus, the additional current density expected from the avalanche-generated conduction band electrons will be

$$J_{CB} = n \times [kT/2\pi m]^{1/2} \times [1.6 \times 10^{-19} \text{ coul/chg.}] \times [\text{probability of emission}].$$

#### Full Model with Breakdown

The full model, with breakdown now included, is embodied in the following set of equations. Here, the previous parameter assumptions have been inserted.

$$(1) \quad J_{\text{dark}} = 1.49 \times 10^9 \times F^2 \times \exp(-7.89/F)$$

$$(2) \quad J_{\text{light}} = ([1.245 \times 10^5 \times I_n \times M'] + [4.32 \times 10^{-13} \dot{n}]) \times \exp(-5.48/F)$$

- (3)  $\hat{n} = [(M-1)/4] \times [10^{14} + 4A']$
- (4)  $A' = [2.82 \times 10^{13} \times I_n]$
- (5)  $F = [V_A \times 10^3 - I_{total} \times R_1] / 5r_t$
- (6)  $R_1 = [R_0/M] / [1 + 1.13 \times I_n]$
- (7)  $(J_{dark} + J_{light}) \times 5.65 \times 10^{-9} / I_{total} - 1 = 0$
- (8a)  $M = M_1 = [1 - (2 \times I_{total} \times R_1 / (2 \times 10^5))^6]^{-1}$  "hard"
- (8b)  $M = M_2 = [1 - (2 \times I_{total} \times R_1 / (2 \times 10^5))]^{-6}$  "soft"
- (9)  $M' = [\hat{n} + A'] / A'$
- (10)  $r_t = 3000\text{\AA}$

The model is most easily solved in the following order. First, one chooses values for the intensity,  $I_n$ , dark resistance  $R_0$ , and arbitrary total current value  $I_{total}$ . Secondly, equations (6) together with either (8a) or (8b) are solved iteratively, yielding  $R_1$ . Using  $R_1$ ,  $M$  is obtained from (8a) or (8b) appropriately. Lastly, the remaining equations are solved iteratively, using equation (7) as the test.

Results of this model appear in Figures 44 and 45.  $R_0$  has been taken to be  $10^{14}$  ohms in both cases. Figure 44 shows the result of using  $M_1$ , the "hard" breakdown expression. In contrast, Figure 45 shows the "soft" breakdown case, utilizing  $M_2$ . The hard breakdown qualitatively follows the experimental data, showing  $\ln(I/V_A^2)$  with a local minimum. Alternatively, the "soft" breakdown gives the smooth transition between high and low current regimes, apparent in the experimental data, compared to the sharp slope of the "hard" case at low  $(1/V_A)$  values. Some combination of the two approaches used, or a better empirical expression for  $M$  would no doubt yield better qualitative agreement to the empirical data.

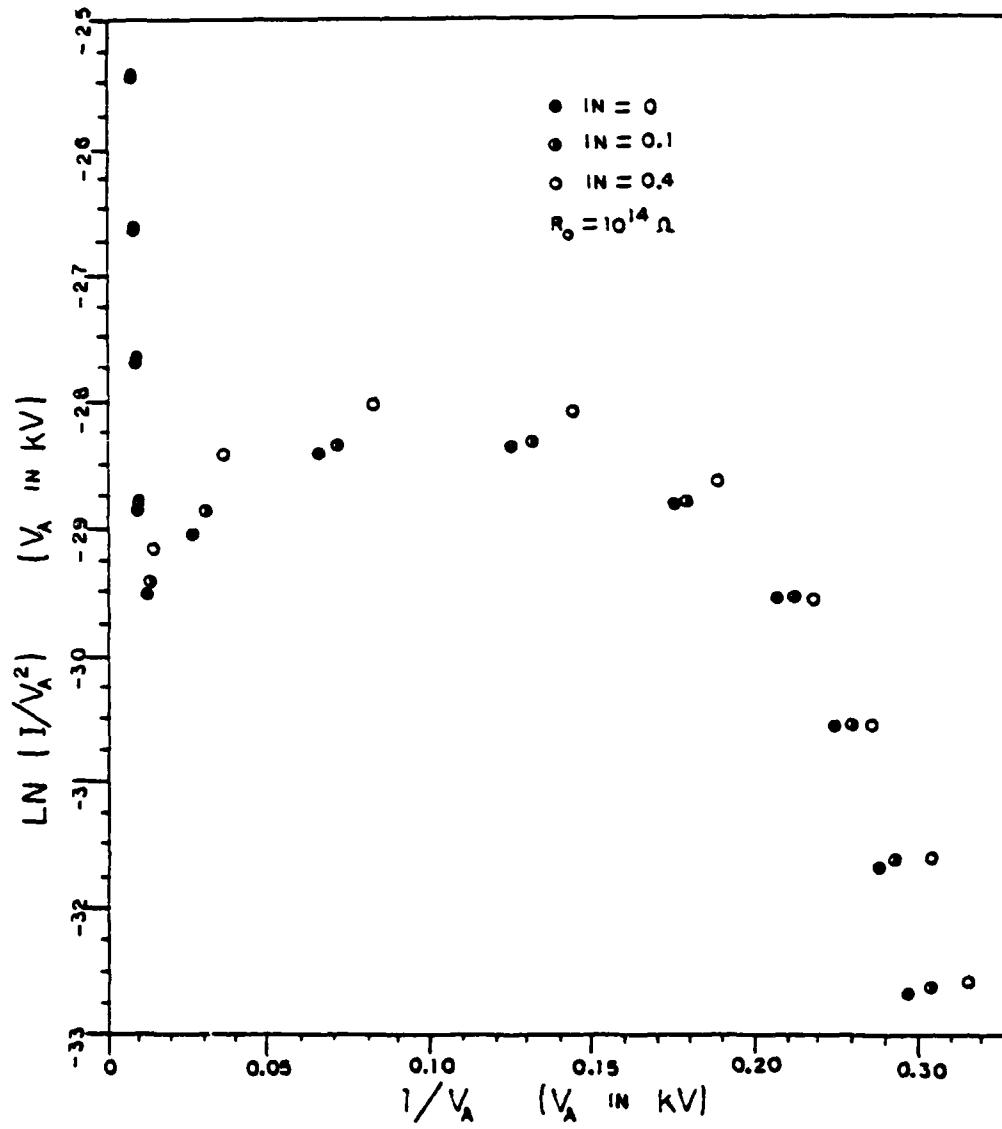


Figure 44. Fowler-Nordheim Plot of Revised Theory with Hard Breakdown Mechanism.

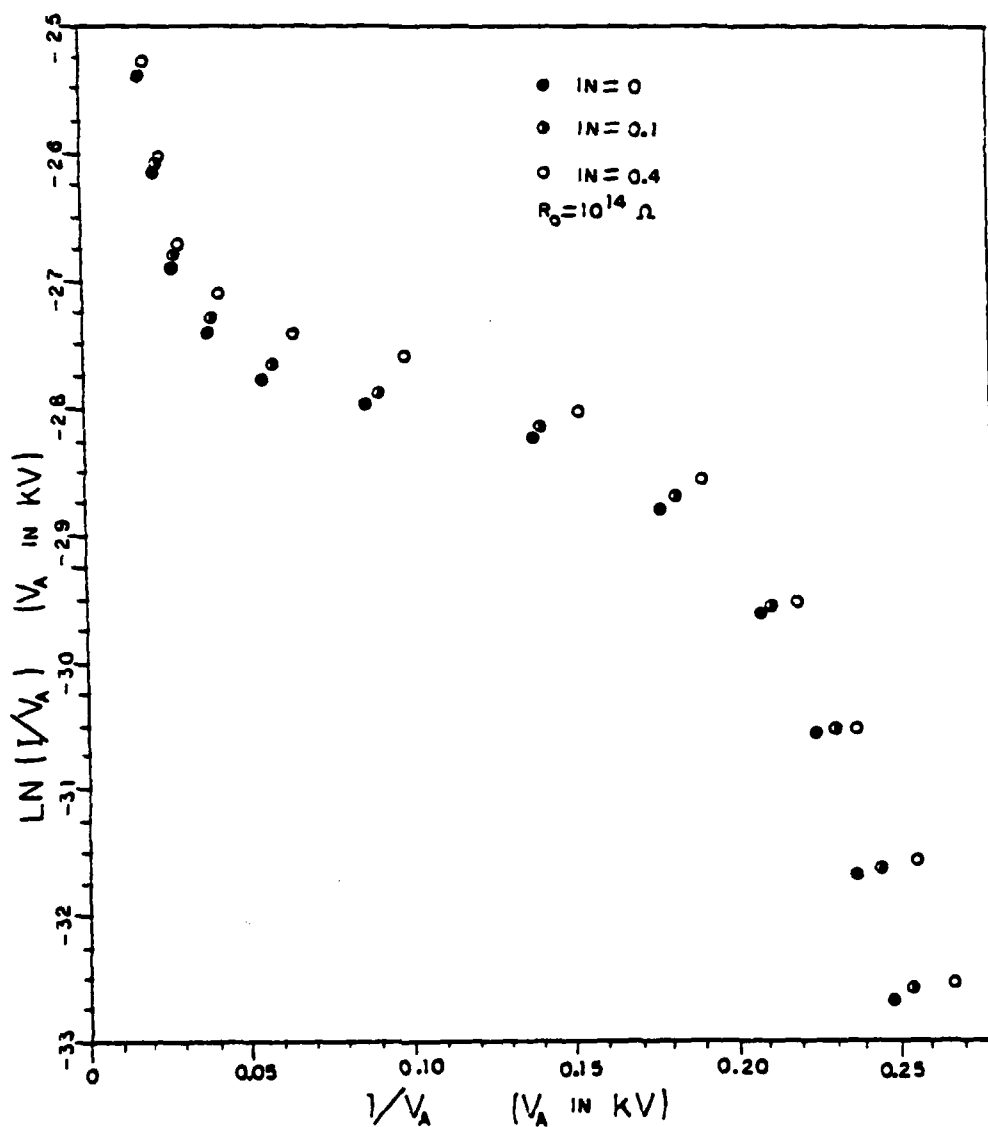


Figure 45. Fowler-Nordheim Plot of Revised Theory with Soft Breakdown Mechanism.

Lastly, it should be noted that the graphs derived from these models show discrepancy in the low current regime. Experimentally, the FEED studies show emission generally originates from one wide energy regime, ascribed to surface states. For high current densities, a subsidiary peak at higher energy appears, but it is of lower intensity than that of the surface state emission. In these models, the author has neglected treatment of the surface barrier, present with negatively charged surface acceptor states. For low current densities, it is envisioned that this barrier will substantially reduce the conduction band contribution to the current, and eliminate the discrepancy present in these models.

Taking this into account, theoretical plots using the same model but with  $J_{\text{light}}$  reduced by a factor of 5000, are shown in Figures 46 and 47. These figures indicate that the discrepancy at low current levels is eliminated by neglecting the conduction band contribution.

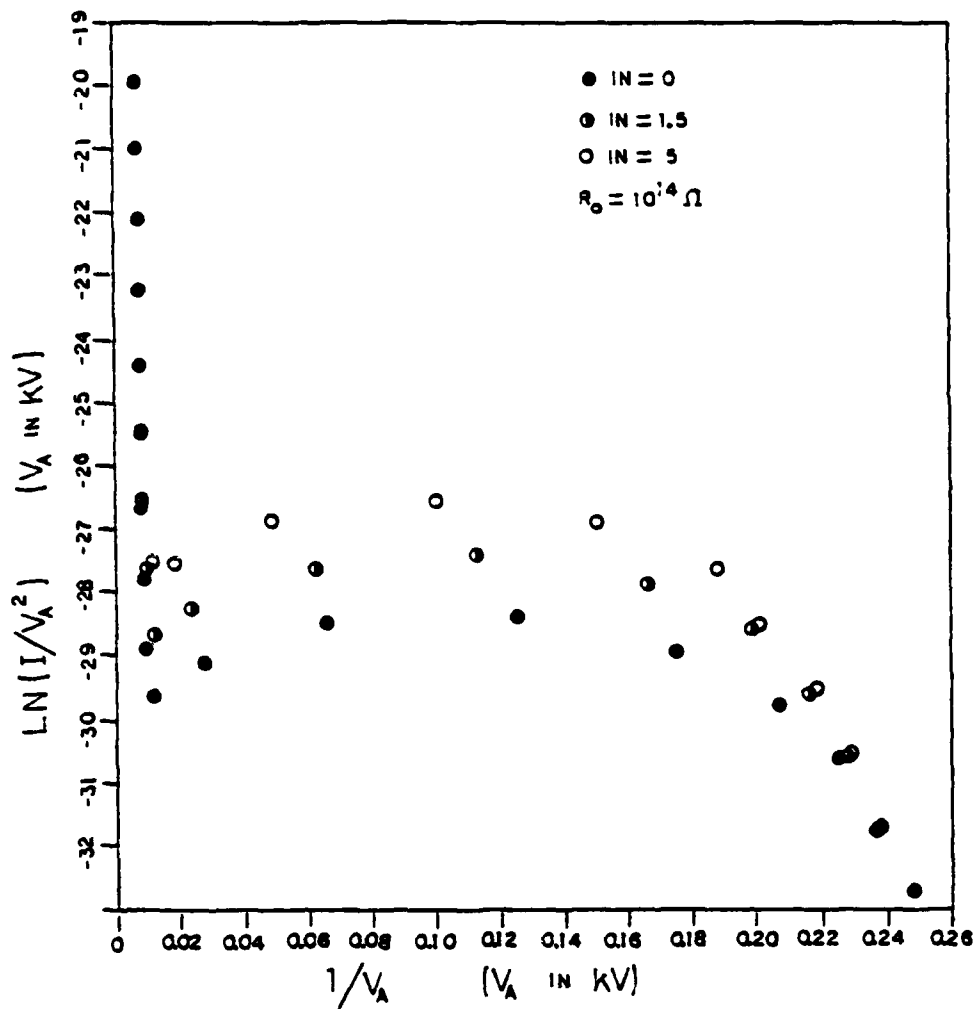


Figure 46. Fowler-Nordheim Plot of Revised Theory with Hard Breakdown Mechanism Without Conduction Band Contribution.

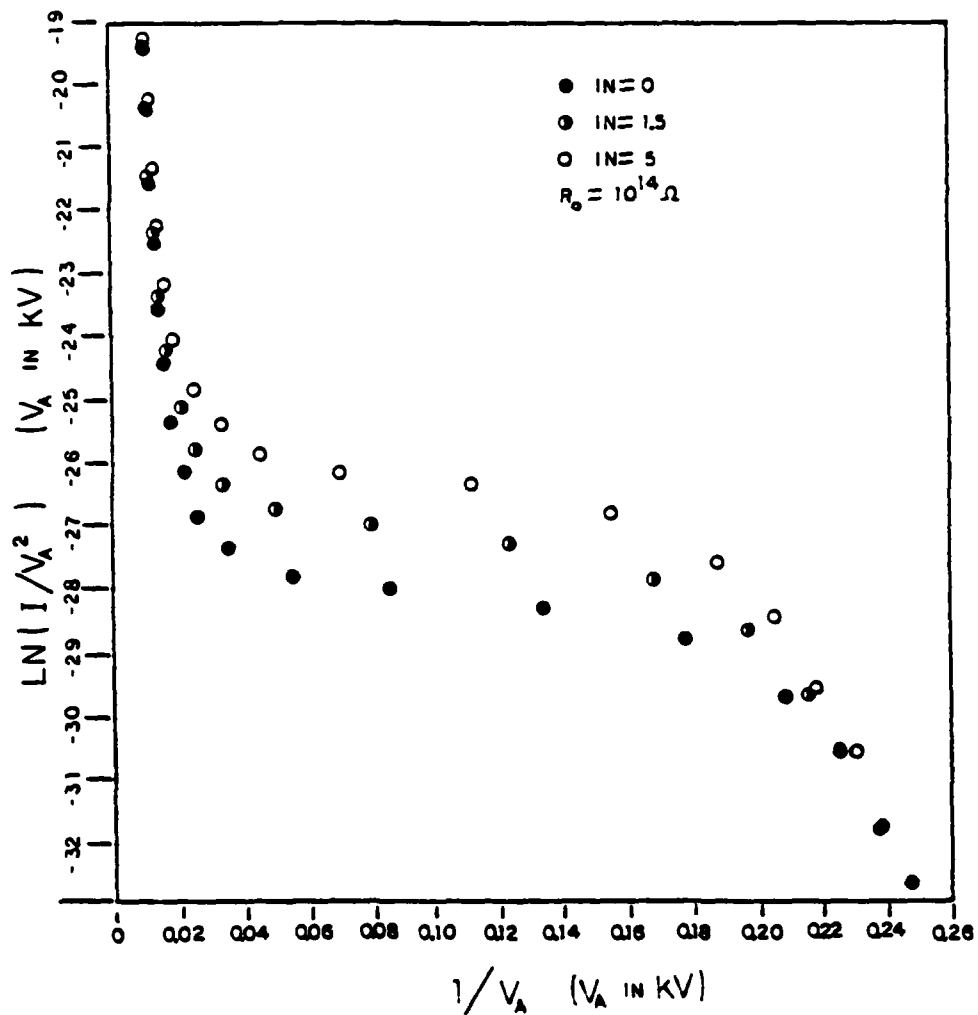


Figure 47. Fowler-Nordheim Plot of Revised Theory with Soft Breakdown Mechanism Without Conduction Band Contribution.

## CHAPTER VI

## CONCLUSION

In summary, the thesis has examined the results of both past and current experimental results with respect to the present theory of FE from semiconductors. In general, application of the Stratton theory predicts either one or two peaks in the FEED, corresponding to the valence and conduction bands. The separation of these two peaks at the base is taken to be a constant, the thermal gap energy, if surface states are neglected. Further, as the Fermi level is shifted, the valence band peak theoretically should not change shape--only amplitude. Experimentally, both the peak separation and lower energy peak shape widen with increasing field. The single emission peak, seen for degenerately n-doped semiconductors at 300K, always appears some tenths of an eV below the Fermi level, even at very low current densities. A smaller, subsidiary peak appears at 78K for these heavily n-doped samples at high fields. The subsidiary peak also appears in data of other researchers for lightly doped semiconductors, and those at low temperature.

Comparison with photoemission results leads to a different

model of FE from semiconductors. The data of Wagner and Spicer [55] on photoemission from heavily n-doped Si shows a wide band of surface states contiguous to the valence band and tailing off to zero a few tenths of an eV below the conduction band edge. Combining this interpretation with the application of an electron emission field leads to the conclusion that surface state emission, rather than valence band emission, is responsible for the large peak observed below the Fermi level on heavily n-doped semiconductors. This conclusion, implying surface state emission, explains the energy position of the lower peak and, qualitatively, its width. The upper, subsidiary, peak is tentatively ascribed to emission of conduction band electrons.

Such a conclusion from FEED studies and photoemission also concurs with work on PFE. For example, Stetsenko, Yatsenko, and Miroschnichenko [50] observed two separate time constants from single voltage pulses applied to emitters. In addition, they found hysteresis in the emission characteristics of pulse pairs; the second of the two pulses always showed reduced emission. To these authors, their results indicated that emission occurs primarily from surface states, which deplete under strong emission.

Surface states may also play a role in explaining anomalies in FE work function determinations. Although this point was not investigated in the thesis, Busch and Fischer [11] determined that work function values seemed to correlate to the Fermi level in the bulk. That is, an n-type emitter, having a high bulk Fermi level, also demonstrated a large work function. This thesis presents data indicating that field desorbed and annealed surfaces show different work

function values. Perry [42,43] found that Si emitters gave two or more distinct work function values for the same emitter. Generally, the change in work function came at high current densities. His data shows that the value of work function may increase or decrease upon changing into the high current regime. Also, Allen [1,2] observed that a hysteresis existed for some of his thermally annealed Si emitters. The surface state density may thus be changing in these various circumstances.

In application to a theory of PFE, Yatsenko [56] was the first to take account of surface states. His theory initially assumed that such states depleted, allowing field penetration into the semiconductor surface. However, he abandoned this notion after showing that the penetrating field was greater than that necessary for avalanche breakdown. In Yatsenko's model, avalanche necessarily leads to an infinite current. The experimental FEED work indicates that some field penetration does exist for low temperatures and dopings--precisely the case for PFE. Thus, a new model, eliminating or reducing the breakdown problem, was needed to link the FEED evidence to the PFE results.

Such a model is suggested in this thesis. In this model, the photon flux generates carriers with two functions. The carriers reduce the sample resistance, and electrons generated increase the conduction band population. Although breakdown is seen to be necessary to give the correct shape to the PFE F-N plots, the breakdown does not yield infinite current. This latter is because the sample resistance never drops to zero. Thus, the surface field is limited by the potential drop within the sample. As a result, the theoretical F-N plot shows

qualitatively the same behavior as that of the experiment. It is suggested that a better correspondence between theory and experiment would result from a more sophisticated treatment of the breakdown mechanism.

## SELECTED BIBLIOGRAPHY

1. Allen, F. G. Field Emission from Silicon and Germanium; Field Desorption and Surface Migration. J. Phys. Chem. Solids, 1961, 19, 87-99.
2. Allen, F. G. Work Function and Emission Studies on Clean Silicon Surfaces. J. Phys. Chem. Solids, 1959, 8, 119-122.
3. Allen, F. G., and Gobeli, G. W. Work Function, Photoelectric Threshold, and Surface States of Atomically Clean Silicon. Phys. Rev., 1963, 127, 150-158.
4. Apker, L. and Taft, E. Field Emission from Photoconductors. Phys. Rev., 1952, 88(5), 1037-1038.
5. Arthur, J. R. Energy Distribution of Field Emission from Germanium. Surface Science, 1964, 2, 389-395.
6. Ashcroft, N. W., and Mermin, W. D. Solid State Physics. Philadelphia, PA: Holt, Rhinehart, and Winston, 1976.
7. Bar-Lev, A. Semiconductors and Electronic Devices. London: Prentice-Hall, International, Inc., 1979.
8. Blakemore, J. Semiconductor Statistics. New York: Pergamon Press. 1962.
9. Boltaks, B. I., Diffusion in Semiconductors. New York: Academic Press, 1963.
10. Borzyak, P. G., Yatsenko, A. F., and Miroschnichenko, L. S. Photo Field Emission from High Resistance Silicon and Germanium. Phys. Stat. Sol., 1966, 14, 403-411.
11. Busch, G., and Fischer, T. F. Feldemission aus Silizium. Phys. Kondens. Materie., 1963, 1, 367-393.
12. Cardona, M., and Pollak, F. H. Energy-Band Structure of Germanium and Silicon: The k-p Method. Phys. Rev., 1966, 142, 530-543.
13. Cooper, E. C., and Muller, E. W. Field Emission by Alternating Fields. An Improved Technique for Field Emission Microscopy. Rev. Sci. Instr., 1958, 29 (4), 309-312.
14. D'Asaro, L. A. Field Emission from Silicon. J. Applied Phys., 1958, 29, 33-34.

15. Dobretsov, L. N., and Gomoyunova, M. V. [Emission Electronics] (I. Schectman, trans., Y. Freundlich and T. Korn, Eds.), Jerusalem: Israel Program for Scientific Translations, Ltd., 1971. (Originally published, 1966.)
16. Eastman, D. E., and Grobman, W. D., Photoemission Densities of Intrinsic Surface States for Si, Ge, and GaAs. Phys. Rev. Letters, 1972, 28, 1378-1381.
17. Eckert, E. R. G., and Drake, R. M. Analysis of Heat and Mass Transfer. New York: McGraw Hill, 1972.
18. Fischer, R. Die Energieverteilung der bei der ausseren Feldemission aus Halbleitern emittieren Elektronen. Phys. Stat. Solidi., 1962, 2, 1088-1095.
19. Fischer, R. Einfluss der Effektiven Masse auf die Energieverteilung der bei der ausseren Feldemission aus Halbleitern emittieren Elektronen. Phys. Stat. Solidi, 1962, 2, 1466-1470.
20. Fowler, R. H., and Nordheim, L. W. Electron Emission in Intense Electric Fields. Roy. Soc. Proc., 1928, 119, 173-181.
21. Frankl, D. R. Electrical Properties of Semiconductor Surfaces. Oxford: Pergamon Press, 1967.
22. Franz, Von W. Einfluss eines elektrischen Feldes auf eine optische Absorptionskante. Zeitschrift fur Naturforschung, 1958, 13A, 484-489.
23. Gadzuk, J. W., and Plummer, E. W. Field Emission Energy Distribution (FEED). Reviews Mod. Phys., 1973, 45, 487-548.
24. Glaser, A., and Subak-Sharpe, G. Integrated Circuit Engineering. Reading, Mass.: Addison Wesley, 1979.
25. Gomer, R. Field Emission and Field Ionization. Cambridge, MA.: Harvard University Press, 1961.
26. Good, R. H., and Muller, E. W. Field Emission. Handbuch der Physik, (ed. by S. Flugge, Springer-Verlag, Berlin) 1956, 21, 176-231.
27. Herman, M. H., and Tsong, T. T. Photon Excited Field Emission from a Semiconductor Surface. Physics Letters, 1979, 71A, 461-463.
28. Herman, M. H., and Tsong, T. T. Observation of Multiple Peaks in Field Emission Energy Distributions from Silicon. Phys. Rev. Letters, 1982, 48(15), 1029-1032.
29. Huang, K. Statistical Mechanics. New York: John Wiley and Sons, Inc., 1963.

30. Hughes, O. H., and White, P. M. The Energy Distribution of Field-Emitted Electrons from GaAs. Phys. Stat. Solidi, 1969, 33, 309-316.
31. Jackson, J. D. Classical Electrodynamics. New York: John Wiley and Sons, Inc., 1975.
32. Kagan, M. S., Lifshits, T. M., Musatov, A. L., and Sharonov, A. A. Field Emission of Electrons from High Resistivity Germanium. Fiz. Tvera. Tela, 1964, 6, 723. Translated in Sov. Phys. Solid State, 1964, 6, 563.
33. Keldysh, L. V. The Effect of a Strong Electric Field on the Optical Properties of Insulating Crystals. Soviet Physics JETP, 1952, 34(7)(2), 788-790.
34. Kisker, E., Mahan, A. H., and Reihl, B. Energy Loss of Electrons Emitted from W-EuS Junctions. Physics Letters, 1977, 62A(4), 261-264.
35. Kittel, C. Introduction to Solid State Physics. New York: John Wiley and Sons, Inc., 1971.
36. Kleint, Von Ch., and Kusch, S. Uber die Energieverteilung von Feldelektronen aus Silizium. Annalen der Physik, 1964, 13, 210-212.
37. Long, D. Energy Bands in Semiconductors. New York: Interscience Publishers, 1968.
38. Many, A., Goldstein, Y. and Grover, N. B. Semiconductor Surfaces. Amsterdam: North Holland. 1965.
39. Nordheim, L. W. The Effect of the Image Force on the Emission and Reflection of Electrons by Metals. Roy. Soc. Proc., 1928, 121, 626-639.
40. Pals, J. A. Experimental Verification of the Surface Quantization of an n-type Inversion Layer of Silicon at 300 and 77K. Phys. Rev. B, 1972, 5(10), 4208-4210.
41. Pals, J. A. Measurement of the Surface Quantization in Silicon n- and p-Type Inversion Layers at Temperatures Above 25K. Phys. Rev. B, 1973, 7(2), 754-760.
42. Perry, R. L. Experimental Evidence for the Existence of Two Distinct Field Emission Characteristics from Silicon Emitters. J. Appl. Physics, 1961, 32, 128-130.

43. Perry, R. L. Experimental Determination of the Current Density-Electric Field Relationship of Silicon Field Emitters. J. Appl. Phys., 1962, 33(5), 1875-1883.
44. Plummer, E. W. and Young, R. D. Field Emission Studies of Electronic Energy Levels of Adsorbed Atoms. Phys. Rev. B, 1970, 1(5), 2088-2109.
45. Russell, A. M. and Litov, E. Observation of the Band Gap in the Energy Distribution of Electrons Obtained from Silicon by Field Emission. Applied Phys. Letters, 1963, 2(3), 64-66.
46. Seeger, K. Semiconductor Physics. Wein: Springer-Verlag, 1973.
47. Shepherd, W. B., and Peria, W. T. Observation of Surface-State Emission in the Energy Distribution of Electrons Field-Emitted from (100) Oriented Ge. Surface Science, 1973, 38, 461-498.
48. Stern, F. Quantum Properties of Surface Space-Charge Layers. CRC Critical Reviews in Solid State Physics, 1974, 499-514.
49. Stern, F. Self-Consistent Results for n-Type Si Inversion Layers. Phys. Rev. B, 1972, 5, 4891-4899.
50. Stetsenko, B. V., Yatsenko, A. F., and Miroschnichenko, L. S. Effect of Surface States in Transient Processes in Silicon Field Cathodes. Phys. Stat. Solidi (a), 1970, 1, 349-355.
51. Stratton, R. Theory of Field Emission from Semiconductors. Phys. Rev., 1962, 25(1), 67-82.
52. Stratton, R. Energy Distribution of Field Emitted Electrons. Phys. Rev., 1964, 135(3A), A794-A805.
53. Swanson, L. W., and Crouser, L. C. Anomalous Total Energy Distribution of a Tungsten Field Emitter. Phys. Rev. Letters, 1966, 16(10), 389-392.
54. Sze, S. Martin. Physics of Semiconductor Devices. New York: Wiley-Interscience, 1969.
55. Wagner, C. F., and Spicer, W. E. Observation of a Band of Silicon Surface States Containing One Electron Per Surface Atom. Phys. Rev. Letters, 1972, 28, 1381-1384.
56. Yatsenko, A. F. On a Model of Photo Field Emission from P-Type Semiconductors. Phys. Stat. Solidi (a), 1970, 1, 333-348.
57. Young, R. D. Theoretical Total-Energy Distribution of Field Emitted Electrons. Phys. Rev., 1959, 113(1), 110-114.

58. Young, R. D., and Clark, H. E. Effect of Surface Patch Fields on Field Emission Work Function Determinations. Phys. Rev. Letters, 1966, 17(7), 351-353.
59. Young, R. D., and Kuyatt, C. E. Resolution Determination in Field Emission Energy Analysers. Rev. Sci. Instrum., 1968, 39(10), 1477-1480.
60. Young, R. D., and Muller E. W. Experimental Measurement of the Total-Energy Distributions of Field Emitted Electrons. Phys. Rev. Letters, 1959, 113(1), 115-120.

APPENDIX A  
BASIC PROGRAM FOR EXPERIMENTATION

The Basic program, contained in this appendix, controls the FEED experiment. After loading this program into the Apple II, the user must next load in the machine language program contained in Appendix B. Typing ]RUN causes a "menu" of options to appear for the program user.

These options appear in lines 130 to 202. After a choice is made by the user in line 210, control is transferred to specific program sections, as defined in lines 215 to 274. Such sections prompt the user for input whenever decisions are required. Musical prompts are incorporated to direct user attention to equipment problems or when physical manipulation is required, such as during the X-Y plotting routine.

Once data is taken, it can be stored on cassette tape. The user first must determine the extent of memory which the data occupies. This is accomplished by typing "D" from the menu. The resulting prompt character, a star (\*), shows that the computer is in the "monitor" mode. Typing \*7000 next, then holding the REPEAT key down with the RETURN key depressed simultaneously causes the memory locations to appear rapidly on the screen. If they are zeros until \*8000 is reached, then the minimum value of the data should be \*8000. Otherwise, the minimum should be \*7000. The user determines the maximum value by testing

memory values higher than \*8000. Typically, one test \*9000, \*A000, etc. until zeros are encountered. The end of the data is determined by testing between the known zero and known non-zero locations. The user starts the cassette recorder in the "Record" mode, then types \*mini.maxiW to Write onto the tape from minimum to maximum locations. At this point, the user should make notation of the stored memory minimum and maximum. To reload data stored on tape, the user types "D" from the menu. After starting the cassette recorder on "Play," the user types \*8000.9700R, for example, to Read the recorded data into locations \*8000 to \*9700. It is important to realize that the data must be placed back into the same memory locations from which it was originally stored. Also, it should be noted that the cassette recorder should have its volume and tone controls both set to the value 9.

JLIST

```

5  GOTO 100
6  FOR I = 28672 TO 32767: POKE I,0: NEXT I: GOTO 100
10 INPUT "NEW DATE OR SAMPLE?":A$: IF A$ < > "Y" THEN
    35
15 INPUT "DATE:(MO,DY,YR)":MO,DY,YR: POKE 27404,MO: POKE
    27405,DY: POKE 27406,YR
21 PRINT "SAMPLE TYPES:1 = W": PRINT TAB( 13)"2 = SI
    LICON- INTRINSIC": PRINT TAB( 13)"3 = SI P-TYPE"
    : PRINT TAB( 17)"4 = SI N-TYPE": PRINT TAB( 13)
    "5 = OTHER METAL": PRINT TAB( 13)"6 = OTHER SEMI
    CONDUCTOR"
25 INPUT "WHICH SAMPLE TYPE?":S1: POKE 27403,S1: INPUT
    "ON GRAPHING-WHAT MESH SIZE?":A9
35 POKE 32779,( PEEK (27404)): POKE 32780,( PEEK (274
    05)): POKE 32781,( PEEK (27406)): POKE 32778,( PEEK
    (27403)): POKE 6,A9: RETURN
59 A1 = 0
60 POKE - 16304,0: POKE - 16299,0: POKE - 16297,0:
    POKE - 16301,0
70 INPUT "WANT OUT?":A1$: IF A2 = 0 THEN A1 = 0
72 IF A2 = 1 THEN A1 = 1
75 IF A1$ = "Y" THEN GOTO 100
80 IF A1 = 1 THEN POKE - 16300,0: POKE - 16301,0
85 IF A1 = 0 THEN POKE - 16299,0: POKE - 16302,0
87 IF A1 = 0 THEN A2 = 1
88 IF A1 = 1 THEN A2 = 0
90 GOTO 70
100 TEXT
120 PRINT "MENU:TYPE 'F' FOR FIXED RETARDER VALUE": PRINT
    : PRINT TAB( 11)"'I' FOR INFO ON PARAMETERS": PRINT

130 PRINT TAB( 11)"'M' FOR PUTTING RETARDER AT": PRINT
    TAB( 17)"10 VOLTS": PRINT TAB( 11)"'G' FOR RUNN
    ING THE EXPERIMENT"
140 PRINT TAB( 11)"'U' FOR RAW NUMERICAL DATA": PRINT

190 PRINT TAB( 11)"'L' FOR LOOKING AT A GRAPH": PRINT
    TAB( 17)"OF THE DATA"
202 PRINT TAB( 11)"'D' FOR READING/WRITING DATA": PRINT
    : PRINT TAB( 11)"'C' FOR COMPARING DATA": PRINT

210 PRINT "": INPUT "WHAT COURSE?":Z1$
215 IF Z1$ = "I" THEN 1350
220 IF Z1$ = "F" THEN 290
230 IF Z1$ = "M" THEN 360
240 IF Z1$ = "G" THEN 370
260 IF Z1$ = "U" THEN 940
270 IF Z1$ = "L" THEN 1060
272 IF Z1$ = "D" THEN CALL - 151
274 IF Z1$ = "C" THEN 59

```

```

280 HOME : GOTO 120
290 INPUT "WHAT FIXED VALUE OF U-RET?":T1
300 F0 = 409.6:T2 = INT (T1 * F0):X = PEEK (49412)
320 FOR TA = 1 TO T2:X = PEEK (49410): NEXT TA
350 HOME : GOTO 120
360 X = PEEK (49412): HOME : GOTO 120
370 INPUT "FULL VOLTAGE RANGE?(Y OR N)":A$
380 IF A$ < > "Y" THEN 420
390 U0 = 10:U9 = 0: GOTO 440
420 INPUT "MIN. VOLTAGE OF RETARDER?":U9
430 INPUT "MAX VALUE?":U0
440 INPUT "READINGS/VOLTAGE STEP?":R
450 INPUT "HOW MANY LOOPS?":L
460 N = 2.4414E - 3:X = INT ((U0 / N) - 1):Y = INT (
U9 / N):G1 = X - Y:YB = INT (Y / 256)
500 YB = INT (Y / 256):YA = Y - (256 * YB):GB = INT
(G1 / 256):GA = G1 - (256 * GB)
540 IF G1 > 4095 THEN PRINT "MAX EXCEEDS 4095 COUNTS
!"
545 IF G1 > 4095 THEN STOP
550 POKE 27394,R: POKE 27395,R: POKE 27396,L: POKE 27
401,YA: POKE 27402,YB: POKE 27397,GA: POKE 27398,
GB
620 PRINT "THESE VALUES HAVE BEEN LOADED."
630 CALL 27413
640 MAX = G1:H1 = PEEK (27409)
660 S0 = ( INT ((U1 - M1) * 409.6) * 3 + 32789)
670 IF H1 = 1 THEN PRINT "": PRINT "**ERROR IN DATA B
US OR A/D POWER!!!!*": PRINT "": GOSUB 3000
683 IF H1 = 1 THEN 120
684 FOR I = 1 TO 5
685 FOR K = 1 TO 8: POKE 27684,K: CALL 27685: NEXT K
686 NEXT I
690 POKE 32768,R: POKE 32769,L: POKE 32770,YA: POKE 3
2771,YB: POKE 32772,GA: POKE 32773,GB: GOSUB 10
691 INPUT "U-TIP?":U1
760 POKE 32774, INT (U1 - INT (U1 / 256) * 256): POKE
32775, INT (U1 / 256): INPUT "U-ANODE":U2: POKE 3
2776, INT (U2 - INT (U2 / 256) * 256):
800 POKE 32777, INT (U2 / 256)
890 INPUT "LENS VOLTAGE":U5: POKE 32783, INT (U5 / 2)
: INPUT "TEMPERATURE IN KELVIN":U7
910 POKE 32784, INT (U7 / 4): INPUT "WHAT OFFSET (RET
=0)?":U8: POKE 32786, INT (U8 / 256)
923 POKE 32785, INT (U8 - INT (U8 / 256) * 256):
924 INPUT "LIGHT OR DARK(1 OR 0)":A2
925 GOTO 120
940 INPUT "WANT FAULT TOLERANCE?":F$
945 IF F$ < > "Y" THEN 955
950 INPUT "WHAT FAULT TOLERANCE?":IM
955 INPUT "WHAT I? ":I:I2 = I * 3: FOR I1 = I2 TO 409
6:P1 = 3 * I1
960 IF (32768 + P1) > 40170 THEN STOP

```

```

980 DEF FN UA(P2) = PEEK (P2 + 32789 + P1)
990 PP = FN UA(0) + (256 * ( FN UA(1))) + (256 ^ 2 *
  ( FN UA(2))) + 256 ^ 3 * PEEK (28679 + I1)
991 PQ = FN UA(3) + (256 * ( FN UA(4))) + (256 ^ 2 *
  ( FN UA(5))) + 256 ^ 3 * PEEK (28679 + I1 + 1)
993 IF PQ - PP < - 15000000 THEN POKE (28679 + I1 +
  1),1: GOTO 990
1001 PR = PQ - PP: PRINT (32768 + P1),PP,PR
1002 IF F$ < > "Y" THEN NEXT I1
1003 IF ABS (PR) > IM THEN GOSUB 2040
1005 PQ = FN UA(3) + (256 * ( FN UA(4))) + (256 ^ 2 *
  ( FN UA(5)))
1010 PR = PQ - PP: PRINT (32768 + P1),PP,PR: NEXT I1: PRINT
  "": PRINT "": HOME : GOTO 120
1060 PRINT "          *****": PRINT " THIS IS A DATA
  VIEW:A PLOT": PRINT "          OVER ANY RANGE OF"
1070 CLEAR
1090 PRINT " THE ENERGY DISTRIBUTION.": PRINT "
  *****": PRINT "": GOSUB 1620
1100 RL = PEEK (32768) * PEEK (32769)
1162 INPUT "CLEAR PREVIOUS GRAPHS?":G1$: IF G1$ = "Y"
  THEN HGR
1165 INPUT "HARDCOPY ALSO?":P$: IF P$ = "Y" THEN INPUT
  "READY?":Z1$: GOSUB 1900
1168 POKE - 16297,0: POKE - 16300,0: POKE - 16304,
  0: HCOLOR= 3: POKE - 16301,0: FOR X1 = 0 TO INT
  (N)
1173 X = INT (X1 * N1): HPL0T X,157: NEXT X1
1181 HPL0T 0,78 TO 278,78: FOR X2 = 0 TO INT (N / 4)
  :X = INT (X2 * N1 * 4): HPL0T X,158: HPL0T X,159
  : NEXT X2: HPL0T 0,156
1190 FOR I1 = 0 TO 278
1202 ZA = INT (I1 * (ZC - T0) / 278)
1203 T2 = T0 + ZA - S3
1204 T1 = T2 + 2 * S3
1205 S2 = S0 + 3 * ZA - 3 * S3
1210 S1 = S2 + 6 * S3
1211 PRINT "S1="S1,"T1="T1
1213 GOTO 1215
1214 S2 = S0 - 3 * S3:T2 = T0 - S3
1215 DEF FN PP(S2) = PEEK (S2) + 256 * PEEK (S2 +
  1) + (256 ^ 2) * PEEK (S2 + 2)
1216 DEF FN PA(T2) = 256 ^ 3 * PEEK (T2)
1217 PP = 0:PQ = 0:A9 = PEEK (6)
1218 FOR A = - A9 TO A9
1220 PP = PP + FN PP(S2 + 3 * A) + FN PA(T2 + A)
1230 PQ = PQ + FN PP(S1 + 3 * A) + FN PA(T1 + A)
1235 NEXT A
1240 PR = (PQ - PP) / (RL * AA)
1241 IF PR > MZ THEN MZ = PR: POKE 32766,( INT (MZ /
  256)): POKE 32767,MZ - 256 * ( INT (MZ / 256))
1250 PS = PR * F1 / S3
1251 IF Z3$ = "Y" THEN PS = PR * 156 / MZ

```

```

1260 IF PS > 156 THEN HPLOT TO I1,156
1261 IF PS > 156 THEN PS = PS - 156
1262 IF PS > 156 THEN 1261
1270 IF PS < 0 THEN PS = 0
1275 IF P$ = "Y" THEN GOSUB 2000
1280 PT = 156 - PS
1290 HPLOT TO I1,PT
1291 B5 = B6
1292 IF PS < 78 THEN B6 = 0
1293 IF PS > 78 THEN B6 = 1
1294 IF ABS (B6 - B5) = 1 THEN HPLOT I1,156 TO I1,1
50: HPLOT I1,PT
1300 NEXT I1
1305 H1 = 0: GOSUB 3000
1310 INPUT "GO BACK TO MENU (HIT M) OR MORE PLOTS?":Z
2$: IF Z$ = "M" THEN TEXT : HOME : CLEAR : GOTO
120
1330 GOTO 1060
1350 PRINT "R=" PEEK (32768) " L=" PEEK (32769) " P=" < PEEK
(32768) * PEEK (32769)
1355 US = PEEK (32771) * 256 + PEEK (32770)
1360 UT = PEEK (32774) + 256 * PEEK (32775)
1365 UA = PEEK (32776) + 256 * PEEK (32777)
1370 PRINT "U-START=" << INT (US / 4.096) * .01
1375 PRINT "U-TIP:" UT " U-ANODE:" UA " U-DIFF=" UT -
UA
1380 PRINT "OFFSET VOLTAGE:" < PEEK (32785) + PEEK (3
2786) * 256)
1385 PRINT "TEMPERATURE IN KELVIN:" 4 * PEEK (32784)
1390 PRINT "LENS VOLTAGE:" PEEK (32783) * 2
1450 PRINT "DATE:" PEEK (32779) "/" PEEK (32780) "/" PEEK
(32781)
1470 PRINT "SAMPLE TYPE:" PEEK (32778)
1480 GET KY: GOTO 120
1620 INPUT "NORMALIZE?":Z3$:MZ = (256 * PEEK (32766)
+ PEEK (32767))
1626 IF Z3$ = "N" THEN MZ = 0: INPUT "FACTOR GUESS?":
F1
1629 F0 = 409.6
1630 MI = ( PEEK (32771) * 256 + PEEK (32770)) / F0
1632 MI% = 1000 * MI:MI = MI% / 1000
1640 PRINT "THE DATA'S STARTING VOLTAGE IS "MI" VOLTS
."
1645 INPUT "HOW MANY POINTS DO YOU WISH TO AVERAGE?":
S3
1647 INPUT "ON GRAPHING-WHAT MESH SIZE FOR AVERAGING?
":A9: POKE 6,A9
1648 AA = 2 * A9 + 1
1650 INPUT "WHAT VOLTAGE DO YOU WISH TO START AT?":U1
1659 T0 = ( INT ((U1 - MI) * F0) + 28679)
1660 S0 = ( INT ((U1 - MI) * F0) * 3 + 32789)
1661 INPUT "WHAT MAX VOLTAGE":ZB

```

```

1663 ZC = INT ((ZB - M1) * F0) + 28679
1664 N = (ZB - U1) * 20:N1 = 278 / N
1665 RETURN
1900 X = PEEK (49438):X = PEEK (49439): FOR I = 1 TO
      100:X = PEEK (49425): NEXT I: INPUT "READY?":Z1$

1903 INPUT "PLOT TICS?":P1$: IF P1$ = "N" THEN RETURN

1904 X7 = 0
1905 FOR X1 = 0 TO INT (N):X = INT (N1 * 3 * X1) -
      INT (N1 * 3 * (X1 - 1))
1906 P9 = 10
1907 IF X7 = 0 THEN P9 = 20
1912 FOR I = 1 TO 200: NEXT I
1914 FOR I = 1 TO 100: NEXT I: FOR I = 1 TO P9:Y = PEEK
      (49428): NEXT I
1917 FOR I = 1 TO 100: NEXT I: FOR I = 1 TO P9:Y = PEEK
      (49424): NEXT I
1925 FOR I = 1 TO X:Y = PEEK (49426): NEXT I
1926 X7 = X7 + 4: IF X7 - 16 = 0 THEN X7 = 0
1927 NEXT X1
1930 H1 = 0: GOSUB 3000: INPUT "RAISE PEN!!!":Z5$
1931 X = PEEK (49438):X = PEEK (49439): FOR I = 1 TO
      100:X = PEEK (49425): NEXT I: FOR I = 1 TO 10:X =
      PEEK (49424): NEXT I
1932 INPUT "READY?":Z1$: RETURN
2000 A1 = PS - A1: IF A1 > 0 THEN A2 = INT (3 * A1 +
      .5): IF A2 < > 0 THEN FOR I = 1 TO A2:X = PEEK
      (49424): NEXT I
2012 IF A1 < 0 THEN A2 = INT (- 3 * A1 + .5): IF A2
      < > 0 THEN FOR I = 1 TO A2:X = PEEK (49428): NEXT
      I
2030 FOR I = 1 TO 3:X = PEEK (49426): NEXT I:A1 = PS
      : RETURN
2040 POKE (32768 + P1 + 5), ( PEEK (32768 + T1 + 2))
2041 POKE (32768 + P1 + 4), ( PEEK (32768 + P1 + 1))
2043 POKE (32768 + P1 + 3), ( PEEK (32768 + P1))
2045 RETURN
3000 FOR I = 1 TO 19: IF I < = 10 THEN J = I
3001 IF I > 10 THEN J = 20 - I
3002 A = I: POKE 27684,A: CALL 27685: NEXT I
3003 RETURN

```

## APPENDIX B

## MACHINE LANGUAGE PROGRAM FOR DATA ACQUISITION

This program resides in memory locations \*6B15 through \*6C88. It is written for the Apple II's Mostek 6502 microprocessor. The leftmost column of the printout is the memory location, specified in hexadecimal, beginning with \*6B15. The next three columns hold the actual program steps, again in hexadecimal notation. The rightmost two columns are the "disassembled" mnemonic notation for the hexadecimal program step on the same line.

Lines \*6B16 through \*6B1C cause the program to jump to several subroutines. These subroutines set initial conditions by zeroing all pertinent data storage locations, setting the retarder to its minimum operating voltage, and loading the R and L counters properly. Steps \*6B26 through \*6B3B comprise a waiting cycle, and test the ADC for status. If conversion is not complete after 126 cycles, control is transferred to \*6BA5, which sets an error flag and exits back to the Basic program.

Once conversion is complete, lines \*6B3D through \*6B5F perform a quadruple precision addition into the appropriate memory locations. Lines \*6B61 through \*6B42 increment the memory locations to provide proper sequencing of data, and test the R and L loops for completion. Lines \*6C25 through \*6C52 generate music on the Apple's speaker. Lastly, lines \*6C60 through \*6C6F test the data bus for failure.

\*LL

6B15-	78		SEI	
6B16-	20 AD	6B	JSR	\$6BAD
6B19-	20 04	6C	JSR	\$6C04
6B1C-	20 D9	6B	JSR	\$6BD9
6B1F-	AD 0C	C1	LDA	\$C10C
6B22-	4C 63	6C	JMP	\$6C63
6B25-	EA		NOP	
6B26-	AD 0A	C1	LDA	\$C10A
6B29-	A9 79		LDA	#\$79
6B2B-	8D 01	6B	STA	\$6B01
6B2E-	CE 01	6B	DEC	\$6B01
6B31-	D0 03		BNE	\$6B36
6B33-	4C A5	6B	JMP	\$6BA5
6B36-	AD 09	C1	LDA	\$C109
6B39-	29 F0		AND	#\$F0
6B3E-	D0 F1		BNE	\$6B2E
6B3D-	A0 00		LDY	#\$00
6B3F-	AD 0B	C1	LDA	\$C10B
6B42-	AD 08	C1	LDA	\$C108
6B45-	18		CLC	
6B46-	71 F9		ADC	(\$F9),Y
6B48-	91 F9		STA	(\$F9),Y
6B4A-	C8		INY	
6B4B-	AD 09	C1	LDA	\$C109
6B4E-	71 F9		ADC	(\$F9),Y
6B50-	91 F9		STA	(\$F9),Y
6B52-	C8		INY	
6B53-	A9 00		LDA	#\$00
6B55-	71 F9		ADC	(\$F9),Y
6B57-	91 F9		STA	(\$F9),Y
6B59-	88		DEY	
6B5A-	88		DEY	
6B5B-	A9 00		LDA	#\$00
6B5D-	71 ED		ADC	(\$ED),Y
6B5F-	91 ED		STA	(\$ED),Y
6B61-	CE 03	6B	DEC	\$6B03
6B64-	F0 03		BEQ	\$6B69
6B66-	4C 1F	6B	JMP	\$6B1F
6B69-	AD 02	6B	LDA	\$6B02
6B6C-	8D 03	6B	STA	\$6B03

Best Available Copy

6B6F-	AD 02 C1	LDA	#C102
6B72-	AD 12 C1	LDA	#C112
6B75-	E6 F9	INC	\$F9
6B77-	D0 02	BNE	\$6B7B
6B79-	E6 FA	INC	\$FA
6B7B-	E6 F9	INC	\$F9
6B7D-	D0 02	BNE	\$6B81
6B7F-	E6 FA	INC	\$FA
6B81-	E6 F9	INC	\$F9
6B83-	D0 02	BNE	\$6B87
6B85-	E6 FA	INC	\$FA
6B87-	E6 ED	INC	\$ED
6B89-	D0 02	BNE	\$6B8D
6B8B-	E6 EE	INC	\$EE
6B8D-	C6 EB	DEC	\$EB
6B8F-	A5 EB	LDA	\$EB
6B91-	C9 FF	CMP	#\$FF
6B93-	D0 D1	BNE	\$6B66
6B95-	C6 EC	DEC	\$EC
6B97-	A5 EC	LDA	\$EC
6B99-	C9 FF	CMP	#\$FF
6B9B-	D0 C9	BNE	\$6B66
6B9D-	CE 04 6B	DEC	\$6B04
6BA0-	F0 06	BEQ	\$6BA8
6BA2-	4C 19 6B	JMP	\$6B19
6BA5-	EE 11 6B	INC	\$6B11
6BA8-	60	RTS	
6BA9-	EA	NOP	
6BAA-	EA	NOP	
6BAB-	EA	NOP	
6BAC-	EA	NOP	
6BA0-	A0 00	LDY	#\$00
6BAF-	A2 40	LDX	#\$40
6BB1-	86 FB	STX	\$FB
6BB3-	A2 70	LDX	#\$70
6BB5-	86 FA	STX	\$FA
6BB7-	A2 80	LDX	#\$80
6BB9-	86 FD	STX	\$FD
6BBB-	A2 15	LDX	#\$15
6BBD-	86 FC	STX	\$FC

68BF-	84	F9	STV	\$F9
68C1-	98		TVA	
68C2-	8D	11 6B	STA	\$6B11
68C5-	91	F9	STA	(\$F9),Y
68C7-	E6	F9	INC	\$F9
68C9-	D0	FA	BNE	\$6B05
68CB-	E6	FA	INC	\$FA
68CD-	C6	FB	DEC	\$FB
68CF-	D0	F4	BNE	\$6B05
68D1-	A9	40	LDA	#\$40
68D3-	85	FB	STA	\$FB
68D5-	60		RTS	
68D6-	EA		NOP	
68D7-	EA		NOP	
68D8-	EA		NOP	
68D9-	AD	0A 6B	LDA	\$6B0A
68DC-	85	FF	STA	\$FF
68DE-	AD	09 6B	LDA	\$6B09
68E1-	85	FE	STA	\$FE
68E3-	AD	04 C1	LDA	\$C104
68E6-	AD	1E C1	LDA	\$C11E
68E9-	AD	02 C1	LDA	\$C102
68EC-	AD	12 C1	LDA	\$C112
68EF-	C6	FE	DEC	\$FE
68F1-	A5	FE	LDA	\$FE
68F3-	C9	FF	CMP	#\$FF
68F5-	D0	F2	BNE	\$6BE9
68F7-	C6	FF	DEC	\$FF
68F9-	A5	FF	LDA	\$FF
68FB-	C9	FF	CMP	#\$FF
68FD-	D0	EA	BNE	\$6BE9
68FF-	60		RTS	
6C00-	EA		NOP	
6C01-	EA		NOP	
6C02-	EA		NOP	
6C03-	EA		NOP	
6C04-	A5	FC	LDA	\$FC
6C06-	85	F9	STA	\$F9
6C08-	A5	FD	LDA	\$FD
6C0A-	85	FA	STA	\$FA

Best Available Copy

6C0C-	A9 40	LDA	##40
6C0E-	85 13	STA	#13
6C10-	AD 05 6B	LDA	\$6B05
6C13-	85 EB	STA	#EB
6C15-	AD 06 6B	LDA	\$6B06
6C18-	85 EC	STA	#EC
6C1A-	A9 70	LDA	##70
6C1C-	85 EE	STA	#EE
6C1E-	A9 07	LDA	##07
6C20-	85 ED	STA	#ED
6C22-	60	RTS	
6C23-	EA	NOP	
6C24-	08	PHP	
6C25-	A2 FF	LDX	##FF
6C27-	AD 30 C0	LDA	\$C030
6C2A-	AD 24 6C	LDA	\$6C24
6C2D-	20 A8 FC	JSR	\$FC08
6C30-	CA	DEX	
6C31-	D0 01	BNE	\$6C34
6C33-	60	RTS	
6C34-	4C 27 6C	JMP	\$6C27
6C37-	60	RTS	
6C38-	10 10	BPL	\$6C4A
6C3A-	09 10	ORA	##10
6C3C-	09 08	ORA	##08
6C3E-	09 64	ORA	##64
6C40-	09 09	ORA	##09
6C42-	08	PHP	
6C43-	09 08	ORA	##08
6C45-	07	???	
6C46-	08	PHP	
6C47-	64	???	
6C48-	08	PHP	
6C49-	08	PHP	
6C4A-	07	???	
6C4B-	08	PHP	
6C4C-	09 10	ORA	##10
6C4E-	10 09	BPL	\$6C59
6C50-	09 09	ORA	##09
6C52-	09 64	ORA	##64

6C54-	23	???	
6C55-	6B	???	
6C56-	FF	???	
6C57-	00	BRK	
6C58-	00	BRK	
6C59-	FF	???	
6C5A-	FF	???	
6C5B-	00	BRK	
6C5C-	00	BRK	
6C5D-	94 FF	STY	\$FF,X
6C5F-	00	BRK	
6C60-	4C A5 6B	JMP	\$6BA5
6C63-	AD 0E C1	LDA	\$C10E
6C66-	D0 F3	BNE	\$6C60
6C68-	AD 0D C1	LDA	\$C10D
6C6B-	C9 FF	CMP	#\$FF
6C6D-	D0 F1	BNE	\$6C60
6C6F-	4C 25 6B	JMP	\$6B25
6C72-	FF	???	
6C73-	00	BRK	
6C74-	01 DF	ORA	(&DF,X)
6C76-	FF	???	
6C77-	00	BRK	
6C78-	00	BRK	
6C79-	FF	???	
6C7A-	FF	???	
6C7B-	00	BRK	
6C7C-	00	BRK	
6C7D-	23	???	
6C7E-	FF	???	
6C7F-	00	BRK	
6C80-	00	BRK	
6C81-	FF	???	
6C82-	FF	???	
6C83-	00	BRK	
6C84-	00	BRK	
6C85-	DF	???	
6C86-	FF	???	
6C87-	00	BRK	
6C88-	00	BRK	

Best Available Copy

#### VITA

A native of Hartford, Connecticut, Michael Herman was born on June 8, 1954. He graduated from George J. Penney High School in East Hartford in May of 1972. Subsequently, he majored in Physics at Grinnell College in Grinnell, Iowa. Upon completion of his B.A. in May of 1976, he attended graduate school in Physics at The Pennsylvania State University. In the Fall of 1977, he joined the Field Emission Laboratory to undertake research for the Ph.D. degree.

Mr. Herman is a member of the American Physical Society, Phi Beta Kappa, and Sigma Pi Sigma.

DISTRIBUTION LIST FOR TM 82-177

Commander (NSEA 0342)  
Naval Sea Systems Command  
Department of the Navy  
Washington, DC 20362

Copies 1 and 2

Commander (NSEA 9961)  
Naval Sea Systems Command  
Department of the Navy  
Washington, DC 20362

Copies 3 and 4

Defense Technical Information Center  
5010 Duke Street  
Cameron Station  
Alexandria, VA 22314

Copies 5 through 10

**DATE**  
**ILME**